A 3D maximum likelihood analysis for studying highly extended sources in VERITAS data

by

Joshua Vincent Cardenzana

A dissertation submitted to the graduate faculty

in partial fulfillment of the requirements for the degree of

DOCTOR OF PHILOSOPHY

Major: Astrophysics

Program of Study Committee:
Amanda J. Weinstein, Major Professor
Frank Krennrich
Mayly Sanchez
Curtis Struck
Jue Yan

Iowa State University

Ames, Iowa

2017

DEDICATION

I dedicate this thesis to my wife, Amy. Your unwavering support helped me get through the long days and even longer nights. You are truly the most amazing person I have ever met. Thank you for standing by me through this ordeal and for all your emotional support (and financial support). And to my parents, without whose encouragement I would never have made it this far.

TABLE OF CONTENTS

LIST OF TABLES

LIST OF FIGURES

ABSTRACT

Imaging Atmospheric Cherenkov Telescopes have provided insights into many astrophysical phenomena including particle acceleration in SNR, studies of the extragalactic background light, and high energy emission from pulsars. However, current techniques for analyzing IACT data are poorly suited to studying emission greater than a few tenths of a degree. This thesis outlines a new analysis technique, known as the *3D MLM*, designed to enhance the sensitivity of the VERITAS IACT array to sources from 0.5° to greater than 2° in radius. This analysis employs a maximum likelihood technique which models the expected distribution of events in the VERITAS data in two dimensions analogous to sky coordinates. Additionally a third dimension based on *mean scaled width*, a known gamma/hadron discrimination parameter, improves the sensitivity of the 3D MLM to such highly extended sources. Simulated VERITAS observations of 2FHL J0431.2+5553e, a 1.27° radius *Fermi*-LAT source, demonstrate the potential superior performance of this new technique over the standard ring background model analysis.

CHAPTER 1. INTRODUCTION

1.1 Brief History of Gamma-Ray Astronomy

When compared to the history of astronomy in other wavelengths, ground based gamma-ray astronomy is a rather young field (Weekes, 2005). Gamma-ray astronomy began with the suggestion that a non-trivial portion of the night sky background light[1] (approximately 0.01%) could originate from Cherenkov radiation (Blackett, 1949). This radiation originates from highly energetic charged particles moving through Earth's atmosphere. A few years later, Galbraith and Jelley (1953) reported the first observed Cherenkov pulses using a single photomultiplier tube (PMT), a 10 inch parabolic mirror, and an oscilloscope. Galbraith and Jelley were able to correlate signals in their simple Cherenkov telescope with signals obtained from a near-by air-shower detector, effectively showing that the showers were the origin of the observed light pulses.

The Cherenkov light emitted in the atmosphere is produced by particle showers initiated by either gamma-rays (high energy photons) or cosmic-rays[2]. Since cosmic-rays carry a charge, their paths through the interstellar medium are distorted by the magnetic fields that permeate the galaxy. By the time these cosmic rays finally arrive at Earth, all information regarding where they originated has been lost, resulting in a nearly isotropic distribution of cosmic-rays across the sky. However, gamma-ray photons travel nearly undisturbed through our galaxy and will appear to concentrate near the source of their emission. Making use of the technique by Galbraith and Jelley, scientists began to search for gamma-ray sources by observing the Cherenkov light that was emitted by the resulting particle shower after their interaction with

[1] *Night sky background* light refers to the ambient glow of the night sky. Significant sources of this glow included man-made lights (e.g. street lights and car headlights) and light from the moon scattered in the atmosphere.

[2] Cosmic-rays in this context are high energy (> 1 GeV) charged particles such as protons, atomic nuclei, or electrons.

the atmosphere.

Utilizing a more complicated setup, in which many PMTs are used to image the profile of the Cherenkov radiation in multiple cameras, scientists found that they could reconstruct the positions of incoming gamma-rays and cosmic-rays on the sky. Such telescopes are often referred to as imaging atmospheric Cherenkov telescopes (IACT). They then attempted to locate point-sources of gamma-ray emission by looking for regions with higher concentrations of observed events. Unfortunately, due to the low number of gamma-ray events relative to cosmic-ray events ($\lesssim 1\%$) any such signal was swamped by the cosmic-ray background.

Hillas (1985) presented a technique which characterizes the observed images in a telescope camera using several computed moments. By selecting events within certain ranges of these parameters it is possible to dramatically reduce the number of cosmic-ray events in data while preserving a significant fraction of the gamma-ray events. The most important parameters were the r.m.s. of the observed image width and length. Adopting this technique led to the first credible detection of an astrophysical source of gamma-rays by an IACT with the Whipple observatory (Weekes et al., 1989). Since this first detection of the Crab nebula, the source has been studied extensively and the central pulsar has even become the first to be detected above 100 GeV (Aliu et al., 2011).

It is necessary to provide an overview of typical acceleration and emission mechanisms in high energy sources. Gamma-ray emission is thought to originate primarily from leptons and hadrons. The leptonic component consists of high energy electrons (e^-) and positrons (e^+) while the hadronic component consists of high energy protons and atomic nuclei. These particles are accelerated to high energy (greater than a few tens of GeV) at which point they can emit high energy photons through interactions with their local environment.

1.2 Diffusive Shock Acceleration

Shock waves exist in many astrophysical environments (e.g. supernova remnants expanding into the interstellar medium, interactions between molecular clouds, bow shocks around stars as they move through the interstellar medium, etc...). As the shock develops it sweeps up slow moving material in the path of the shock. One of the most important processes in high

energy gamma-ray astronomy is the acceleration of charged particles in such shocks to very high energies through a process known as first order Fermi (Fermi-I) acceleration (Fermi, 1949), also referred to as *diffusive shock acceleration* (DSA). As particles move back and forth across the shock front, they scatter off inhomogeneities in the magnetic fields which move along with the shock. Each scattering event amplifies the energy of the particle by a factor[3]

$$\frac{E_{after}}{E_{before}} = \gamma^2 \left[1 + \frac{2Uv_0 cos\theta}{c^2} + \left(\frac{U}{c}\right)^2\right] \tag{1.1}$$

where γ is the Lorentz factor associated with the shock wave, U and v_0 are the speeds of the shock wave and particle respectively, and θ is the inclination angle between the motion of the particle and the shock front material.

As particles travel across the shock front in either direction they will see the oncoming material moving towards them with velocity U. This implies that particles are accelerated regardless of the direction in which they travel across the shock front. The particles that ultimately escape from this process will exhibit a power law spectrum.

1.3 Emission Mechanisms

1.3.1 Synchrotron Emission

The ambient magnetic field strength between stars is approximately 3 μG (Zirnstein et al., 2016), but the magnetic field strength in supernova remnants (SNR) can be as much as several to hundreds of micro-Gauss and active galactic nuclei (AGN) can have magnetic fields orders of magnitude stronger still. Leptons will spiral along these relatively intense field lines losing energy through synchrotron radiation[4]. Due to the relativistic nature of the particles producing this emission the radiation is highly beamed, however the random distribution of magnetic fields in an astrophysical source and the large population of particles result in synchrotron emission emitted in all directions. The amount of radiation emitted by a single electron with energy E in a magnetic field B is given approximately by Eq. 1.2 (Ginzburg and Syrovatskii (1965), Eq. 2.10).

$$P_{sync} = 0.98 \times 10^{-8} \left(\frac{B}{[\mathrm{G}]}\right)^2 \left(\frac{E}{mc^2}\right)^2 [\mathrm{eV} \cdot \mathrm{s}^{-1}] \tag{1.2}$$

[3] A more rigorous derivation of this is provided in Appendix A.

[4] Synchrotron radiation is sometimes also referred to as *magnetobremsstrahlung* radiation.

As can be seen, the power loss is inversely proportional to the square of the particle mass, suggesting that electrons and positrons will lose energy through synchrotron radiation more rapidly than heavier particles, such as protons. This radiation is emitted at wavelengths from radio up to X-ray. The peak frequency of the emitted radiation from a single electron with energy E can be approximated by (Ginzburg and Syrovatskii (1965), Eq. 2.23)

$$\begin{aligned} \nu_{peak} &= 1.2 \times 10^{6} \left(\frac{B}{[\mathrm{G}]}\right) \left(\frac{E}{mc^2}\right)^2 [\mathrm{Hz}] \\ \nu_{e^-,peak} &\approx 4.6 \times 10^{-6} \left(\frac{B}{[\mathrm{G}]}\right) \left(\frac{E_{e^-}}{[\mathrm{eV}]}\right)^2 [\mathrm{Hz}] \end{aligned} \tag{1.3}$$

This can be reversed to find an expression for the energy of an electron which produces synchrotron radiation at a given frequency.

$$E_{e^-} = 4.7 \times 10^{2} \left(\frac{\nu}{[\mathrm{Hz}]}\right)^{1/2} \left(\frac{B}{[\mathrm{G}]}\right)^{-1/2} [\mathrm{eV}] \tag{1.4}$$

Electrons can also emit synchrotron emission when they travel along *curved* magnetic field lines. This special case of synchrotron emission is often referred to as *curvature radiation*. Curvature radiation is an important process for understanding high energy emission from pulsars (see 1.4.3).

1.3.2 Inverse Compton Emission

High energy leptons can also up scatter ambient photons to high energies through inverse Compton (IC) scattering. These ambient photons can be nearby starlight, photons from the cosmic microwave background (CMB), or even synchrotron photons emitted by the same electron population. IC scattering of the latter photons is referred to as *synchrotron self-compton*. On average, an IC scattered photon will have energy equivalent to (Longair, 1992)

$$\left\langle E'_{\gamma} \right\rangle_{gain} = \frac{4}{3}\beta^2 \left(\frac{E_{e^-}}{m_{e^-}c^2}\right)^2 E_{\gamma} \tag{1.5}$$

after the up scattering event. In the above formula, β and E_{e^-} are relative to the electron doing the scattering and E_{γ} is the initial photon energy. This inverse Compton emission can reach into the energy range detectable by VERITAS ($E \gtrsim$100 GeV).

Assuming the leptons are highly relativistic (i.e. $\beta \approx$1) and combining Eq. 1.5 with Eq. 1.3 yields a formula for the magnetic field as a function of the peak frequencies in both the

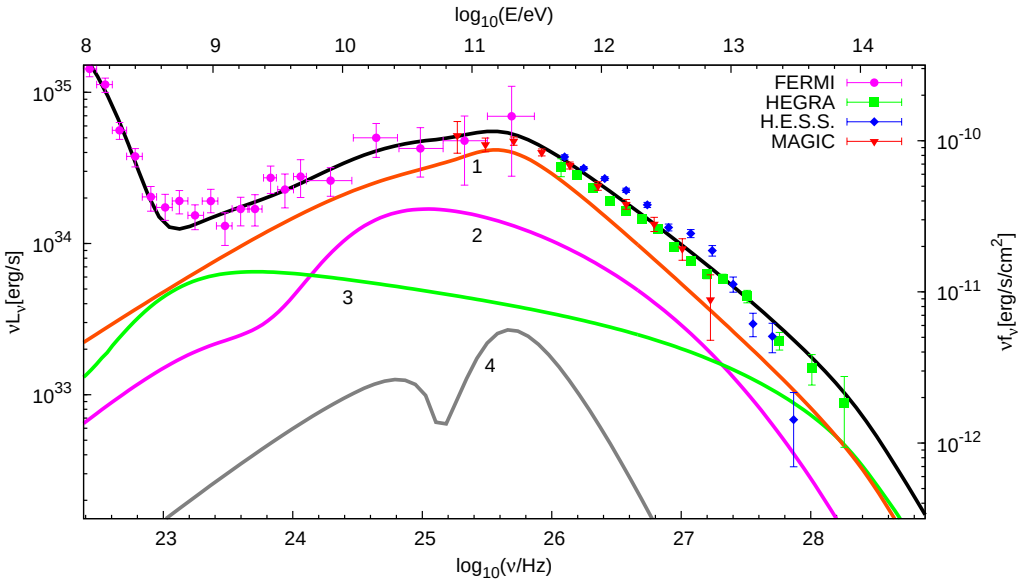

Figure 1.1: Gamma-ray Crab SED reproduced from Meyer et al. (2010). The contribution from inverse compton upscattering of various photon fields are shown: (1) synchrotron, (2) thermal dust, (3) CMB, and (4) line emission from filaments. Black line shows the total contribution from the sum of all components. Data points are taken from various gamma-ray detectors.

synchrotron and IC.

$$B \approx \frac{\nu_{sync}^2}{\nu_{IC}} [\mu\mathrm{G}] \tag{1.6}$$

This demonstrates how observations at GeV and TeV energies provide useful constraints for studying the magnetic field strength in the synchrotron emission environment in SNR.

1.3.3 Bremsstrahlung

Bremsstrahlung emission occurs typically for electrons which interact with the coulomb field of an atomic nucleus or other ions. Because the emission deals with inter-particle interactions, the amount of radiation emitted via bremsstrahlung will scale with the ion density in the medium and the temperature of the electron plasma. This type of emission is more dominant in the X-ray energy regime. At energies above 100 GeV (i.e. energies relevant for VERITAS observations) inverse Compton scattering is typically favored as the emission mechanism for electrons.

1.3.4 Neutral Pion Decay

The dominant gamma-ray emission mechanism for hadrons (protons and atomic nuclei) arises from interactions with ambient material. Proton-proton interactions are believed to be responsible for the bulk of the observed gamma-rays emitted by hadrons in SNR. This interaction chain proceeds in the following chain of particle production an decay.

$$\begin{aligned} p + p &\rightarrow p + p + n\left(\pi^{+} + \pi^{-} + \pi^{0}\right) \\ \pi^{0} &\rightarrow 2\gamma \\ \pi^{\pm} &\rightarrow \mu^{\pm} + \overset{(-)}{\nu}_{\mu} \\ \mu^{\pm} &\rightarrow e^{\pm} + \overset{(-)}{\nu}_{\mu} + \overset{(-)}{\nu}_{e} \end{aligned} \tag{1.7}$$

In the above chain N denotes secondary nucleons produced in the reaction, and n denotes the number of $\pi^{\pm,0}$ produced in the interaction. Due to the large number of produced pions and charge conservation each type of pion is produced in approximately equal amounts. Note that among the products of this interaction will be numerous gamma-ray photons (via π^0 decay) and $e^{\pm}$ (via $\pi^{\pm}$ decay). The energy threshold for the production of π^0 from the interaction of two protons is $E_{p,min} \sim 1.2$ GeV.

For interaction energies much higher than $E_{p,min}$ the reaction products are almost entirely pions. The minimum pion energy necessary to produce a photon with energy E_γ is given by

$$E_{\pi^0,min} = E_\gamma + \left(\frac{m_\pi^2 c^4}{4E_\gamma}\right) \tag{1.8}$$

which implies that for very high energy gamma-rays the minimum required pion energy is comparable with the observed energy of the gamma-ray. This translates into a minimum required proton energy for producing an observed gamma-ray of $\sim 3E_\gamma$. Given that n is most likely more than three, a factor of ten is not unrealistic, meaning that observing 10 TeV gamma-rays would imply at least 100 TeV protons (provided a hadronic origin for the gamma-rays can be established).

An interesting consequence of these interactions is also the large number of neutrinos ($\nu_{\mu,e}$) produced. Detecting high energy neutrinos produced in SNR would provide clear evidence that proton acceleration does occur in such sources. However, because of the almost negligible

interaction cross-section of neutrinos with matter, relative to the cosmic-ray cross-section, such a detection is not feasible with the current or planned IACT instruments.

1.4 Sources of High Energy Gamma-ray Emission

Test!

Gamma-ray emission is produced in a host of different sources. Objects capable of producing photons at TeV energies from within our galaxy include pulsar wind nebulae (PWN), supernova remnants (SNR), binary systems, and pulsars. Gamma-rays are also emitted by relativistic particles in the jets emanating from the nuclei of external galaxies. There are also theorized exotic sources of TeV gamma-rays, such as self annihilation of dark matter. Gamma-ray bursts are also believed to produce radiation above 1 TeV, however so far no gamma-ray burst has been observed by IACTs.

1.4.1 Extra Galactic

Cosmic-rays can come to the Earth from outside the galaxy. Active nuclei of distant galaxies are a posited source of extra-galactic cosmic-rays. They are known particle accelerators and bright in gamma-rays. Active galactic nuclei (AGN) can be broken into multiple types (Urry and Padovani (1995)).

- **Type 1** - Bright continuum spectra with broad emission lines. Emission originates from hot gas deep within the gravity well, near the central compact object.
- **Type 2** - Weak continuum spectrum with narrow emission lines. Emission is mostly blocked by thick gas around the core of the AGN.
- **Type 0** - Characterized by pecular spectral features. BL Lacertae (BL Lac) objects are a subset of this type. BL Lacs are characterized by bright radio emission and lacking bright emission and absorption lines.

The different types are primarily based on the random orientation of the AGN. Both Type 1 and Type 0 are believed to be AGN for which the observation angle is nearer to 0°, meaning the line of sight is directly in line with one of the jets. AGN in which the line of sight coincides

almost directly with one of the jets are referred to as *blazars*. Type 2 AGN, however, are believed to be AGN where the line of sight is at a large inclination angle from the jets.

Emission from an AGN is typically believed to originate from leptons accelerated in the outflowing material within the jets. Observations of synchrotron emission in X-ray coupled with inverse Compton emission at TeV energies seems to suggest this as the most likely source of the emission. The photons up scattered in the inverse Compton emission can come either from the synchrotron photons emitted by the same leptons (referred to as *synchroton self Compton*) or from other external sources Ghisellini et al. (1998). However, it should be noted that a hadronic origin of the emission has not been ruled out.

1.4.2 Supernova Remnants

When a massive star exhausts the fuel in its core, the resulting explosion is known as a supernova[5]. This explosion can leave behind a rapidly rotating neutron star, known as a *pulsar*. The explosion also sends out a shockwave into the surrounding interstellar medium (ISM). As the shockwave expands the ejected material forms a supernova remnant (SNR).

The evolution of a SNR (more specifically a shell-type SNR) can be roughly described in four phases (Rosswog and Brüggen, 2007). In the first phase, the velocity of the shockwave is approximately constant, given by

$$v_{ej} \sim 10^4 \left(\frac{E_{SN}}{10^{51}\text{erg}}\right)^{1/2} \left(\frac{M_{ej}}{M_\odot}\right)^{-1/2} [\text{km s}^{-1}] \tag{1.9}$$

where E_{SN} is the initial energy of the supernova and M_{ej} is the total mass of the ejected material. During this phase the remnant sweeps up material from the interstellar medium. The second phase generally begins about the time the remnant has swept up as much mass as the mass initially ejected. Because of this, the approximate duration of the first phase can be computed via

$$t_1 \sim 200 \left(\frac{E_{SN}}{10^{51}\text{erg}}\right)^{-1/2} \left(\frac{M_{ej}}{M_\odot}\right)^{5/6} \left(\frac{\rho_{ISM}}{10^{-24}\text{g cm}^{-3}}\right)^{-1/3} [\text{yr}] \tag{1.10}$$

where ρ_{ISM} is the density of the surrounding ISM. During this phase the energy of the expanding wave is approximately constant, as the energy lost due to radiation is still small in

[5]Note that Type Ia supernova, resulting from a white dwarf accreting matter from a nearby companion beyond the Chandrasekhar limit, can also lead to an expanding remnant. See for example high energy observations of the Tycho SNR (Acciari et al., 2011; Giordano et al., 2012).

comparison to the energy of the expanding shell. The second phase is sometimes referred to as the *Sedov* phase because of this and typically lasts several to a few tens of thousands of years. In this phase the SNR can emit bremsstrahlung radiation strongly in X-rays. It is during these first two phases that the bulk of the cosmic-rays accelerated by the shock are emitted.

As the shell begins to cool, its outward motion becomes driven by an internal hot gas. During this phase the remnant emits strong line emission in the optical regime. The momentum of the expanding shell during is approximately constant. As the shell continues to expand it piles up surrounding material, leading to this being referred to as the *snowplow* phase. The final phase begins when the shell reaches an equilibrium with the surrounding ISM, effectively merging with the ISM. This occurs when the SNR is approximately a few times 10^5 years old. In these later stages, high energy emission observed from the SNR is dominated by leptons in the inner hot gas region, as most of the cosmic-ray protons and atomic nuclei at the shell are believed to have escaped.

The above is a reasonable description of a shell-type SNR. For a *filled-center* SNR, such as the Crab nebula, the dynamics of its evolution will differ. This is primarily due to the central engine of the remnant which serves as both a source of energy and high energy particles. For this reason, shell-type SNR are typically favored for studying the acceleration and emission of cosmic-rays from SNR shocks.

1.4.3 Pulsars

Hewish et al. (1968) reported the first detection of a pulsar, observed as a rapidly pulsating source of radio emission with a period of 1.337 s. The common theory explaining this emission is that it is the result of a compact, rapidly rotating neutron star. Electromagnetic radiation is emitted in a narrow beam from the magnetic poles. If the Earth falls within the path of this beam, the observed signal will appear to peak at regular intervals as a result of the beam sweeping over the Earth. Because of the fast rotation, the neutron star produces intense magnetic fields of the order 10^{12} G. These fields co-rotate with the neutron star. Because of the fast rotation of the star, at a certain distance (R_{lc}) the co-rotation velocity approaches the

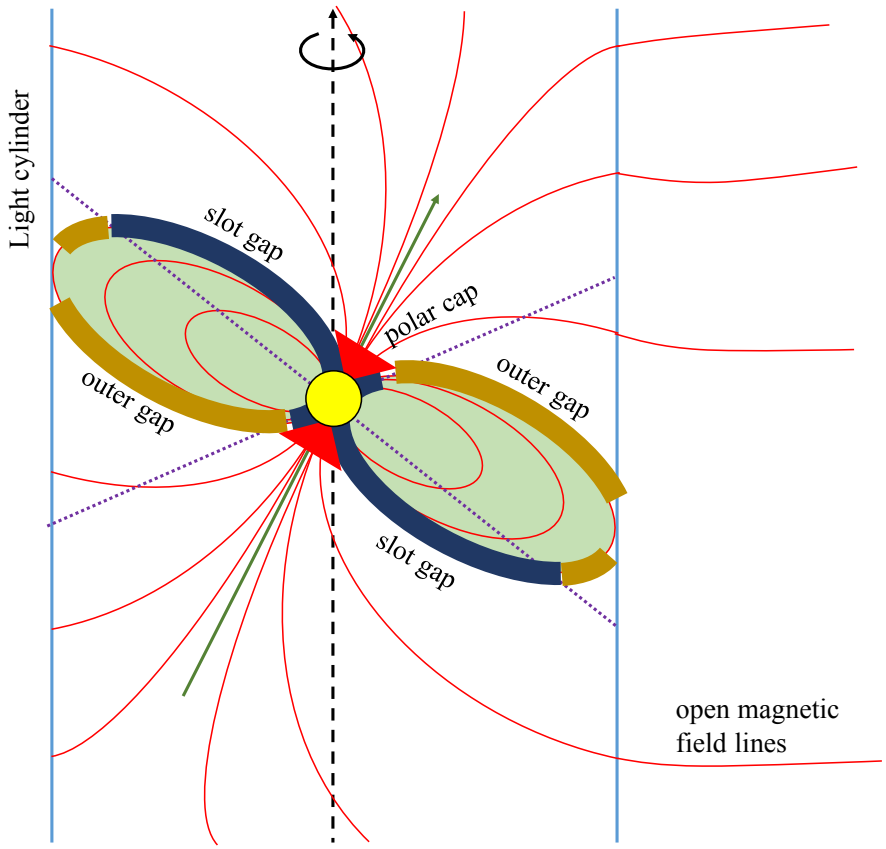

Figure 1.2: Diagram of a pulsar showing the compact neutron star (yellow circle), magnetic field lines (red lines), and boundaries of the light cylinder (blue lines). The null surface is indicated by the purple dotted lines. The various proposed regions of high energy emission are also labeled.

speed of light (c). This distance is given by

$$R_{lc} = \frac{cP}{2\pi} \tag{1.11}$$

where P is the rotation period of the observed pulsar. The magnetic fields that would have extended beyond this distance become open field lines.

The mechanisms for high energy emission from pulsars is still poorly understood, however several models have been suggested. One of the early theories, called the *polar cap* model, puts forth that the emission originates from electrons streaming from the magnetic field poles (Harding et al., 1978; Daugherty and Harding, 1982). This model predicts a high energy cutoff $\lesssim 10$ GeV, however recent observation by the VERITAS and MAGIC observatories have detected emission from the Crab pulsar at a few tens of GeV up to 1.5 TeV (Aliu et al., 2011;

Ansoldi et al., 2016).

The *slot gap* model moves the acceleration region from the pole to the last open field line extending from the stars surface to the null surface[6] (Muslimov and Harding, 2004). Still another model, the *outer gap* model, defines the acceleration region as extending along the last open field line from the null surface to the light cylinder (Romani and Yadigaroglu, 1995). These regions are shown in Fig. 1.2. Regardless of where the acceleration region is located, the mechanism is typically the same. High energy electrons propagate along the intense field lines, emit high energy photons via curvature radiation, and these high energy photons then pair produce on the intense magnetic fields.

1.4.4 Pulsar Wind Nebulae

Despite the high energy output of the pulsed emission, pulsars dissipate most of their rotational energy through a relativistic particle wind (Gaensler and Slane, 2006). The wind is comprised primarily of electrons and positrons that have escaped the light cylinder. Initially the energy of the wind is dominated by the electromagnetic energy flux, however as the wind expands the particles will lose energy and the energy is converted into the kinetic energy of the particles. The electrons and positrons contained in this wind spiral along the open magnetic field lines and emit synchrotron radiation creating a pulsar wind nebula (PWN). Eventually these particles interact with the reverse shock, caused by the rebounding material from the SNR shock wave interacting with the ISM. The reverse shock effectively terminates the pulsar wind. The particles in the wind are then accelerated and their pitch angles become randomly scattered giving rise to emission in all directions.

These synchrotron leptons can also scatter lower energy photons to high energies. This is known as inverse Compton emission (see §1.3.2). The source of these low energy photons can be nearby starlight or even the cosmic microwave background (CMB). This emission is typically what gamma-ray instruments observe. Over time as the surrounding SNR dissipates the leptons that are confined by the reverse shock will be free to diffuse into the surrounding interstellar medium.

[6]The null surface is defined as the line which runs through the points along the magnetic field lines which point perpendicular to the rotation axis.

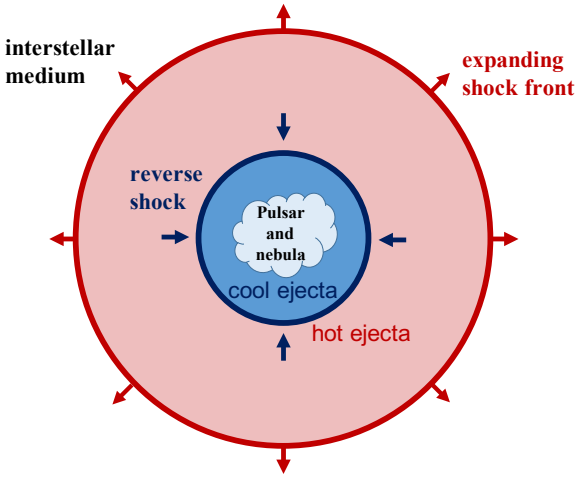

Figure 1.3: Diagram of a SNR showing the expanding shock front and the PWN.

1.5 Select Gamma-ray Detectors

1.5.1 *Fermi*-LAT

The *Fermi* Large Area Telescope (*Fermi*-LAT) is a space based observatory sensitive to gamma-ray photons with energies from 20 MeV to 300 GeV[7] (Acero et al., 2015). The *Fermi*-LAT space telescope was launched in 2008 and has been taking data with an approximate duty cycle of 76%. As of the 3FGL catalog, the *Fermi*-LAT point spread function (PSF) changes dramatically over its sensitive energy range from about 5° at 100 MeV, decreasing to 0.8° at 1 GeV, and reaches its narrowest of 0.2° around 20 GeV and above. The collection area of the instrument is ∼6500 cm^{-2} with a field of view of 2.4 sr at 1 GeV. The standard orbit of *Fermi* allows it to observe the entire sky every ∼3 hours during normal observations.

The *Fermi*-LAT instrument consists of an anticoincidence shield, a tracking section, and a calorimeter. The tracking section is comprised of 36 layers of silicon strips. These silicon strips are interleaved with 16 layers of tungsten foil, 12 thinner layers in the front end of the detector and 4 thicker layers on the back end. At the bottom of the detector sits a CsI calorimeter. When a high energy gamma-ray enters the detector, it will pass freely through the anticoincidence shield, and enter the tracking section. Here it will interact with the tungsten foil producing

[7]This energy range can be somewhat expanded using dedicated analysis techniques. E.g. see Ackermann et al. (2016) which reports detection of sources above 1 TeV.

an electron-positron pair. This pair then travel the remaining length of the tracking section depositing energy into the silicon strips as they go. This allows the detector to reconstruct the path of the charged particles through the detector, which can then be used to detemine the incident direction of the initiating gamma-ray. Once the pair reach the bottom they deposit their remaining energy into the calorimeter which allows the initiating gamma-rays energy to be determined. Charged particles will have the same effect except that when they pass through the coincidence shield they produce a flash of light identifying that the initiating particle was actually a charged cosmic-ray and not a gamma-ray. Thus the anticoincidence shield allows the *Fermi*-LAT instrument to separate the large cosmic-ray background from the gamma-ray signal.

Fermi is also equipped with a gamma-ray burst monitor (GBM) (Connaughton et al., 2015). The GBM consists of 12 sodium iodide detectors sensitive from 8 keV to 1 MeV, and two bismuth germanate scintillators sensitive from 200 keV to 40 MeV. These detectors are situated inside the satellite to provide a 7 sr view of the sky. When a burst is observed, the detector repositions the LAT detector to observe the burst. Due to the brief nature of gamma-ray bursts, an notification is also issued to the astronomical community to alert telescopes around the world of this event.

1.5.2 Imaging Atmospheric Cherenkov Detectors

IACT arrays are ground based observatories. The multiple telescopes observe the Cherenkov radiation produced by charged particles moving through the atmosphere and the resulting images are combined to reconstruct the origin of the initiating particle on the sky. The benefits of an IACT array over a single telescope is the more precise reconstruction of the event sky position and shower properties. This yields a narrower PSF and more accurate measurement of the initiating particles energy. One such array, VERITAS, has a resolution of $<0.07^{\circ}$ above 1 TeV. VERITAS observes photons from $\sim$85 GeV to greater than 30 TeV and is capable of reconstructing the energy of the initiating gamma-ray to within 15% - 20% (Park and VERITAS Collaboration, 2015).

Currently there are three main IACT arrays in operation. These are operated by the

H.E.S.S. (Becherini et al., 2012), MAGIC (Lotto and the Magic Collaboration, 2012), and VERITAS collaborations. Because the technique at the focus of this dissertation is specifically developed and implemented for the VERITAS array, more details will be given regarding this detector in later chapters. Specifically, the telescope hardware and operations are described in Chapter 3 with an overview of standard data analysis techniques given in Chapter 4.

1.5.3 High Altitude Water Cherenkov Detector

The High Altitude Water Cherenkov (HAWC) Observatory is a recently completed detector in central Mexico sensitive to gamma-ray photons in the energy range of 1-100 TeV (Smith, 2015). The detector consists of an array of 300 tanks filled with water, which serves as the medium through which Cherenkov light is produced as charged particles pass through the tanks. As a result, the observed particle showers must reach the ground in order to be observed by HAWC, making the detector sensitive to showers produced by gamma-rays of much higher energies compared to IACTs. The detector is also located at high altitudes (4100m above sea level) to reduce the energy threshold as compared to previous generations of water Cherenkov instruments, such as Milagro.

The main benefit of such a detector over an IACT array is derived from the fact that the Cherenkov producing medium and PMTs are contained within a light-tight enclosure. This allows the detector to operate continuously even during the day. The detector is also able to observe events from a large fraction of the sky simultaneously, an important quality due to the low flux rate of photons at these energies. As particles produced in the shower pass through the array, the timing of individual PMT triggers can be used to reconstruct the initiating particle's direction of origin on the sky. The resulting HAWC angular resolution is reported to be between about 0.5° around 1 TeV to $\lesssim 0.2^\circ$ above 10 TeV with an energy resolution less than 50% above 10 TeV (Abeysekara et al., 2013).

The next chapter will focus on two current open questions in gamma-ray astronomy. These are the observed anomalous positron fraction and the mechanisms by which cosmic-rays are accelerated in supernovae and diffuse into the galaxy.

CHAPTER 2. SCIENTIFIC MOTIVATION

VERITAS has made a number of important contributions to the field of high energy gamma-ray astronomy. However, as will be outlined in §4.3.3 most of the studies with VERITAS are limited to sources of modest extension ($\lesssim 0.3^\circ$ in radius). This limits the degree to which VERITAS can contribute to the study of gamma-ray sources with extensions much greater than this. As was mentioned in Chapter 1, IACTs are sensitive in an energy range which complements both the lower energy *Fermi*-LAT space telescope and the higher energy HAWC detector.

2.1 Synchrotron & Inverse Compton Emission in PWNe

As the injected electrons within a PWN travel outward they will lose energy. Eq. 2.1 gives the characteristic time for a synchrotron electron to lose approximately half of its energy through synchrotron emission.

$$T_{c,sync} = 5.1 \times 10^8 \left(\frac{B}{[\mathrm{G}]}\right)^{-2} \left(\frac{mc^2}{E}\right) [\mathrm{s}] \tag{2.1}$$

Higher energy electrons will emit their synchrotron emission in X-rays. The inverse relation with energy in Eq. 2.1 suggests these electrons will have a much shorter emission timescale than lower energy electrons which emit synchrotron in the radio. Assuming a power-law spectrum, and considering the finite emission lifetime of the electrons injected into the nebula, the emission spectrum will exhibit a cutoff at a frequency (and corresponding electron energy) given by Eq. 2.2.

$$\begin{aligned} \nu_{cutoff} &= 3.1 \times 10^{23} \left(\frac{B}{[\mathrm{G}]}\right)^{-3} \left(\frac{t}{[\mathrm{s}]}\right)^{-2} [\mathrm{Hz}] \\ E_{cutoff} &= 2.6 \times 10^{14} \left(\frac{B}{[\mathrm{G}]}\right)^{-2} \left(\frac{t}{[\mathrm{s}]}\right)^{-1} [\mathrm{eV}] \end{aligned} \tag{2.2}$$

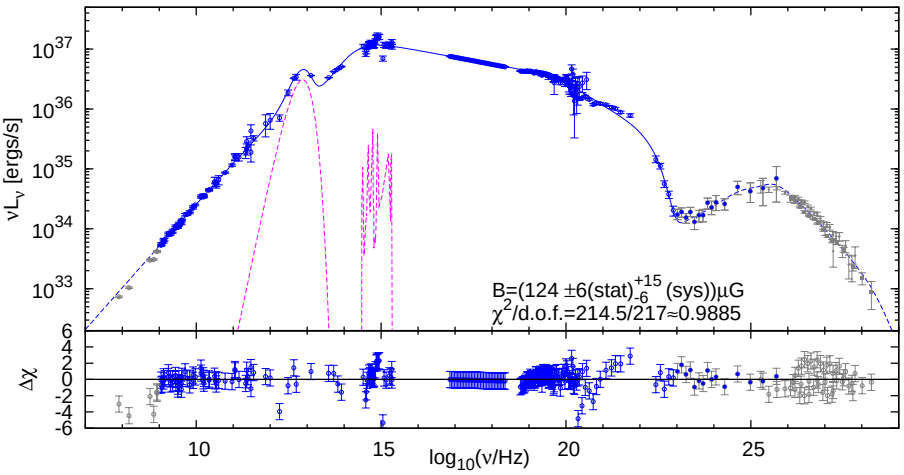

Figure 2.1: Crab SED reproduced from Meyer et al. (2010). The observed spectral cutoff between 10^{14}-10^{15} Hz is predicted from Eq. 2.2 based on emission from synchrotron electrons, the best fit magnetic field, and the age of the nebula. Gray points represent inverse Compton emission observed by high energy instruments including *Fermi*-LAT, H.E.S.S., HEGRA, and MAGIC.

The emission spectrum will increase below this frequency, while above it the emitted energy will begin to decrease. Observations in the radio can probe the regions below and around this frequency, and X-ray observations probe the spectrum above this cutoff. Electrons which emit radiation at frequencies above this cutoff will reach the outer region of the nebula in ever decreasing numbers. This leads to differing observed morphologies in the remnant when comparing radio and X-ray observations.

For example, using numbers derived for the Crab nebula of $B \approx 124$ μG (Meyer et al., 2010) and an age $t \approx 10^3$ years the estimated turnover occurs at $\nu_{cutoff} \approx 10^{14}$ Hz, or an electron energy of $E_{cutoff} \approx 5\times10^{11}$ eV (see Fig. 2.1). The observed morphology of the infrared emission as compared to the X-ray emission can be viewed in Fig. 2.2. This image shows that the X-ray synchrotron emission, which suffers energy losses at a more rapid rate, has a more compact morphology than the radio emission, which loses energy much slower and can travel farther. As the X-ray emitting electrons lose energy they begin to emit in optical and ultimately radio wavelengths.

Studying the synchrotron emission in the radio to ultraviolet and the inverse Compton

Figure 2.2: Composite image of the Crab nebula combining data taken in different wavelengths: (*purple*) infrared (NASA/JPL-Caltech/Univ. Minn./R.Gehrz), (*red* & *yellow*) Optical (NASA/ESA/ASU/J.Hester & A.Loll), (*blue*) X-ray (NASA/CXC/SAO/F.Seward). The image shows the different morphology of the Crab nebula in the lower energy infrared and optical as compared to the higher energy X-ray emission.

in the gamma-ray regime provides the most complete image of the leptonic emission yielding information about the particle population, the energy of the leptons, and the strength of the magnetic field.

2.2 Positron Excess and Geminga

2.2.1 Positron Excess

A number of space observatories including PAMELA (Adriani et al., 2009), AMS (Aguilar et al., 2013), and *Fermi*-LAT (Ackermann et al., 2012) have observed a local enhancement of the total number of positrons to the combined number of electrons and positrons ($e^+/(e^+ + e^-)$) referred to as the *positron fraction* (see Fig. 2.3). One potential origin for this excess is dark matter annihilation (Cholis et al., 2009; Feng et al., 2014) in which dark matter particles annihilate into light bosons which can decay through various channels, the result of which are elections and positrons.

Another explanation for the observed excess involves pulsars and PWNe (Hooper et al.,

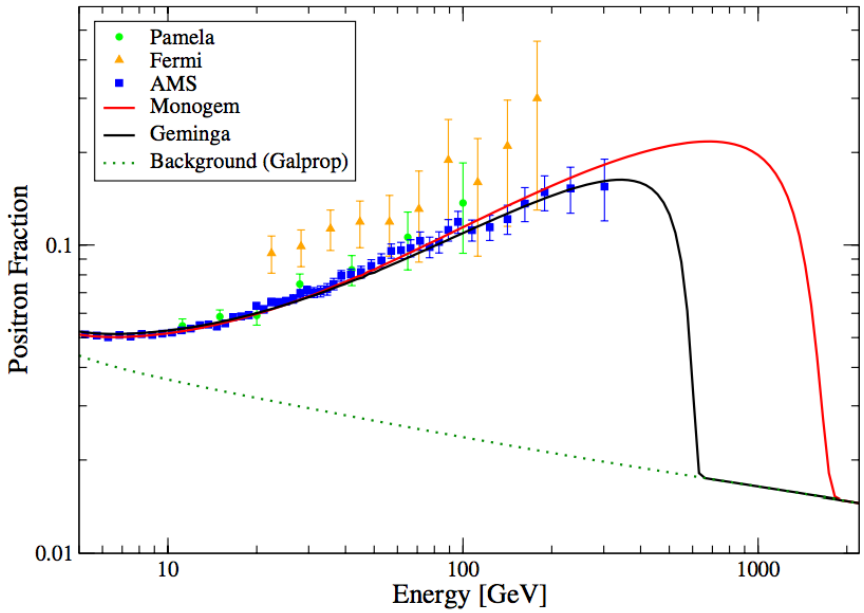

Figure 2.3: Positron fraction shown as a ratio of the flux of positrons to the total flux of electrons and positrons ($e^+/(e^-+e^+)$). Shown are the proposed contributions in a Geminga origin and Monogem origin scenario. Image reproduced from Linden and Profumo (2013).

2009; Yüksel et al., 2009). This theory states that as a supernova remnant ages its surrounding nebula will dissipate. Once this occurs there is no longer a reverse shock to confine the high energy electrons within the PWN. The electrons are then free to diffuse into the surrounding medium where they can be detected directly. Geminga's close proximity and age make it a possible origin of the local positron fraction. Yüksel et al. (2009) claim that the observed extended emission as seen by Milagro is evidence of high energy electrons and positrons with energies up to a minimum of 100 TeV. The lack of a radio or x-ray nebula of consistant with the Milagro emission also suggest the surrounding nebula has dissipated. A result is that the high energy leptons are no longer confined to the source and are able to diffuse into the surrounding interstellar medium. The small distance to Geminga suggests that leptons accelerated in Geminga's more energetic past could also have made it to the Earth by present day.

One feature of the resulting particle spectrum is a cutoff at high energies (see Fig. 2.3). This cutoff is the result of inverse Compton and synchrotron losses experienced by the particles as they are diffusing through the interstellar medium. Linden and Profumo (2013) describe the

cutoff energy scaling as

$$E_{loss} \simeq \frac{1}{b_0 T} \tag{2.3}$$

where T is the time since particle injection. Taking b_0=1.4x10^{-16} GeV^{-1} s^{-1}, Eq. 2.3 produces a cutoff of E_{loss} ≃750 GeV for T=300 kyr and E_{loss} ≃750 GeV for T=1 Myr. An additional cutoff is also derived which relates to the diffusion of the emitted leptons into the interstellar medium over time. This scales as

$$exp\left(-\left(\frac{d}{r_{diff}(E)}\right)^2\right) \tag{2.4}$$

where d is the observers distance from the source and $r_{diff}(E)$ is an energy dependent diffusion length. The resulting spectrum can be modeled as an exponentially cutoff power law of the form

$$f(E) = f_0 E^{-\Gamma} exp\left(\frac{E}{E_{cut}}\right) \tag{2.5}$$

Linden and Profumo suggest that IACTs can potentially contribute through targeted observations on the Geminga and Monogem pulsars. The observed gamma-ray flux surrounding the pulsar in the IACT energy range could provide a substantial constraint on the flux of leptonic emission from these sources. In order for these observations to be of use, a technique would need to be implemented that can handle the scale of these sources. More importantly, being able to detect an energy dependent morphology in a source like Geminga would provide evidence to favor or disfavor Geminga as a potential origin of the positron excess.

2.2.2 Pulsar Detection and Characterization

In 1972 the Second Small Astronomy Satellite (SAS-2) detected significant emission at galactic coordinates l=194.9°(±1.5°), b=4.9°(±2.2°), near the galactic anticenter (Thompson et al., 1977). The early discovery noted that the source appeared to emit a significant amount of its radiation above 100 MeV with no known counterpart in other wavelengths. It was subsequently nicknamed *Geminga*[1]. Bignami et al. (1983) later found an X-ray counterpart and concluded that due to its compact size and high luminosity a neutron star was the most

[1]A footnote of Bignami et al. (1983) states that due to the location of the source in the constellation Gemini and its lack of a counter part in other wavelengths, the source was given the name *Geminga* which means "it's not there" or "does not exist" in the Milanese dialect.

probable source candidate, however no pulsed emission was detected at the time. Thus, the nature of Geminga was left to speculation until ROSAT discovered pulsed emission with a period of 237 ms establishing Geminga as a rapidly spinning neutron star (Halpern and Holt, 1992). More recently, observations by Faherty et al. (2007) have established an approximate distance to Geminga of 250^{+120}_{-62} pc through parallax measurements using the Hubble Space Telescope. Manchester et al. (2005) have also derived a characteristic age for the pulsar of 342 kyr by relating the pulsar's period and first period derivative.

The Geminga pulsar has also been observed in *Fermi*-LAT data (Abdo et al., 2010). Geminga appears as the second brightest gamma-ray source in the *Fermi*-LAT data. The resulting spectrum of the pulsar was found to follow an exponentially cutoff power law of the form

$$\frac{dN}{dE} = N_0 E^{-\Gamma} exp\left(\frac{E}{E_0}\right) \tag{2.6}$$

with $N_0 = 1.189$ ($\pm 0.013_{stat} \pm 0.070_{sys}$) x$10^{-9}$ GeV^{-1}cm^{-2}s^{-1}, $\Gamma = 1.30$ ($\pm 0.01_{stat} \pm 0.04_{sys}$), $E_0 = 2.46$ ($\pm 0.04_{stat} \pm 0.17_{sys}$). It should be noted, that in *Fermi*-LAT data there is no evidence for extended emission surrounding the Geminga pulsar.

2.2.3 TeV Observations of Geminga

Milagro reported observations of the region around the Geminga pulsar finding evidence of an extended region of emission (Abdo et al., 2009b). The source, MGRO C3, was initially analyzed as a point source giving a 3.5σ significance, below the detection threshold of the instrument. However, the resulting excess suggested the source may be extended leading researchers to reanalyze the data by convolving the Milagro point spread function with a 1° Gaussian. This lead to a significant detection of 6.3σ and the first claim of TeV emission from the region surrounding the Geminga pulsar. Fitting the spatial data with a Gaussian yields a region with extension of approximately $1.30^\circ \pm 0.2^\circ$. This translates into a source with full width at half max of $2.6^{+0.7}_{-0.9}$ after accounting for the Milagro PSF. Combining this large extension with the estimated distance to Geminga provides an estimate for the size of the emission region of approximately 5-10 pc.

Data from the Tibet-III air shower array was also used to search for emission near the

Geminga pulsar. This analysis yielded a peak significance of 2.2σ, implying no detectable emission (Amenomori et al., 2010). However, a recent analysis from the HAWC observatory by Baughman et al. (2015) reported evidence of extended emission consistent the Milagro result. No details regarding the HAWC detection significance or spectrum were provided in this study.

Aliu et al. (2015) analyzed approximately 71.6 hours of data from the VERITAS detector covering multiple epochs to search for pulsed emission from Geminga, but was only able to derive an upper limit to the integral flux above 135 GeV of 4.0 x 10^{-13} photons cm^{-2} s^{-1}. Most recently, the MAGIC observatory attempted a search for pulsed and extended emission from the Geminga pulsar and surrounding region (Ahnen et al., 2016). However, in 63 hours of good quality data the detector was only able to place upper limits of 5.3 x 10^{-13} TeV^{-1} cm^{-2} s^{-1} for the pulsed emission and 3.5 x 10^{-12} TeV^{-1} cm^{-2} s^{-1} for the surrounding nebula at 50 GeV. These limits are currently the most constraining for energies which VERITAS is sensitive to.

2.3 Mapping Particle Acceleration and Diffusion in SNR

2.3.1 Cosmic-ray Spectrum

Current observations of the energy distribution of cosmic-rays from various detectors shows a spectrum with several features (see Fig. 2.4). The spectrum is typically viewed as a power law with the index changing at each of these features. Two features that are generally agreed upon by most studies occur at around 3×10^{15} eV (the *knee*) and $10^{18.5}$ eV (the *ankle*). The ankle feature is generally believed to be the result of a change in the origin of the cosmic-rays observed. Cosmic-rays below the ankle are believed to be produced predominantly within the Milky Way galaxy while those above the ankle are believed to originate from extra-galactic sources.

Although cosmic-rays around the knee are believed to originate from within the galaxy, there have been multiple explanations for where they originated. The prevailing theory is that galactic cosmic-rays are accelerated in SNR shocks. Indeed, as little as 10% of the overall energy from a supernova remnant would be necessary to account for the observed galactic cosmic-ray background (Drury et al., 1989). Detailed simulations of SNR shocks predict that such an

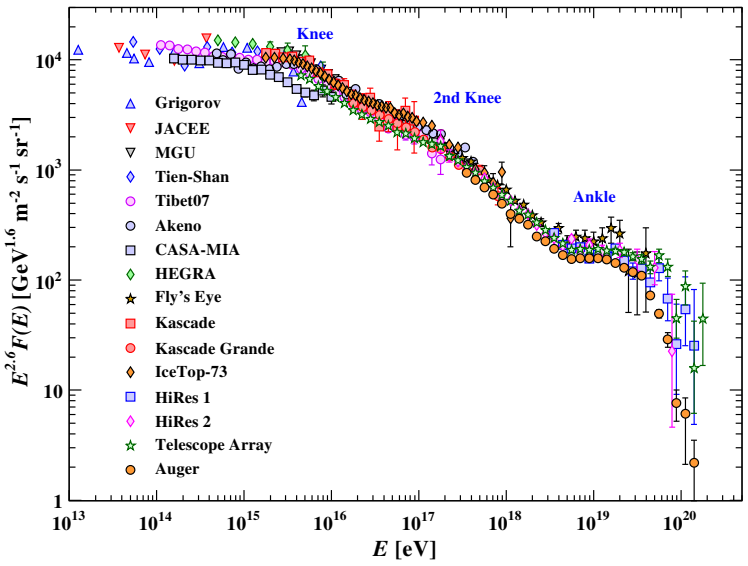

Figure 2.4: Cosmic-ray energy spectrum for all particles reproduced from Olive et al. (2014).

acceleration efficiency is well within the realm of possibility (Malkov and Drury, 2001).

It is generally accepted that SNR are capable of accelerating protons to significant energies through the process of DSA. A recent study of W44 and IC443 by Ackermann et al. (2013) detected a low energy gamma-ray cutoff in *Fermi*-LAT data, providing evidence of proton acceleration in these SNR (see Fig. 2.5). The cutoff they observed occurs just below 100 MeV, roughly half the rest mass energy of a decaying π^0 particle ($m_{\pi^0}c^2$=135.0 MeV) suggesting the emission has a significant hadronic component. Studies of the high energy emission from the Tycho SNR, the remnant of a Type Ia supernova, tend to favor a hadronic origin of the emission as well (Acciari et al., 2011; Giordano et al., 2012). However, whether SNR actually accelerate cosmic-rays up to PeV energies, consistent with the observed spectral *knee* in the cosmic-ray spectrum, is still an open question. Specifically, observational evidence showing cosmic-ray acceleration up to the knee is needed.

An important source class in studying cosmic-ray acceleration in SNR shocks are shell-type SNR. These are SNR who's outer shell (i.e. the shock region) can be directly observed. Several shell-type SNR have been detected by the H.E.S.S. observatory. These include (but

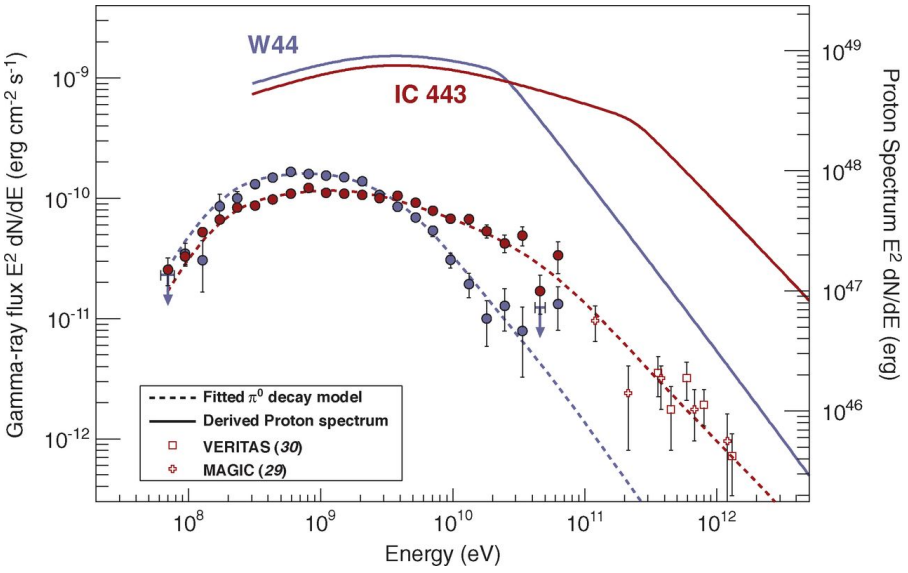

Figure 2.5: Low energy cutoff observed in *Fermi*-LAT data from the IC443 and W44 SNR. The feature is indicative of the decay of π^0 produced in *pp* interactions. Image reproduced from Ackermann et al. (2013).

are not limited to) SNR G347.3 - 0.5 (Aharonian et al., 2004), RX J0852.0-4622 (Aharonian et al., 2007), RCW 86 (Aharonian et al., 2009), SN 1006 (Acero et al., 2010), HESS J1731347 (Abramowski, A. et al., 2011), and RX J1713.7-3946 (Aharonian et al., 2006). The success of the H.E.S.S. instrument in achieving these detections comes both from it's larger field of view ($\sim 5^\circ$ across) and a dedicated survey of a large portion of the galactic plane. Such sources allow studying directly the shock front region where gamma-ray emission takes place. The amount of gamma-ray emission observed in the shock front region provides insight regarding the population of hadrons and/or leptons producing the emission.

An updated analysis of the H.E.S.S. data on RX J1713.7-3946 presented by Abdalla et al. (2016) demonstrates how detailed studies of shell-type SNR at TeV energies contributes to our knowledge of cosmic-ray acceleration. Researchers observed a broader extension of the TeV emission as compared to the X-ray emission from certain regions of the remnant. One interpretation of this is the TeV gamma-ray emitting particles are actually leaking out of the shock in these regions. Efforts to model the observed spectrum as derived from either a purely leptonic, purely hadronic, or combined particle population were unable to describe the data unambiguously. Earlier analysis by Aharonian et al. (2006) favor a hadronic origin, but were

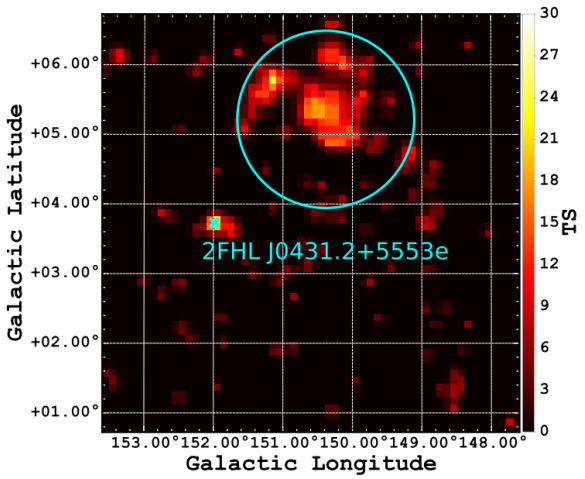

Figure 2.6: TS map of the *Fermi*-LAT source 2FHL J0431.2+5553e reproduced from Ackermann et al. (2016). The teal circle represents the extent of the best fit disk of radius 1.27°±0.04°.

also unable to rule out a leptonic origin.

2.3.2 *Fermi*-LAT Source 2FHL J0431.2+5553e

A recent analysis of ∼80 months of *Fermi*-LAT data from 50 GeV up to 2 TeV resulted in the publication of the second *Fermi*-LAT catalog of hard spectrum sources (2FHL, Ackermann et al. (2016)). The energy range covered by the catalog suggests these sources could possibly be detected by IACTs. Indeed, at the time of publishing ∼25% of the reported sources already had associations in IACT data. One source in particular, 2FHL J0431.2+5553e, was found to have an extension of 1.27°±0.04°. The source is located at Galactic coordinates l=150.384, b=5.216, well within the observing capabilities of the VERITAS instrument (see Fig. 2.6). The *Fermi*-LAT integrated spectrum from 50 GeV to 2 TeV is 11.70 (± 2.11) $\times 10^{-11}$ photon cm^{-2} s^{-1} with a spectral index of -1.66 ± 0.20. This implies a flux normalization of $\sim 1.17 \times 10^{-7}$ TeV^{-1} m^{-2} s^{-1}. Such a hard spectrum would seem to suggest that VERITAS should be able to observe this source as the emission would still be fairly strong into the high energy regime. However, it is more realistic to expect that such a hard spectrum would at some point turn over and the spectrum would become softer at higher energies making the flux at VERITAS energies lower than that predicted above.

2FHL J0431.2+5553e has an associated source at radio wavelengths (SNR G150.3+4.5)

reported by Gao and Han (2014). Gao and Han describe the emission as a 2.5°×3.0° shell. Combined with the non-thermal nature of the emission, a shell-type SNR was found to be the must likely origin of the source.

VERITAS currently has ∼22.5 hours of data on or overlapping the region around 2FHL J0431.2+5553e. However, current analyses are unable to assess whether the data contains emission from such a highely extended source. This will be demonstrated in section §4.3.4 by processing the data through the standard ring background analysis. Instead, new techniques will be necessary for studying such a highly extended source.

2.4 Summary

Both Geminga and 2FHL J0431.2+5553e are highly extended sources. Geminga represents a source of potentially leptonic emission while the emission from 2FHL J0431.2+5553e is most likely a combination of hadronic and leptonic in origin. As mentioned above, detecting the spatial morphology of these two sources would provide a valuable constraint on the positron fraction and help study cosmic ray acceleration and diffusion. In order to do this a new analysis technique is necessary for studying such highly extended sources. One such technique for VERITAS will be presented in Chapter 5.

CHAPTER 3. VERITAS: DESIGN AND OPERATION

This chapter provides an overview of the VERITAS observatory and how it collects data. The chapter begins with a description of the relevant processes for high energy particles which interact with atoms in the Earth's atmosphere. The cascade of high energy particles produced in these interactions go on to emit a detectable Cherenkov radiation signal. Details are then provided regarding how this radiation is observed by the individual telescopes in the array. The chapter concludes with an overview of the instrument hardware and details regarding the maintenance and calibration of the the telescope mirrors and photo-multiplier tubes (PMTs).

3.1 Extensive Air-showers

3.1.1 Gamma-ray Induced Air-showers

VERITAS studies photons with energies above ∼85 GeV. Particles above this energy will be screened from ground based observatories due to interactions with atomic nuclei in the Earth's atmosphere. These gamma-rays will ultimately be converted into an electron-positron ($e^{\pm}$) pair. This occurs through a process known as Coulomb pair production[1] which arises due to the interaction of the photon and the Coulomb field of an atomic nucleus. The approximate cross section of this interaction is given by Eq. 3.1.

$$\sigma_{pair} = \frac{7}{9}\left(\frac{A}{\chi_0 N_A}\right) \tag{3.1}$$

Here, A is the atomic mass number of the atoms in the atmosphere, N_A is Avogadro's number, and χ_0 is the approximate radiation length[2] in units of $g{\cdot}cm^{-2}$. Using standard estimates

[1] Pair production is the dominant form of energy loss for photons with energy above ∼100 MeV.

[2] The radiation length is typically interpreted as the distance an electron can travel on average before losing all but $1/e$ of its energy.

for the composition of the Earth's atmosphere, σ_{pair} is approximately of the order 10^{-25} cm^2 (Grieder, 2010a).

As the produced $e^{\pm}$ move through the atmosphere they will also lose energy through the following mechanisms:

- **Bremsstrahlung Radiation:** Radiation emitted due to $e^{\pm}$ interactions with the Coulomb field of atomic nuclei.
- **Ionization:** Interactions with electrons in atoms including ionizing or excitation.

Bremsstrahlung radiation is the dominant mode of energy loss for $e^{\pm}$ at high energies. These Bremsstrahlung photons are also of high energy and go on to produce their own $e^{\pm}$ pairs. This process continues resulting in a cascade of particles and photons, often referred to as a particle *shower* or *cascade*. As the $e^{\pm}$ continue to lose energy, eventually ionization becomes the dominant form of energy loss. The cascade will gradually cease as the generated photons no longer carry sufficient energy to generate additional $e^{\pm}$ pairs.

The pair produced e$^{\pm}$ particles are actually generated with a significant amount of kinetic energy, approximately half the energy of the initiating photon. For gamma-rays with energies observable by VERITAS ($E \gtrsim$100 GeV), this translates into a particle speed greater than the phase velocity of light through the atmosphere. The result of such a high velocity particle traveling through the atmosphere (which is essentially a dielectric material) is to produce Cherenkov radiation. A simple Huygens construct (see Fig. 3.1) can be used to show that this radiation is emitted at a characteristic angle given by Eq. 3.2.

$$\theta = arccos\left(\frac{1}{\beta n}\right) \tag{3.2}$$

Here, β is the velocity of the particle divided by the speed of light ($v_{particle}/c$) and n is the index of refraction of the atmosphere. θ is typically $\lesssim 1^{\circ}$ for electrons in the atmosphere. As more and more particles are produced, this radiation builds up, forming a narrow wavefront of Cherenkov emission approximately 1-3 meters thick contained mostly within a distance of $\sim$125 meters of the shower core once it reaches the ground[3] (Hillas, 1982). This Cherenkov

[3]The lateral distribution of these photons somewhat depends on the emission hight of the air-shower.

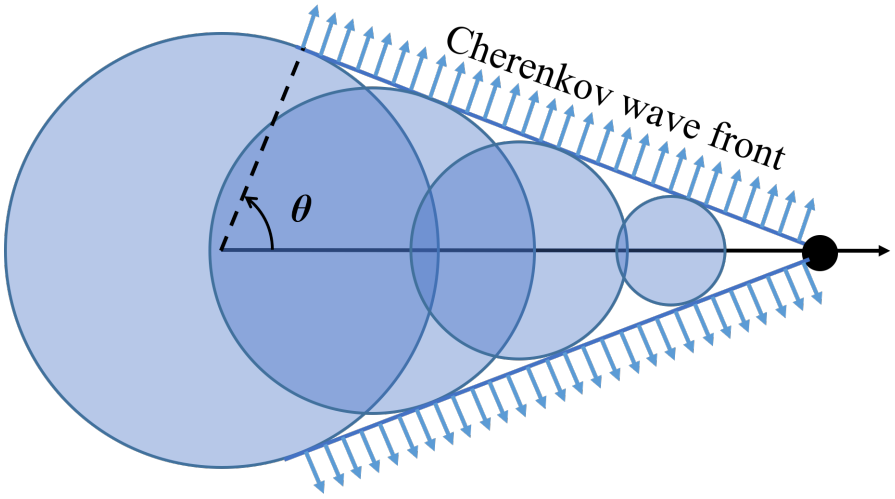

Figure 3.1: Huygens construct of a highly energetic particle and its Cherenkov emission.

radiation is what is observed by the VERITAS instrument. A diagram of this process is shown in Figure 3.2

3.1.2 Cosmic-ray Induced Air-showers

It is important to note that although the VERITAS instrument is intended to detect air-showers initiated by gamma-rays, fewer than 1% of the total air-showers observed are actually initiated by photons. The vast majority of detected air-showers are actually produced by high energy atomic nuclei (hereafter referred to as *cosmic-rays*). When a high energy cosmic-ray enters the atmosphere, it will most likely collide with ambient atomic nuclei creating a cascade of particles through the chain of reactions given in Eq. 3.3.

$$\begin{aligned} p + p &\rightarrow N + N + n_1\pi^{\pm} + n_2\pi^0 \\ \pi^0 &\rightarrow 2\gamma \\ \pi^{\pm} &\rightarrow \mu^{\pm} + \overset{(-)}{\nu}_{\mu} \\ \mu^{\pm} &\rightarrow e^{\pm} + \overset{(-)}{\nu}_{\mu} + \overset{(-)}{\nu}_{e} \end{aligned} \tag{3.3}$$

In the above chain N denotes secondary nucleons produced in the reaction, and $n_{1,2}$ denote the number of $\pi^{\pm,0}$ respectively produced in the interaction. Note that among the products of this interaction will be numerous photons (via π^0 decay) and $e^{\pm}$ (via $\pi^{\pm}$ decay). These particles will produce Cherenkov radiation as well. However, because of the larger transverse

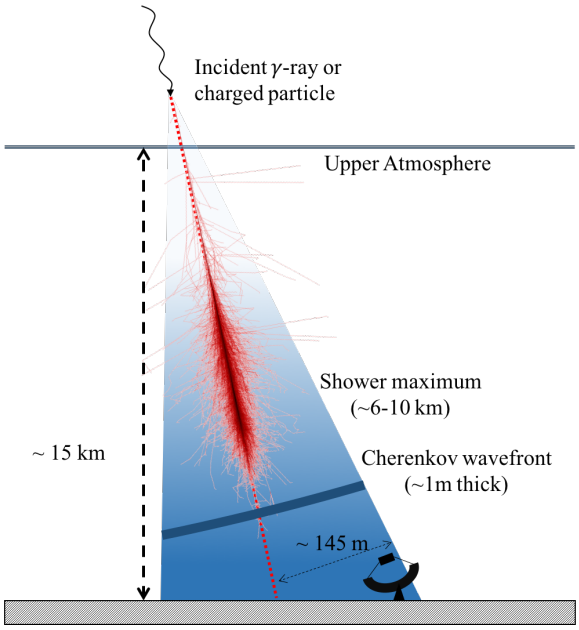

Figure 3.2: Diagram of a typical gamma-ray shower and resulting Cherenkov radiation.

momentum of the pions in the initial reaction, these cosmic-ray showers are typically much broader than gamma-ray showers of similar energy (see for example Figure 3.3). As will be discussed in §4.2.1, this difference in shower broadness is a crucial property in distinguishing between gamma-ray and cosmic-ray initiated showers.

3.2 The VERITAS Instrument

VERITAS consists of an array of four 12-meter imaging atmospheric Cherenkov telescopes (IACTs) located at the Fred Lawrence Whipple Observatory (FLWO) in southern Arizona (31°40' N, 110°57' W, 1.3km a.s.l.). The observatory is not operated during the day time or during periods of exceptionally bright moonlight. This is done in order to protect the photomultiplier tubes in the camera. This section describes the hardware used in each telescope in the array and how the data acquisition system is setup to reduce the frequency of accidentally storing data which does not correspond to air-shower events.

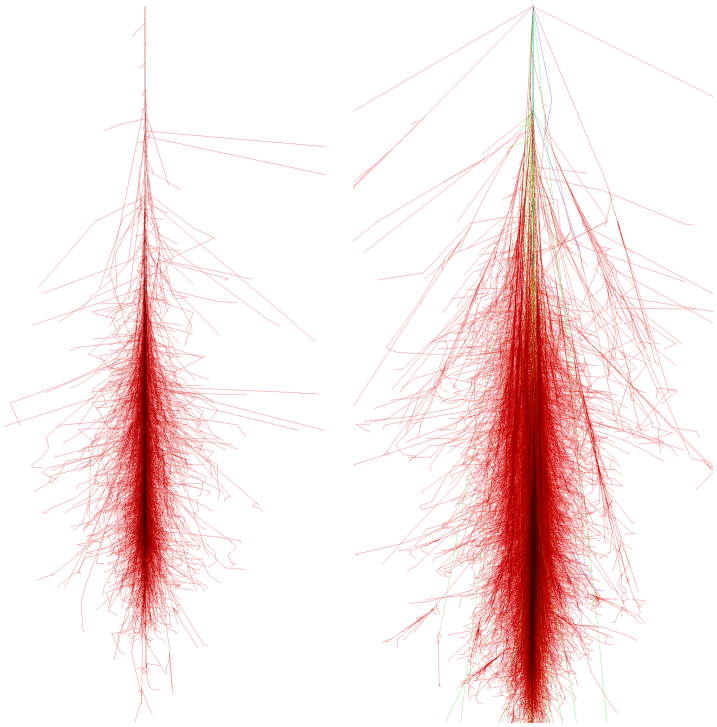

(a) Gamma-ray Shower (b) Proton Shower

Figure 3.3: Comparison of particle distribution in a gamma-ray induced shower (a) and proton shower (b). Both showers were simulated with initial particle energies of 1 TeV using the Cosmic Ray Simulations for Kascade (CORSIKA) simulation package. Images produced by Fabian Schmidt and Johannes Knapp (2005, https://www.ikp.kit.edu/corsika/).

Figure 3.4: Image of the VERITAS array.

3.2.1 Hardware

Each telescope has a 12-meter diameter segmented mirror. The mirrors of each telescope consist of 345 hexagonal facets which have been aluminized and anodized (Roache et al., 2008). The mirrors are responsible for focusing the observed Cherenkov light onto the camera. The optical resolution obtained with these mirrors has an 80% containment radius of $\sim 0.05^{\circ}$(McCann et al., 2010)[4].

The cameras consist of 499 photomultiplier tubes (PMTs). These PMTs operate by converting Cherenkov photons into an electronic current using a photo-cathode to convert the photon signal into an electron (or multiple electrons), a series of dynodes to amplify the electron signal, and an anode to convert the amplified signal into a current.

These resulting PMT signals are then fed into two systems. The first is a constant fraction discriminator (CFD) which decides whether or not the signal is of significance. The CFD will be discussed in more detail in §3.2.2. The second system flash analog-to-digital converter (FADC, Rebillot et al. (2003)). The FADC samples the PMT signal at 2 ns intervals. Each time the signal is sampled, the FADC converts the observed signal into a measure of *digital counts*, where each Cherenkov photon observed by the PMT corresponds to $\sim$5 digital counts. The digitized signals are stored in a 64 μs buffer which allows the array to continue observing at the same time the data acquisition system evaluates the PMT signals to decide whether .

The FADC can only digitize negative signals, truncating positive ones to zero. This is an issue since the night sky background (NSB) produces both positive and negative variations in the PMT response. In order to produce an accurate record of the actual PMT responses and variations, a constant signal is injected into the FADCs. This signal is known as a *pedestal*. In order to monitor the pedestals and subtract them from the PMT signals in the actual analysis, a forced read out of the cameras is made every $\sim$1 sec. This periodic forced read out does not significantly affect the array down time, given that the typical array trigger rate is on the order of a few hundred Hz.

[4]The optical resolution is not to be confused with the gamma-ray point spread function (discussed in §5.2.2.4) which is slightly larger.

3.2.2 Data Acquisition

Because of the setup of the telescope data acquisition system, when the array observes an event it ceases taking data while it reads out the values of the PMTs and writes them to disk. This is referred to as *dead-time*. In order to reduce the fraction of time the array spends writing data a three level *trigger system* is implemented. The trigger system decides when an event has been observed that most likely corresponds to an air-shower event so that the necessary information from each telescope can be saved for later analysis.

The first trigger level determines whether a given PMT has been triggered. In order to determine when this is the case, the VERITAS PMTs use a constant fraction discriminator (CFD, Hall et al. (2003)). In this scheme, each PMT signal is split into two signals, one of which is delayed and inverted while the other is scaled by some fractional value. The two signals are then summed. If the sum of the two signals is above a given threshold, typically around 45-50 mV, then the PMT is identified as having a significant response, and thus considered to have *triggered*.

The NSB also plays a role in the CFD. Fluctuations in PMT signal due the NSB will lead to many L1 triggers which are not initiated by events of interest. The NSB also varies depending on the field observed, increasing for instance in fields along the galactic plane. A rate feedback (RFB) circuit is employed in order to dynamically scale the trigger threshold offset in order to manage the overall trigger rate. It is possible that when a PMT passes the L1 criteria it has observed a gamma-ray event. However, it is also possible that it has only observed a fluctuation in the night sky background, a bright star may have passed over that particular PMT, or some anomaly has triggered only a single PMT.

The second trigger level (L2) determines whether or not an individual telescope has triggered. This is determined by looking for patterns consisting of three nearest neighbor PMTs which have passed the L1 criteria. If such a pattern is found then the telescope is considered to have seen a significant event, and thus the telescope is considered to have *triggered*. While the L2 criteria is useful for discounting single PMT fluctuations, it is still susceptible to cases in which a single telescope may be flashed by some object. Muons developing low in the atmosphere, cars passing near the observing site, observers with flashlights, or even low flying

aircraft are examples of events which could cause a single telescope to pass the L2 criteria.

The third trigger level (L3) determines whether or not the entire array has triggered. To accomplish this, each L2 signal is sent to a central control building. The arrival times for these signals are corrected for the delay introduced by the varying distance from each telescope to the central control building, as well as approximate propagation time of the shower front across the array. The L3 criteria is satisfied when at least two telescopes have passed the L2 criteria within a window of 50 ns, after accounting for these signal delays.

Once the array is considered to have triggered, a 48 ns (24 samples) window containing the detected signal is read from the FADCs and stored regardless of whether an individual PMT or telescope has passed the L1 or L2 criteria for the event. With this trigger system the array achieves a dead-time of <10%. More details regarding the VERITAS array trigger system are provided by Weinstein (2008).

3.3 Hardware Maintenance and Calibration

3.3.1 Mirror Degradation and Alignment

Because the mirrors are left open to the elements, the facets must be periodically washed to remove accumulated dust and grime. Despite periodic washing of the mirrors, the reflectivity of each facet will degrade over time. Because of this, the facets are routinely removed, cleaned, re-anodized and re-aluminized (Roache et al., 2008). Once the facets are placed back on the telescope they must be aligned. This process involves raster scanning around a bright star and monitoring the alignment from individual facets. The end result is a map of the mis-alignment of each facet which is corrected (McCann et al., 2010). This alignment procedure is typically carried out at least twice on consecutive nights to ensure optimal mirror alignment.

3.3.2 CFD Calibration

As was outlined in §3.2.2 each PMT has its signal put through a constant fraction discriminator (CFD) in order to determine whether or not it has triggered above a set threshold. The value of this threshold is important. If set too low the array will trigger near constantly on small fluctuations in the night sky background. If set too high the array will ignore low energy

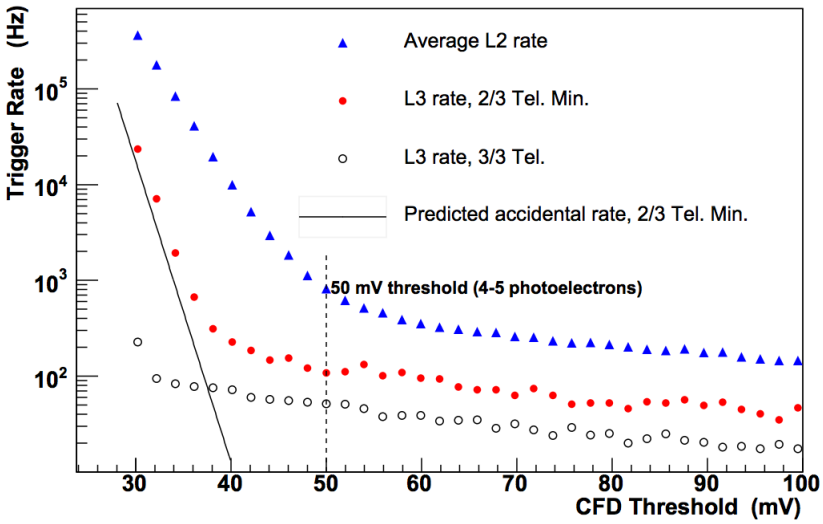

Figure 3.5: Sample bias curve reproduced from Weinstein (2008) based on a three IACT array with a 50 ns coincidence window. Blue triangles represent the averaged L2 trigger rate for the three telescopes, red circles represent the rate of two of the three telescopes triggering within the 50 ns coincidence window, and open circles represent the rate of all three telescopes triggering within the coincidence window. The solid line indicates the predicted accidental trigger rate on random noise based on the L2 trigger rates. The dash line indicates a typical threshold used for observations of 50 mV.

events, which are important for studying certain sources, such as pulsar analyses or sources with very soft spectra.

To determine the correct threshold the following procedure is enacted. First the array is set to observe a patch of sky containing no significant gamma-ray sources and very few bright stars. Next the CFD threshold is varied[5] in order to monitor the triggering rate of the array. This results in a curve which outlines the bias of the instrument towards accidental triggers by fluctuations in the night sky background (see Fig. 3.5 for an example of such a bias curve). The threshold is chosen such that the rate of array level triggers is dominated by actual particle shower events rather than background noise. Typically, this threshold is around 45 - 50 mV.

3.3.3 PMT Gain Calibration

As will be discussed in §4.2, various parameters of an air-shower event are measured based on the signal of the PMTs in each camera. The strength of this signal is directly related to

[5]The CFD thresholds tested typically range from 30 mV - 100 mV.

the ability of a PMT to convert the Cherenkov photon signal to an electron current. This is sometimes referred to as the *gain* of the PMT which can vary between PMTs. Additionally, the gain of a PMT can fluctuate from night to night making it necessary to calibrate this gain.

This calibration is done through the use of a system known as the *flasher* (Hanna et al., 2010). The system works by briefly illuminating the camera with a set of 7 light emitting diodes (LEDs) which emit light at a peak wavelength of approximately 465 nm. The light from the LEDs passes through a diffuser screen which allows the PMTs to be uniformly illuminated. When run, the system flashes the camera at a rate of 200 Hz cycling incrementally through the number of LEDs turned on from none to all. The flasher system is also connected to the array trigger system. This is done to forcibly write out the PMT responses stored in the FADCs for each pulse of the flasher.

3.4 Array Configuration and Instrument Epochs

Since the detector's was fully commissioned, it has gone through various *epochs*, which are sequentially referred to as V4-6. These epochs are identified as follows:

- V4 (*old array*) - Initial running of the observatory with all four telescopes fully commissioned (April 2007 - August 2009)
- V5 (*new array*) - Relocation of the T1 telescope (September 2009 - August 2012)
- V6 (*upgrade array*) - Upgrade of the PMTs used in the VERITAS cameras (September 2012 - present)

The epoch definitions are motivated by changes to the array configuration. The V4 epoch of the array identifies the initial period during which all four telescopes were in operation. However, during this time T1 and T4 were in very close proximity, lowering the sensitivity of the instrument[6]. The V5 epoch began in the summer of 2009 after the relocation of the T1 telescope ∼200 meters east to a more optimal location in reference to the other telescopes in the array (see Fig. 3.6). This move reduced the number of false detections due to local muons and increased the effective area of the instrument. Perkins et al. (2009) notes an increase in

[6]It should be noted that despite the lower sensitivity, the array still met all of its design and sensitivity goals.

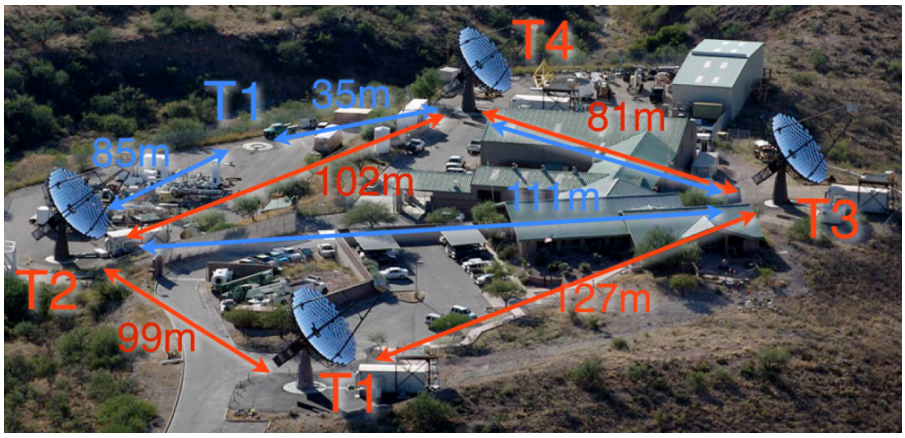

Figure 3.6: Distances between individual telescopes of the VERITAS array. Blue lines identify distances between telescopes in the V4 epoch. Red lines identify distances in the V5 and V6 epochs.

sensitivity of ∼30% to the integral flux of the instrument above 300 GeV after the T1 move. The transition to the V6 epoch occurred in the summer of 2012 when the PMTs in each telescope camera were replaced with higher quantum efficiency PMTs. The new PMTs had an improved photon detection efficiency of ∼50% resulting in a decrease in the lower energy threshold of the detector by ∼30% (Kieda, 2013).

Every year there is an approximately 1-2 month time period during the summer when the array is not operated. This gap corresponds to the annual monsoons experienced at the VERITAS observing site. This time is typically used to perform large scale maintenance and improvements to the telescopes. Both the relocation of the T1 telescope in 2009 and the camera PMT upgrade in 2012 were done during this period.

CHAPTER 4. VERITAS DATA ANALYSIS

This chapter provides an overview of the standard methods of analyzing data from imaging atmospheric Cherenkov telescope (IACT) arrays. It details how the data is processed, how parameters of the shower initiating particle are estimated, and concludes with a description of the typical methods for source detection. In VERITAS the standard software packages used for analyzing data are the VERITAS Gamma-ray Analysis Suite (VEGAS) or Eventdisplay (Cogan, 2008). For the work presented here, only VEGAS is used, and thus the details of this chapter will focus on that package.

4.1 Preliminary Data Reduction

Before the data is analyzed, it must first pass preliminary selection criteria. Typically, data is not used when a significant anti-correlation between the array level trigger rate and the sky temperature[1] is observed. An example where the sky conditions have noticeably affected the data quality of a 20 minute data run is presented in Figure 4.1. The dominant cause of these fluctuations is cloud cover, however cars driving near the observatory, airplanes, satellites, and even observers walking around the site can potentially cause brief interruptions in the data.

Data which passes the above criteria is then calibrated using a flasher run taken under similar conditions and during the same night as the data. The flasher is described in §3.3.3.

4.2 Event Reconstruction

The VERITAS array operates in stereo mode. This means that when a gamma-ray induces an air shower in the atmosphere, all four telescopes have the potential to observe it. The

[1] The sky temperature is measured using an infrared pyrometer.

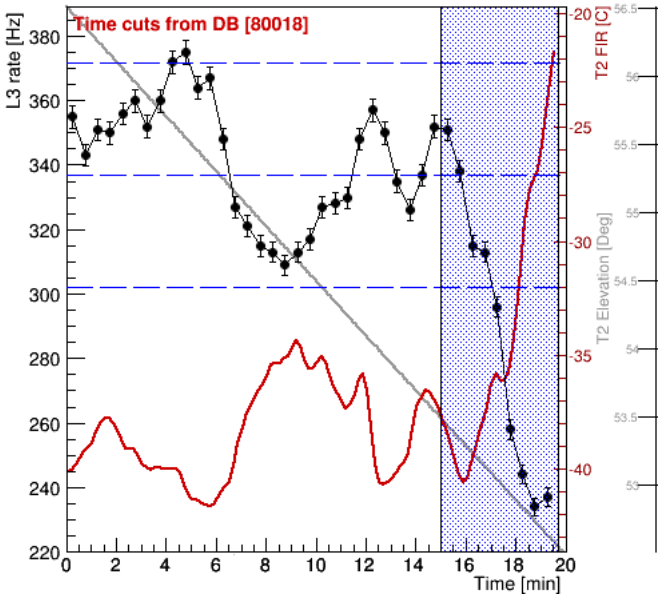

Figure 4.1: The above demonstrates a run in which the sky conditions have impacted the data. Black points indicate the array trigger rate (Hz) and the red curve indicates the temperature (°C) of the atmosphere as measured by an infrared pyrometer attached to the T2 telescope. The blue dashed lines indicate a measure of the spread in the array trigger rates. The shaded region from 15-20 minutes is a suggested time cut region computed by the software used to monitor data quality. However, the large degree of anti-correlation throughout the data run suggests the entire run is affected and thus should not be used.

information from each telescope that successfully observes the air-shower is combined to obtain estimates of various parameters of the shower, and thus of the gamma-ray which initiated it.

4.2.1 Image Parameterization & High Level Data Reduction

An image of the airshower in each telescope camera is constructed from the integrated FADC traces over a 7 sample window in each PMT. The camera images then go through a *cleaning* process in which each integrated PMT trace is divided by the standard deviation of the pedestal values (pedvar). The pedvar is determined by evaluating the stored pedestal events described in §3.2.1. The divided traces represent the relative significance of the PMT signal relative to the background NSB signal level. Each pixel is then placed in one of three categories:

- Image pixel - Significance $> 5\sigma$
- Border pixel - Significance $> 2.5\sigma$
- Noise pixel - Significance $< 2.5\sigma$

All image pixels are retained as well as all border pixels neighboring image pixels. The rest of the pixel values are removed are removed from the image.

The resulting cleaned image from each telescope which contributes to a given event detection is parameterized according to the prescription outlined by Hillas (1985). The image in each camera is characterized by a number of different parameters including the following:

- **Width** - The r.m.s. spread of light perpendicular to the shower axis.
- **Length** - The r.m.s. spread of light along the shower axis.
- **Distance** - Distance of the image centroid from the camera center.
- **Size** - Summed digital counts in the image.

These parameters are represented in Figure 4.2.

From this point, several combined parameters are computed. This includes a mean scaled width (MSW) and mean scaled length (MSL) parameter calculated according to Daniel (2008)[2].

$$MSP = \left(\frac{1}{n}\right) \sum_{i=0}^{n} \frac{p_{i,j}}{< p_i >_j} \tag{4.1}$$

[2]A slight modification is made to the Daniel (2008) formula in that the parameters are estimated on a per-telescope basis. For instance, the width in a given telescope is scaled by the expected width from simulations of that specific telescope.

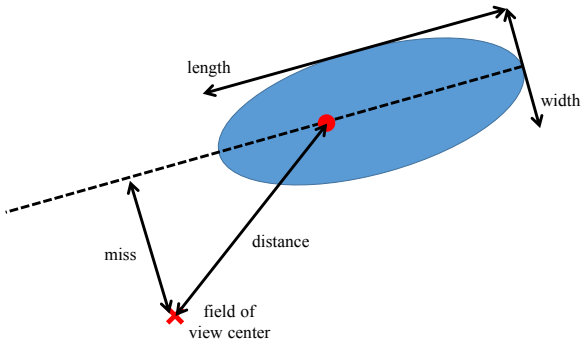

Figure 4.2: Diagram showing the parameterization of a typical telescope image. The red circle represents the image centroid. The red x represents the center of the cameras field of view.

Here, p represents the parameter being estimated (either width or length), n is the number of telescopes participating in the event reconstruction, i indexes the telescope for which the parameter is being estimated, and j indexes the possible combinations of shower parameters over which the expected width or length value is characterized (e.g. size, impact distance, and zenith angle).

Because the expected parameter values are generated from simulations of gamma-ray air-showers, it can be seen from Eq. 4.1 that the resulting mean scaled parameters should peak very close to one for gamma-ray events in data. On the other hand, since cosmic-ray showers typically have much broader particle distributions, the associated mean scaled parameters will peak above one (see for example Figure 4.3). By exploiting this difference, the number of background comic-ray events can be dramatically reduced while preserving the bulk of the gamma-ray photon events.

There is a notable group of events in the cosmic-ray distribution of MSW that peaks near one at lower energies. This peak is most likely due to low energy cosmic-rays in the atmosphere that produce fewer π^0 which decay into gamma-rays and produce Cherenkov radiation. The fewer π^0 results in a more compact image, and thus a more gamma-ray like image.

4.2.2 Position and Energy Reconstruction

Once an observed air-shower has been observed and the associated Hillas parameters determined, it is possible to combine the images in such a way to reconstruct the origin of the

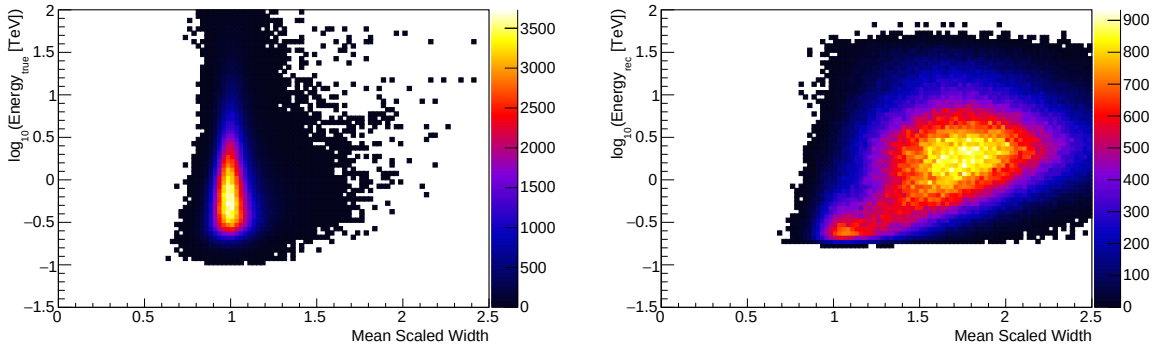

(a) Gamma-ray MSW Distribution

(b) Background MSW Distribution

Figure 4.3: MSW distributions derived (a) from simulated γ-ray air-showers and (b) from observations excluding events within 0.4° of any known sources. Distributions are shown as a function of logarithmic energy. The color scale represents the number of events used to generate the distribution. Models are extracted for an observation position of 70° elevation, 180° azimuth, and 0.5° offset with four telescopes participating in the shower reconstruction.

initiating particle on the sky (Kohnle et al., 1996). Fig. 4.4a diagrams a typical setup for a shower observed with two telescopes in the VERITAS array. Here, the incident direction is offset from the telescope pointing direction by an angle θ_x. Similarly another angle can be constructed, θ_y, in the perpendicular direction. In this case, the major axes of the parameterized images can be projected in the plane of the cameras where they will intersect at the point ($-f\theta_x$,$-f\theta_y$). Here f is the telescope focal length and the negatives account for the reflections due to the telescope mirrors. The array tracking position corresponds to the center of the field of the camera reference frame. As such, the incident position of the event can be determined.

In reality, there will be some uncertainty in the observed shower images resulting in a slight discrepancy in the reconstructed position and the true position of the image position. It can be seen in the two telescope example above that when the major axes are approximately collinear any slight uncertainty in the parameterization of the images translates into a large uncertainty in the position reconstruction. Having more than two telescopes in the reconstruction is therefore a benefit in reducing the error on the reconstructed position. However, having multiple telescopes in the position reconstruction provides an additional challenge as the same uncertainties will almost ensure that the three major axes do not cross at the same point (yellow x's in Fig. 4.4c). In this case the true position is determined often through some weighted

average[3] of the three intersection positions.

The energy of the event is determined through the use of many simulated gamma-ray air-showers. The simulations are generated so that they cover a broad range of sky positions (zenith and azimuth angles), telescope offsets, and energies. The simulated air-showers are also generated such that they impact the ground over a large range of distances from the telescope, typically 750-1000 meters from the center of the array. These simulations are then processed through the standard image analysis algorithm where several reconstructed parameters related to the shower are stored, such as impact distance, which telescope has observed them, size in the camera, and the computed Hillas parameters. The various different combinations of these parameters are stored in a table so that when an observed air-shower is processed the best estimate of the incident particles true energy can be referenced from the stored table.

When simulating a gamma-ray of a specific energy and its air-shower, the resulting observed parameters will vary from simulated shower to simulated shower. For instance, two showers initiated by gamma-rays of the same energy, but whos showers begin developing at different altitudes will have different observed parameters. Notably, the shower developing high in the atmosphere will result in less light observed in the images of the telescopes. The resulting energy lookup table will have some level of uncertainty associated with the estimate of the true energy. As mentioned previously, this uncertainty in the estimate of the true energy is typically on the order of 15%-20% for VERITAS (Park and VERITAS Collaboration, 2015).

4.3 Background Estimation

When analyzing VERITAS data it is necessary to estimate the level of background contaminating the region around the source of interest. Typical methods used are the ring background and reflected region methods. However, as will be outlined in §4.3.3, these methods are ill-suited to studying sources with very high angular extent, such as the extended emission around the Geminga pulsar and the Cygnus Cocoon. For these sources it is necessary to implement a new analysis. Such a technique will be discussed in the following chapter.

Because the gamma-ray signal typically lies on top of some background flux, there is a need

[3]The positions are weighted by the uncertainty of each image. The uncertainty generally scales with the image size, where larger image sizes have a lower uncertainty.

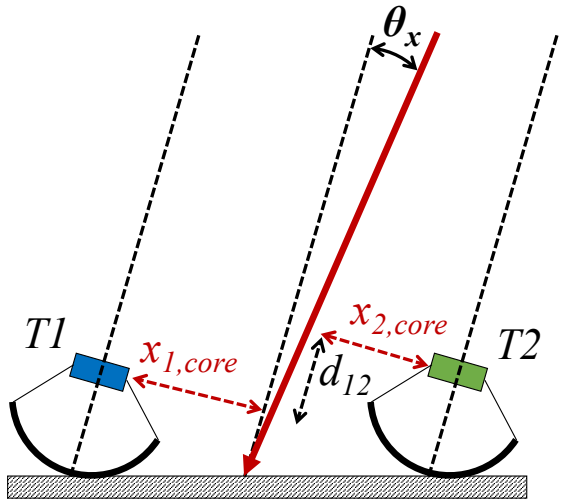

(a) Telescope and shower geometry

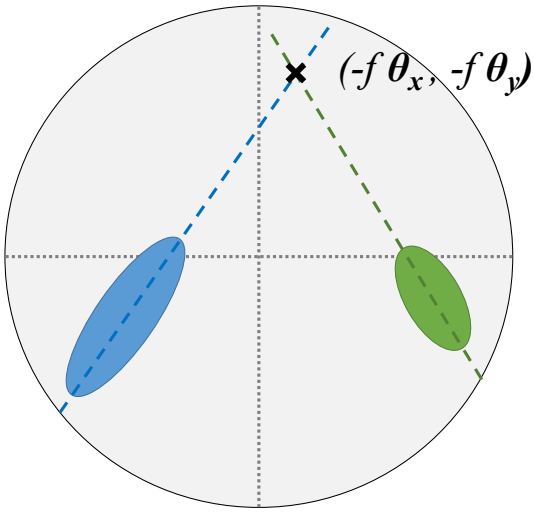

(b) Sky position reconstruction

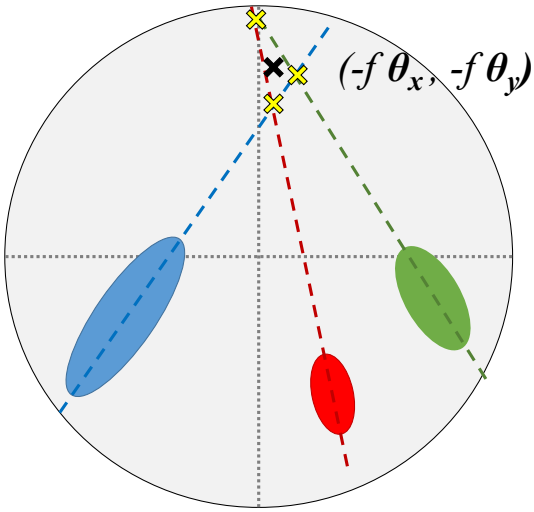

(c) Sky position reconstruction

Figure 4.4: (*a*) Diagram of the geometry between the individual telescope pointings (black dashed lines) and the incident shower direction (red line). (*b*) Image showing how the position (black x) is reconstructed from the parameterized telescope ellipses in the reference frame of the cameras. (*c*) Position reconstruction from a shower imaged by three telescopes, providing a more accurate determination of the position, x.

to account for both components of emission in any region where a source is expected. The total emission in the vicinity of the source is estimated by integrating all events within some distance of the source position. This region is referred to as the ON region. The level of background flux in the On region is estimated by summing all of the counts in a region (or regions) in the field of view which are expected to contain no gamma-ray emission. This region (or collection of regions) is referred to as the OFF region. Li and Ma (1983) Eq. 17 is typically used to estimate the significance of the counts in the ON region as compared to the prediction of counts from the OFF region.

$$\sigma = \sqrt{2}\left[N_{ON}\ln\left(\frac{1+\alpha}{\alpha}\left[\frac{N_{ON}}{N_{ON}+N_{OFF}}\right]\right) + N_{OFF}\ln\left((1+\alpha)\left[\frac{N_{OFF}}{N_{ON}+N_{OFF}}\right]\right)\right]^{1/2} \quad (4.2)$$

The sigma calculated from this distribution corresponds into a probability that the observed number of events in the ON region is a random fluctuation in the background. Assuming a sufficiently large number of counts in the ON region, the probability is assumed normally distributed and the sigma can be translated into an appropriate probability according to the upper-tailed probability given by Eq. 4.3.

$$prob = \frac{\int_{\sigma}^{\infty} e^{-x^2/2\sigma}dx}{\int_{-\infty}^{\infty} e^{-x^2/2\sigma}dx} \quad (4.3)$$

The associated probabilities for a few chosen values of sigma are listed in Table 4.1. A threshold of $\sigma > 5$ is typically used to establish the firm detection of significant emission from an object. There is a simple argument to support requiring 5σ by considering the number of bins in a sky map. Assuming a circular field of view of radius 1.75° broken into bins of 0.025°×0.025° yields ∼15,400 bins. This suggests that a 4σ bin should occur in half of all analyses even when no source is present. However, a bin with 5σ would only occur in 1 of every 225 analyses. The two methods for estimating N_{OFF} are discussed in the next two sections.

4.3.1 Reflected Region Model

The reflected region model estimates the level of background by using a set of n_{OFF} OFF regions. These OFF regions are chosen to mimic the ON region, in that they are the same size and offset the same distance from the center of the field of view (see Fig. 4.5, right). A small buffer around the ON region is used to prevent contamination from mis-reconstructed

Table 4.1: Probability of obtaining a σ value from Eq. 4.2.

σ	probability	1 in X chance
1.0	0.159	6
2.0	0.0228	44
3.0	0.00135	741
4.0	3.17×10^{-5}	31,574
5.0	2.87×10^{-7}	3,488,556

source photons. The main benefit of this method is that it does not require accounting for the radial acceptance of the instrument[4]. The reflected region model is typically used for spectral analyses for this reason. However, this method cannot be used to analyze regions near the center of the field.

4.3.2 Ring Background Model

The ring background model (RBM) uses an annulus around the ON region to estimate the background flux in the source region (see Fig. 4.5, left). This annulus is chosen such that the ratio of on source area (Ω_{ON}) to the annulus area (Ω_{OFF}) is approximately 1:7. The main drawback of this method compared to the reflected region model is that since the OFF region covers a broader range of camera positions at offsets different than the ON region, the acceptance can no longer be assumed similar. However, the advantage of the RBM is that now the size of any detectable gamma-ray component can now be determined at all positions in the field of view including near the center.

4.3.3 Standard Analysis of Highly Extended Sources

The reflected region and ring background models work well for detecting and characterizating sources $\lesssim$0.3° in radius. However, as the source extension increases these techniques begin to struggle. For example, consider a source with a radius of 0.5°. Using the typical observing offset of 0.5° it is easy to see that the reflected region results in only one possible region for characterizing the background. As the source extension becomes larger, the reflected

[4]There may still need to be corrections applied due to changes in airmass which can affect detected counts at different zenith angles across the camera.

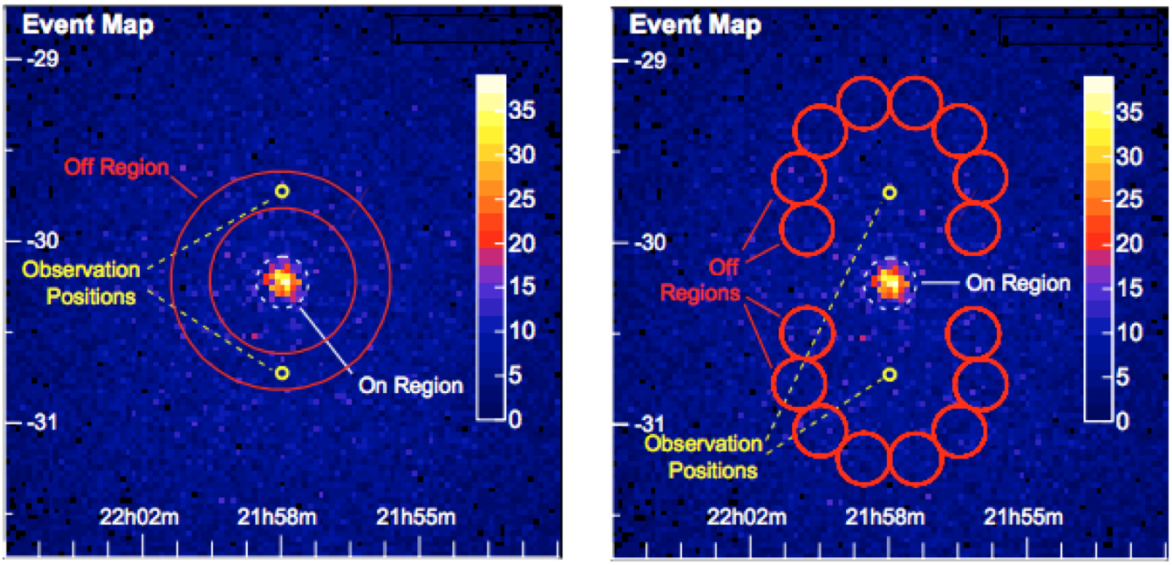

Figure 4.5: Example showing the ON and OFF regions for the ring background model (*left*) and reflected region model (*right*). Image from Berge et al. (2007).

region becomes impossible without increasing the offset of the observations. The upper limit of sources that can be observed with the reflected region method is thus determined by the radial extent of the detector's field of view. For VERITAS, this corresponds to a limit of $\sim 0.8^\circ$ radius. However, with only one OFF region from which to estimate the background, the resulting estimate of the source flux will have a large uncertainty and it is unlikely any meaningful constraints could be obtained.

The RBM method does not require such dedicated, equally sized regions. However, as the source becomes comparable in size to the field of view, the annulus used to estimate the background must shrink in order to stay within the bounds of the instrument. As the annulus shrinks, the error on the estimate of the background flux increases and the analysis again suffers from a lack of suitable OFF regions in the camera.

The above discussion glosses over one important detail for using the reflected region and ring background models. Rarely is it known exactly where the emission is coming from in the field of view for the largest sources of interest ($\gtrsim 2^\circ$ across). Without fore knowledge of the source morphology the above techniques will inevitably result in unknowingly using regions containing source emission in our background estimation leading to self-subtraction of the source. The

only way around this is to exclude a region of the field sufficiently large to cover any potential region of emission.

One approach developed in the past is known as the *matched runs* method which uses data from other fields (OFF data) to estimate the background in the data taken on the source of interest (ON data). Flinders and for the VERITAS collaboration (2015) presents an updated version of this technique specifically for VERITAS data. The OFF data is chosen to match the observing altitude, azimuth, and night sky conditions of the ON data, hence this technique is called the *matched runs* method. Previous implementations of a matched runs method have struggled to correctly account for slight differences in the background flux rate between the ON runs and OFF runs. Flinders and for the VERITAS collaboration attempts to account for this by finding two OFF data samples, one that underestimates the background flux, and one that overestimates the background flux. The level of background flux is evaluated by looking in a region of MSW above 1.2, a region with little to no gamma-ray events and dominated by the background flux. A *blended* OFF run is generated by combining and averaging these two runs such that the flux of the blended OFF data is a match to the ON data. The data can then be analyzed in the gamma-ray dominated region of MSW using the standard analysis. Any sources that may appear in the OFF data are excluded from background estimation. Unless multiple blended OFF data samples are produced for each ON data sample, this technique will still suffer from a poorly constrained estimation of the background when analyzing a highly extended source.

Another technique known as the *maximum likelihood* method has also been developed to address the analysis of extended sources. The implementation of this technique for VERITAS data is known as the 3D maximum likelihood method and is the focus of this dissertation. Details about this methods implementation are provided in the next chapter.

4.3.4 2FHL J0431.2+5553e: A Test Case

One source that demonstrates the limitations of the RBM technique is a source from the second *Fermi*-LAT Catalog of hard sources (2FHL), 2FHL J0431.2+5553e (Ackermann et al., 2016). This source was characterized in the *Fermi*-LAT data as a uniform disk with radius

$1.27° \pm 0.04°$.

VERITAS has taken approximately 22.5 hours of good quality data on or near this source. A standard RBM analysis was carried out on this data using a source integration area of ∼0.16 square degrees[5]. The background for each bin was determined from an annulus of r_{inner}=1.3°, r_{outer}=1.5° centered at the respective bin. The region around the source was excluded from use in the background estimation via a 1.3° radius exclusion region. Since this exclusion region cuts out a majority of the observing field, the background is instead parameterized from a sample of data taken on another source which tracks a similar path through the observed sky. Using the standard RBM analysis reveals a peak significance of 3.86σ at a position approximately 2.42° away from the center of the assumed source emission. This significance is below the accepted threshold for a significant detection. In addition, the position is well outside the published source position, even after taking into consideration the reported extension of the source. Therefore, currently VERITAS is unable to claim a detection of the source with the standard RBM analysis.

Part of the techniques limitation results from the need to use an integration region $< 0.25°$ in radius. The ratio of Ω_{OFF}:Ω_{ON} must remain sufficiently high to reasonably constrain the estimate of the background flux. The analysis described above, however, results in $\Omega_{ON} \approx 3\%$ of the total area covered by the source. This implies the RBM analysis is only sensitive to the flux from small portions of the source. It also implies that the spectrum cannot be determined across the entire source in a single analysis.

[5]This corresponds to an integration region with radius ∼0.224°.

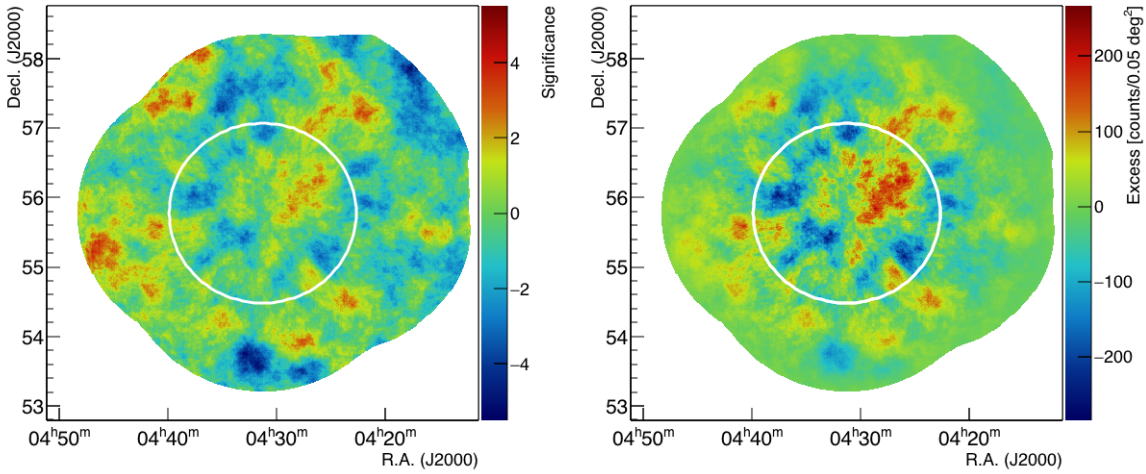

(a) Significance Map

(b) Excess Map

Figure 4.6: Results of a standard RBM analysis of the 2FHL J0431.2+555e source in ∼22.5 hours of VERITAS data. The white circle represents the source region excluded from background estimation. The significance map (*left*) shows that the region covered by the source does not contain any point region of significant emission. The Excess map (*right*), though showing a region of higher excess within the exclusion region, it also shows regions of similar amplitude, yet negative, suggesting the large excess is not the result of a significant source.

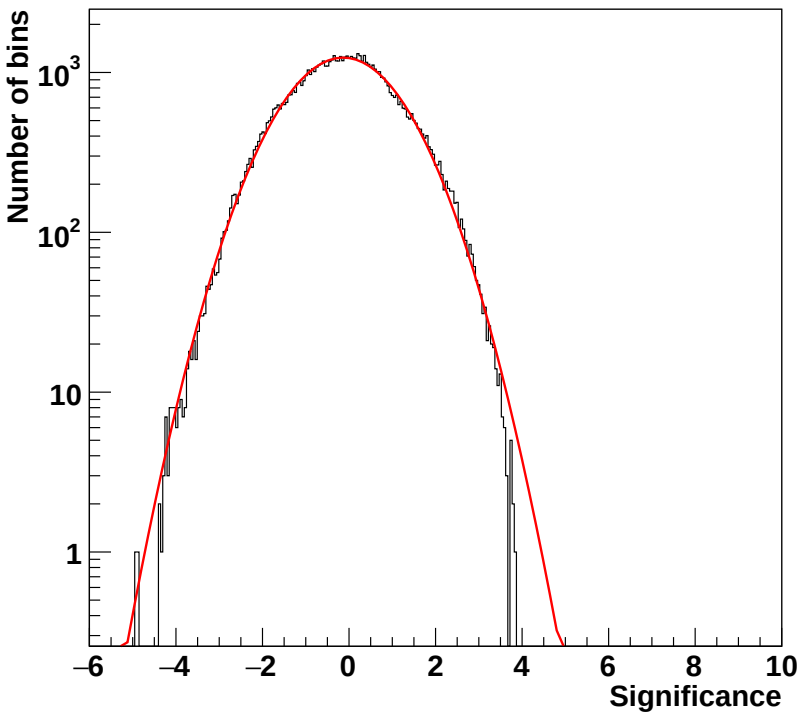

Figure 4.7: Distribution of bin values in significance map shown in Fig. 4.6a.

CHAPTER 5. MAXIMUM LIKELIHOOD METHOD

Various high energy instruments including EGRET, *Fermi*-LAT, HAWC, and CTA have employed a maximum likelihood technique in their own data analysis (Mattox et al., 1996; Abdo et al., 2009a; Younk et al., 2015; Knödlseder et al., 2016). This chapter provides an overview of this technique and describes the maximum likelihood approach developed to analyzing data from the VERITAS observatory.

5.1 Method of Maximum Likelihood

5.1.1 Overview

The maximum likelihood method (MLM) is an approach which seeks to model the expected distribution of data over a set of observables ($\vec{\theta}$). This model is typically represented as a probability density function (PDF). Once the model has been constructed, a likelihood value (L) can be computed by taking the product of the the PDF evaluated for each data point.

$$L(\vec{\boldsymbol{s}}) = \prod_{i=1}^{d} p(\vec{\boldsymbol{\theta}}_i|\vec{\boldsymbol{s}}) \tag{5.1}$$

It can be seen that a model which more accurately represents the data will have a larger likelihood value than one which less accurately represents the data. The above model is represented as a function of some unknown variables $\vec{\boldsymbol{s}}$. The most likely value of those variables can be found by searching for the values which maximize L. Hence the name, *maximum likelihood method*.

The computed value of L is somewhat arbitrary. L can be increased by simply using a more complicated model with additional free parameters. For example, a model that is the sum of two Gaussians as opposed to a single Gaussian. In order to make this a useful tool there must

be a way of establishing whether the more complicated model is preferred over the simpler model. This is where Wilks' Theorem becomes useful.

5.1.2 Wilks' Theorem

Wilks (1938) states that when the parameters being estimated are normally distributed in large samples, then a test statistic can be computed according to

$$TS = -2 \ln \left(\frac{L_{null}}{L_{test}} \right) \tag{5.2}$$

Here, L_{null} represents the likelihood of a specific model, assumed to be the null hypothesis model. L_{test} represents the likelihood based on a test model which is able to reduce back to the null model for certain values of the fit parameters $\vec{s}$. Such a model is referred to as a *nested* model. Wilks goes on to point out that the test statistic (TS) follows a chi-squared distribution with degrees of freedom (n.d.f.) equal to the number of added free parameters in the test model compared to the null model.

Coming back to the example of fitting the distribution of some data sample with a single Gaussian (null model) versus a double Gaussian (test model), Wilks' Theorem can now be employed to evaluate whether the more complicated model is preferred. Taking the position of the Gaussians as being fixed, the test model introduces two additional free parameters to be fit. These are the width of the second Gaussian and the relative strengths between the two Gaussians. The computed TS will now be distributed according to a chi-squared distribution with two degrees of freedom. That is, if this experiment is repeated an infinite number of times on data samples derived from the single Gaussian model, the resulting distribution of TS values would follow Eq. 5.3.

$$f(TS) \propto e^{-TS/2} \tag{5.3}$$

The significance can now be computed as (Mattox et al., 1996)

$$S = \int_{TS}^{\infty} x_2^2(\zeta) d\zeta \tag{5.4}$$

where x is the chi-squared distribution with two degrees of freedom and ζ is the TS value[1].

[1] In most analyses of high energy data, an additional factor of 1/2 is included in the integral to account for the fact that negative source fluxes are not allowed, but the background will still have positive and negative fluctuations. Thus half the TS values will pile up at zero.

In the case of only one additional degree of freedom in the test model, the significance formula follows a normal distribution and the null model can be rejected in favor of the test model at the $\sqrt{TS}$ significance level. It should be pointed out that in practice the distribution is rarely ever *exactly* chi-squared distributed. Rather, in order to establish the true relationship between TS and significance a large number of simulated datasets (derived from the null hypothesis model) needs to be fit with both models and the true distribution of TS values derived.

5.2 3D Maximum Likelihood

The technique implemented in order to study extended emission in VERITAS data is termed the *3D maximum likelihood method* (3D MLM). The method seeks to model the expected distribution of VERITAS data in two spatial dimensions which are analogous to celestial coordinates (right ascension and declination) on the sky. Additionally, the data is also modeled in a third dimension based on mean scaled width[2], a known gamma/hadron discrimination parameter (Hillas, 1985), specifically in order to improve sensitivity to sources greater than ∼0.5°in diameter).

5.2.1 Generating Signal Spatial Models

In order to produce a γ-ray source spatial model the formulation from Mattox et al. (1996) Eq. 2 is used.

$$S_{src}(\vec{\boldsymbol{r}}|\vec{\boldsymbol{s}}) = \frac{1}{N}\int_{E_{min}}^{E_{max}}\int_{0}^{\infty}[B(\vec{\boldsymbol{r}},E')*P(\vec{\boldsymbol{r}},E')]S(E'|\vec{\boldsymbol{s}})R(\vec{\boldsymbol{r}},E',E)A(\vec{\boldsymbol{r}},E')dE'dE \qquad (5.5)$$

This gives the expected spatial distribution of the source emission as it is observed. B represents the intrinsic source morphology, which in the case of a point source is a delta function centered at the source position. Other terms are meant to account for various instrument response functions (IRFs). These include the point spread function (PSF, P), energy resolution (R), and effective area (A). Additional parameters are the intrinsic source energy spectrum (S), the spatial coordinates in the field of view ($\vec{\boldsymbol{r}}$), the true γ-ray energy (E'), and the reconstructed γ-ray energy (E).

[2]For a description of mean scaled width refer to §4.2.1.

5.2.2 Deriving Instrument Response Functions

In order to accurately model data taken by the VERITAS instrument, it is necessary to account for the response of the instrument. Specifically, the responses that need to be characterized include the effective collection area of the instrument (effective area, §5.2.2.2), the probability of mis-estimating the photon energy (energy resolution, §5.2.2.3), the instrument gamma-ray spatial resolution (PSF, §5.2.2.4)[3], and the distribution of photons in our gamma/hadron discrimination parameter (mean scaled width, §5.2.2.5).

5.2.2.1 Description of Simulations Used

To ensure the models produced are accurate each of the following IRFs must be determined for the full set of observing conditions over which the data was taken. This includes observing position on the sky (zenith and azimuth angles), atmospheric conditions, configuration of the telescope array, and background noise level. This is achieved through the use of a sample of simulated gamma-ray air-showers. This also allows an appropriate level of events to be generated from which accurate values for the parameterized IRFs can be extracted. The simulations are generated for the following values of observable parameters

- **Epoch** - Covers array configuration V5 (see §3.4)
- **Season** - One atmospheric model is used which describes the transmission of the atmosphere winter months (November - April)
- **Telescope Multiplicity** - The number of telescopes participating in the reconstruction (three or four, events with only two telescopes were ignored)
- **Zenith Angle** - 0°, 20°, 30°, 35°, 40°, 45°
- **Azimuth** - 0°, 45°, 90°, 135°, 180°, 225°, 270°, 315°, 360°

These simulations are generated via a Monte Carlo technique[4]. These simulated air-shower

[3]The gamma-ray PSF discussed here is not be confused with the optical PSF of the individual telescopes as discussed in §3.2.1.

[4]Air-showers were generated using the CORSIKA package (Heck et al., 1998) with the detector simulated using the GrISUDet software package.

events are then processed using a set of cuts chosen to optimize the instruments response to gamma-ray events while minimizing its response to background.

5.2.2.2 Effective Area

The *effective area* of the VERITAS instrument is a measurement of the effective collection area over which the instrument can observe gamma-ray air-showers. The effective area is calculated as the true area over which the simulated air-showers were generated (A_{thrown}) multiplied by the ratio of the number of events passing cuts ($N_{observed}$) to the total number of events simulated ($N_{simulated}$).

$$A = A_{thrown} \frac{N_{observed}}{N_{simulated}} \tag{5.6}$$

Air-showers are typically generated over an area of radius 750-1000 meters centered on the array. This translates into A_{thrown} ≈1.77-3.14 km^2 and A is on the order of ∼10^5 m^2. It is important to note that A is a function of the true energy of the simulated photons and does not take into consideration the probability of mis-reconstructing the energy of a given photon.

Sample distributions of the effective areas are displayed for 0°, 20°, and 40° zenith angles in Fig. 5.1. These distributions highlight two changes in the effective area when observing an air-shower at larger zenith angles. The first is that the effective area at lower energies *decreases* at higher zenith angles. The second is that the effective area for larger zenith angles *increases* at higher zenith angles. Both of these effects are caused by an increase in airmass and atmospheric depth at larger zenith angles. As showers at larger zeniths pass through the atmosphere the light produced by the shower will be absorbed to a greater degree. For lower energy showers, the light is absorbed to the point where the shower is no longer detectable. Larger energy showers produce enough light to still be observed, but the larger distance the light must travel through the atmosphere yields a larger light pool at the detector. This increases the area over which the array is capable of detecting the shower yielding a large effective area.

5.2.2.3 Energy Resolution

The energy resolution represents the probability that an observed gamma-ray event with a particular true energy E_{true} will actually be reconstructed with an observed energy E_{rec}. It

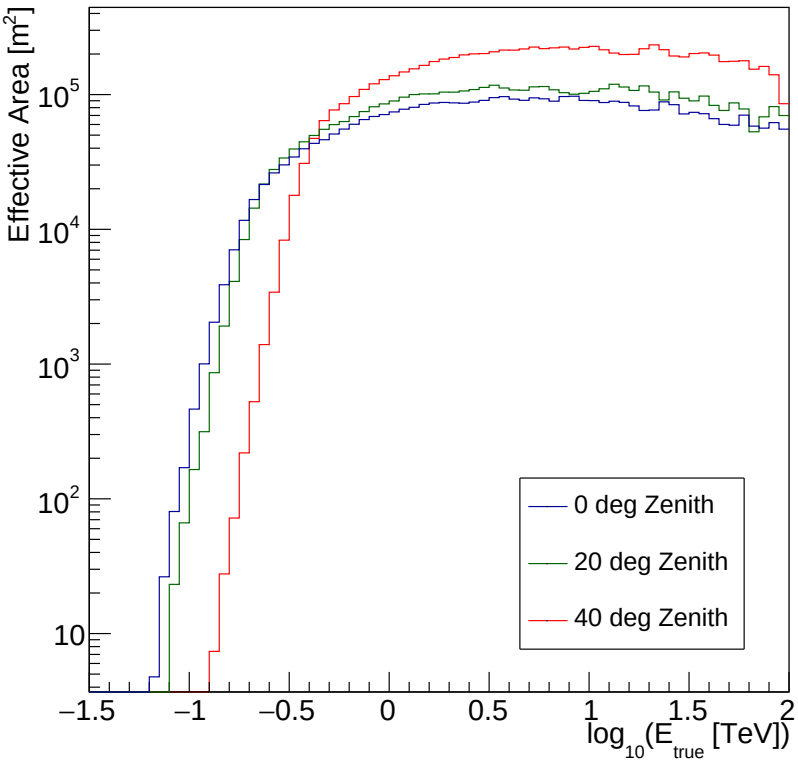

Figure 5.1: Effective area distributions for azimuth 180°, 0.5° offset from the camera center, and for zenith angles of 0° (*blue*), 20° (*green*), and 40° (*red*).

is derived from the same set of gamma-ray air-showers as the effective area IRFs. The energy resolution (R) is determined by counting the number of events simulated with energy E_{true}, but observed with energy E_{rec} after being processed through the standard event reconstruction.

$$R(E_{true}, E_{rec}) = \frac{N_{E_{rec}}}{N_{E_{true}}} \tag{5.7}$$

The energy resolution is stored as a function of (E_{rec}-E_{true})/E_{true}. This ensures the majority of the distributions peak at zero. The distribution is biased at lower energies for reasons discussed in §4.2.2.

5.2.2.4 Point Spread Function

In order to find the best model of the VERITAS gamma-ray PSF several functions were used in an attempt to accurately fit the spatial distribution of events. A Gaussian function, hyperbolic secant, and King function were tried and a King function was decided to work best (see Fig. 5.3). The applied King function is given in Eq. 5.8.

$$PSF(x, y) \propto \left(1 - \frac{1}{\lambda}\right)\left[1 + \frac{1}{2\lambda} \cdot \left(\frac{x^2}{\sigma_x^2} + \frac{y^2}{\sigma_y^2}\right)\right]^{-\lambda} \tag{5.8}$$

Note that the function is allowed to be asymmetric by fitting σ_x and σ_y independently. Generally, however, fits are obtained setting $\sigma_x = \sigma_y$. In particular, fits are obtained for the σ value in narrow ranges of E_{true}. Then an exponential function is fit to the distribution of these values in E_{true} allowing an extrapolation of the PSF at all energies. Care is taken to ensure the King function fits successfully converge in order to determine accurate values of σ otherwise the exponential fits can not be trusted.

The λ parameter is not fit in the above process. It was found that allowing the λ parameter to vary and then fitting for the distribution would cause the extrapolated λ values to become unstable. Instead, λ is fixed for all fits. To find the value that yields the best results, PSF models were generated for a range of λ values from 2.0 to 9.0 in increments of 0.5. The resulting models were fit to a sample of Mrk 501 data. The highest TS from these fits was obtained from the models with λ=2.5. These models were then used in all subsequent analyses.

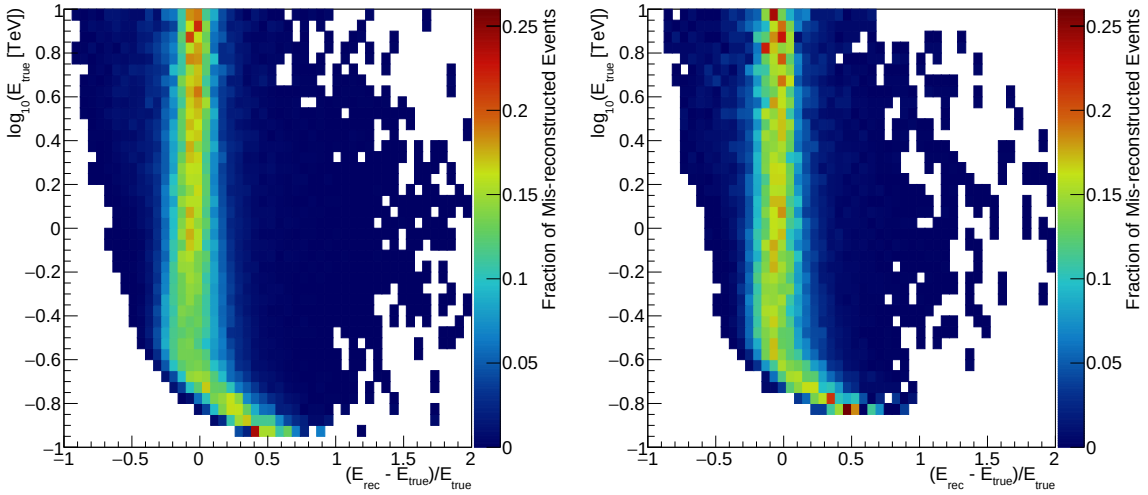

(a) 0° zenith angle

(b) 20° zenith angle

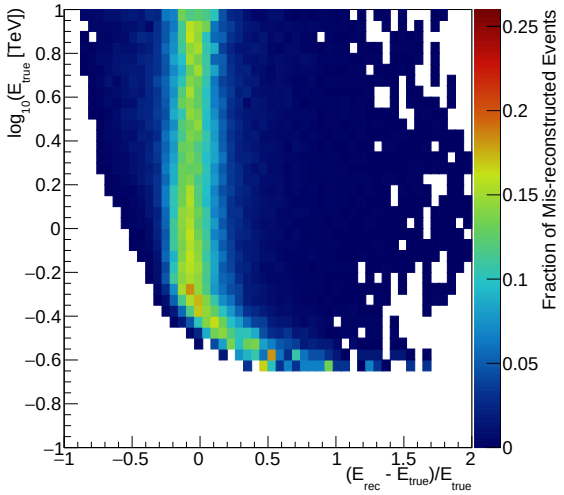

(c) 40° zenith angle

Figure 5.2: Distribution of the fraction of events simulated with energy E_{true} and mis-reconstructed with a given energy value. Plots shown were derived from simulated gamma-ray air-showers observed at 180° azimuth, 0.5° offset, and zenith angles of (*a*) 0°, (*b*) 20°, and (*c*) 40°. Plots also represent only events for which all four telescopes participated in the reconstruction. The plots show the known reconstruction bias observed at lower energies and the increasing low energy threshold at larger zenith angles. The upper cutoff of $E_{true} = 10$ TeV reflects an upper limit to the fully vetted energy range.

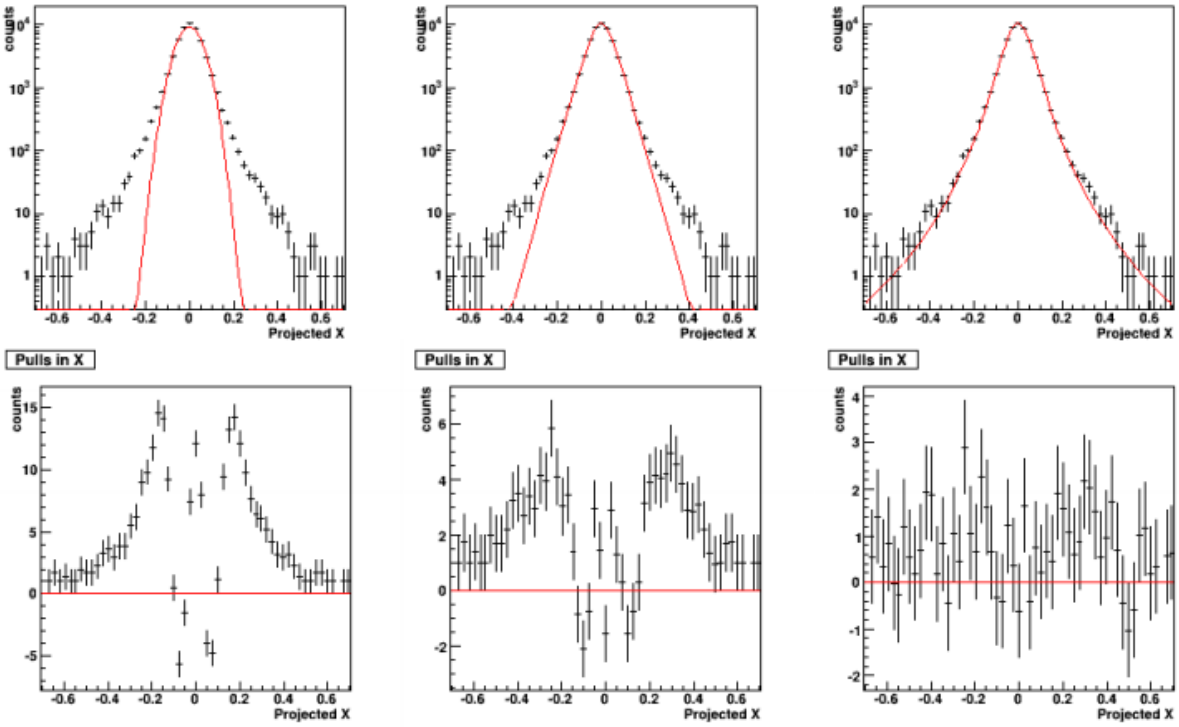

Figure 5.3: Different fits to mono-energetic simulations of gamma-ray events using a Gaussian (*left*), hyperbolic secant (*middle*), and King function (*right*). The bottom plots show the pulls distributions between the events and the model.

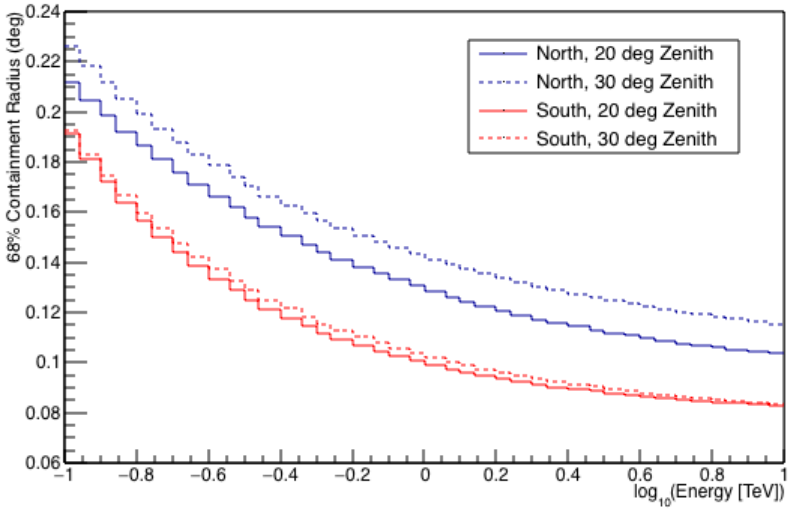

Figure 5.4: Dependence of the 68% containment radius of the VERITAS PSF modeled as a King function. Values are provided over a range of energy, azimuth, and zenith as determined from simulations of gamma-ray air-showers. The x-axis covers the range from 100 GeV to 10 TeV. These models were derived for the fifth epoch of the instrument, winter atmosphere, and all events were observed by all four telescopes.

Based on the fits used here, the VERITAS PSF tends to be poorer at lower energies and improves at higher energies. As an example, for simulated gamma-rays observed at 20° zenith angle, due south and with all four telescopes the observed PSF has a 68% containment radius of 0.13° at 300 GeV. This decreases to 0.099° at 1 TeV, and further to 0.083° at 10 TeV. There is also a dependence of the PSF on observing direction, where the PSF appears to be broader in the northern portion of the sky as opposed to the southern, as is shown in Fig. 5.4. This is due to the geomagnetic fields surrounding the Earth. As the charged particles move through the fields which cause the charge particles in the atmosphere to spread apart (Grieder, 2010b).

5.2.2.5 Source Mean Scaled Width Model

Mean scaled width (MSW) serves as the third dimension in the computed models. The MSW distribution for the signal component is derived from standard simulations of gamma-ray induced air-showers. As mentioned in §4.2.1, the MSW distribution peaks very near 1 for gamma-rays. This is represented in Fig. 5.5. Because of the ample number of events in the simulations from which the source distributions are derived, the MSW distribution is binned

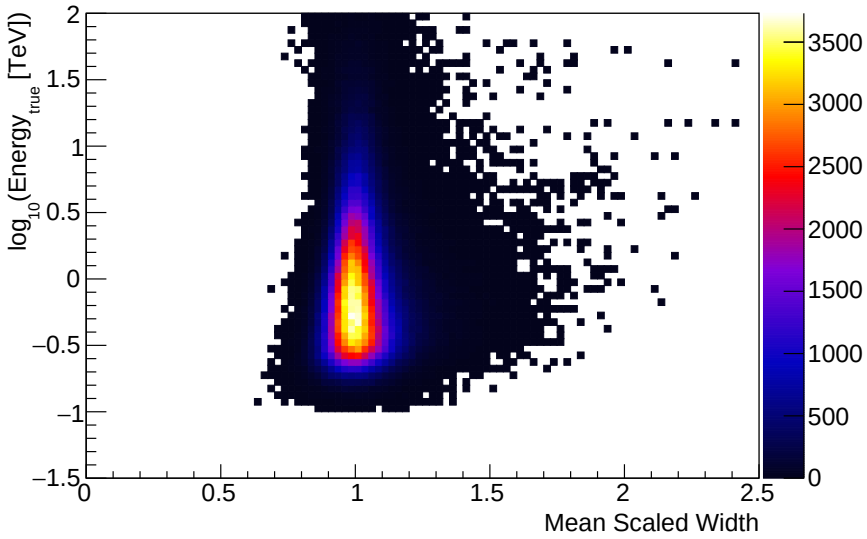

Figure 5.5: Gamma-ray MSW Distribution

Figure 5.6: MSW distributions derived for the source model from simulated γ-ray air-showers. Distributions are shown as a function of logarithmic energy. The color scale represents the number of events used to generate the distribution. Models are extracted for an observation position of 70° elevation, 180° azimuth, and 0.5° offset with four telescopes participating in the shower reconstruction.

in offset at increments of 0.1°. This offset dimension is treated as a *conditional* dimension. When the likelihood for an event is evaluated, the offset from the camera center of the event is computed. Then the MSW distribution for that event is determined by looking up the appropriate distribution at that offset.

5.2.3 Spectral Models

One of the components in accurately modeling the spatial distribution in Eq. 5.5 is the spectral energy distribution of the source. Currently there are three implemented spectral functions in the code:

- **Power law**

$$\frac{dN}{dE} = f_0 \left(\frac{E}{E_0} \right)^{\Gamma} \tag{5.9}$$

- **Log-parabola**

$$\frac{dN}{dE} = f_0 \left(\frac{E}{E_0} \right)^{\alpha + \beta \ln(E/E_0)} \tag{5.10}$$

- **Exponentially cutoff power law** (*not thoroughly tested*)

$$\frac{dN}{dE} = f_0 \left(\frac{E}{E_0} \right)^{\Gamma} e^{E/E_{cut}} \tag{5.11}$$

The starting point of each parameter in the functions can be set in the analysis, or fixed to whatever value they are initially set to. For each model E_0 is the *scale energy* at which the flux normalization (f_0) is evaluated. This value is always fixed and should be chosen near the decorrelation energy, where the correlations between the various fit parameters is a minimum. Doing so results in the smallest errors on the fit parameters and also improves the stability of the fits.

5.2.4 Source Model Implementation

To make the computation of the source model tractable, certain assumptions are employed. The spatial components, B and P, are computed in $0.025^\circ \times 0.025^\circ$ bins. E' is finely binned as well in $log_{10}(E')$ in increments of 0.05 from 0.032 - 100 TeV. This binning in energy is chosen such that it is smaller than the presumed energy resolution of 15% - 20%. As mentioned in §5.2.2.3 the energy resolution is binned in units of $(E_{rec}\text{-}E_{true})/E_{true}$ in narrow bins of $\log E$ and $\log E'$. Therefore, a model that represents the events within a specified range of reconstructed energy must sum over the relevant bins of this distribution as well.

$$S_{src}(\vec{\boldsymbol{r}}_{i,j}|\vec{\boldsymbol{s}}) = \sum_{k,m,n} B_{m,n} P_{m,n}(\vec{\boldsymbol{r}}_{i,j}) A_{m,n}(E'_k) \sum_{E_{min}}^{E_{max}} R_{m,n}(E, E'_k) dE \int_{E'_{k,lower}}^{E'_{k,upper}} S(E'|\vec{\boldsymbol{s}}) dE'. \tag{5.12}$$

Due to the binned nature of the IRFs, the full spatial model for a source within a specified range of reconstructed energy becomes a summation rather than an integration. This provides the expected number of events in the E' bin k, within a spatial bin (i,j). Due to the spatial resolution of the instrument, there is a certain probability that a portion of the emission within a given bin will actually be observed within a nearby bin. This is taken into consideration by summing the contribution from all other bins (indexed by m,n) within 0.5°.

The integration around the spectral function remains as it is often the case that an analytic integral can be done. When available, an analytic solution is preferred as it results in less error and reduces the necessary numeric computation time of the function integral, speeding up the overall analysis. However, a numeric approximation to the integral is still used when such an analytic solution is not readily available. In this case the function is transformed into the $log_{10}(E)$ space and the integral is computed numerically as

$$\int_{E'_{k,lower}}^{E'_{k,upper}} S(E'|\vec{s})dE' = ln(10)\int_{log_{10}(E'_{k,lower})}^{log_{10}(E'_{k,upper})} E' \cdot S(E'|\vec{s})du \tag{5.13}$$

where $u = log_{10}(E')$. The transformation to log space provides a more rapid integration of the integral by preventing the computation from spending a disproportionate amount of time computing the integral in high energy regions where the function changes very little compared to lower energy regions where the function changes rapidly.

Going back to Eq. 5.12, it can be seen that the integral of the spectral function is the only component of the source model that is dependent on the parameters being fit (i.e. the spectral parameters). Because of this, the contribution to the full spatial model from the convolution of the surface brightness model (B) and the PSF (P) along with the relative scaling from the energy resolution (R) and effective area (A) can be precomputed for each of the k narrow bins of E' before the fit. When the the spectral parameters change, the spectral integral is recomputed and each of the spatial models in k can be re-weighted and summed. In this way the fit can be done with far less overhead from recomputing the spatial model for each change in the spectral parameters. This is a crucial aspect in fitting extended sources, as the convolution of B and P is the dominant computation overhead in these models.

5.3 Background Models

The most dominant source of flux in data comes from background sources. Thus accurate background models are needed. This background is dominated by cosmic-rays which are typically protons or atomic nuclei.

5.3.1 Description of Data Used

The background model components were derived using actual observation data taken on sources with either very little or no detectable gamma-ray emission. The background models described in this section were derived from data taken on dwarf spheroidal galaxies (Segue 1, Ursa Minor) and several weak blazars. These sources also had the benefit of being at large galactic latitudes dramatically reducing potential contamination from diffuse emission in the galactic plane. Additionally, data samples were selected such that they contained only a single known or potential gamma-ray source. Regions within 0.4° of any such source were excluded, as were regions within 0.3° of known bright stars[5].

5.3.2 Background Spatial Model

From this data a radial distribution of event counts was derived in narrow bins of squared angular offset from the camera center. A bin-by-bin correction is then applied to account for the area removed by exclusion regions for sources and bright stars. In order to produce a two dimensional spatial model, the radial distributions are fit with a third order polynomial and the resulting curve is extrapolated into a radially symmetric two dimensional map.

A correction is also applied to account for the non-uniform transmission of Cherenkov light as a function of zenith angle. A detailed description of this correction is outlined in Appendix C.

5.3.3 Background Mean Scaled Width Model

Mean scaled width (MSW) serves as the third dimension in the computed models. The MSW distribution for the signal component is derived from standard simulations of gamma-ray induced air-showers. As mentioned in §4.2.1, the MSW distribution peaks very near 1 for gamma-rays. This is represented in Fig. 5.5. The background events, however, are dominated by cosmic-rays. Since cosmic-rays tend to produce broader showers, due to the higher transverse momentum of the particles produced in the shower.

[5] "Bright stars" refers to any star with B magnitude less than 6.

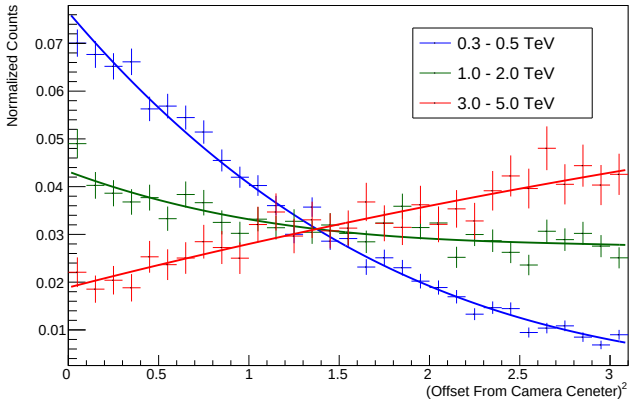

(a) 0°-14.1° zenith angle

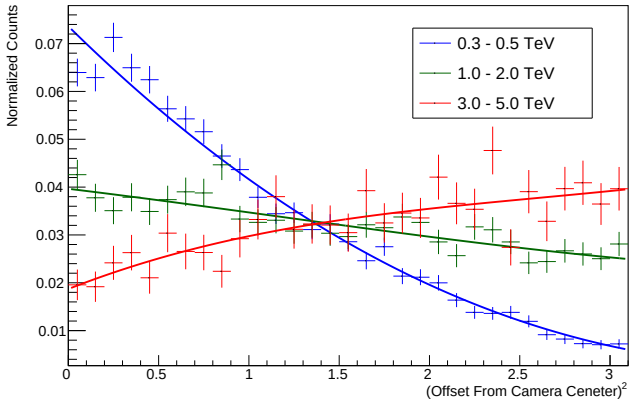

(b) 14.1°-25.5° zenith angle

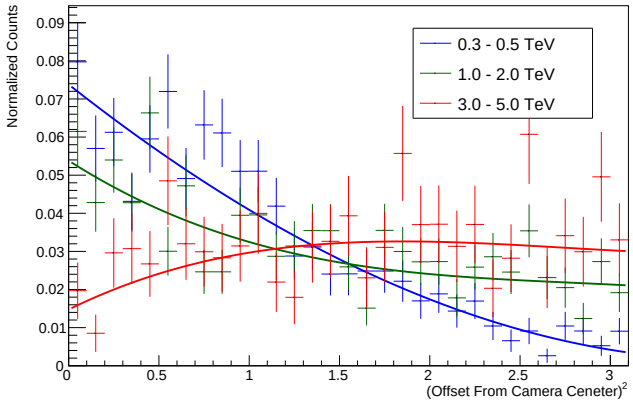

(c) 37.6°-42.6° zenith angle

Figure 5.7: Differences between the distributions of background data (points) used to generated acceptance curves (fitted lines). Shown are curves derived from data taken within the zenith angle ranges of (*a*) 0°-14.1°, (*b*) 14.1°-25.5°, and (*c*) 37.6°-42.6°. Curves are shown for 0.3-0.5 TeV (blue), 1.0-2.0 TeV (green), and 3.0-5.0 TeV (red) and assume four telescopes used in the reconstruction.

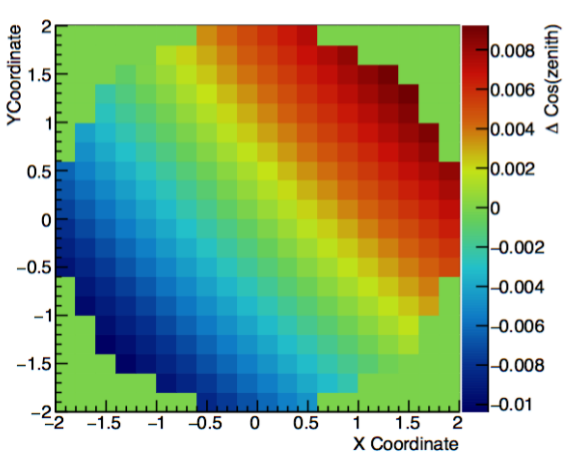

(a) Example zenith gradient map

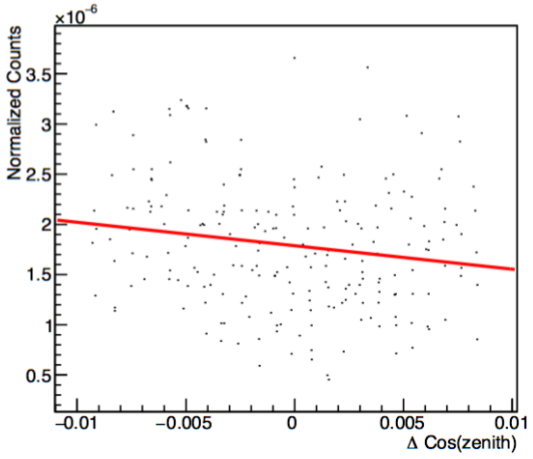

(b) Estimated correction term

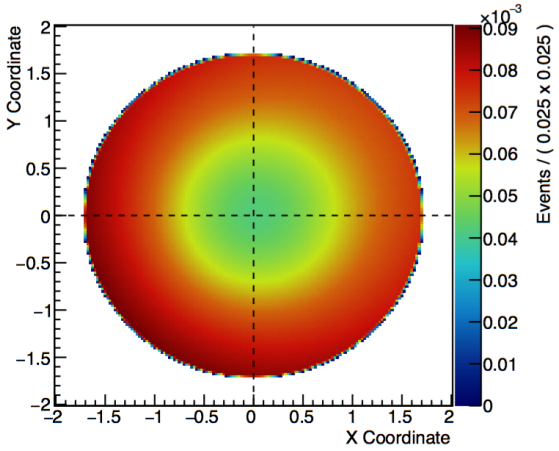

(c) After zenith gradient correction

Figure 5.8: Plots showing how the change in counts across the field of view change as a function of zenith angle. (*top-left*) Diagram showing the zenith gradient across the field of view. (*top-right*) Best fit line to the normalized counts as a function of zenith angle. (*bottom*) Final zenith corrected background spatial model. The model is computed for energies from 2.5-5.0 TeV, 16.4° zenith angle, 237° azimuth angle, and for four telescopes used in the reconstruction.

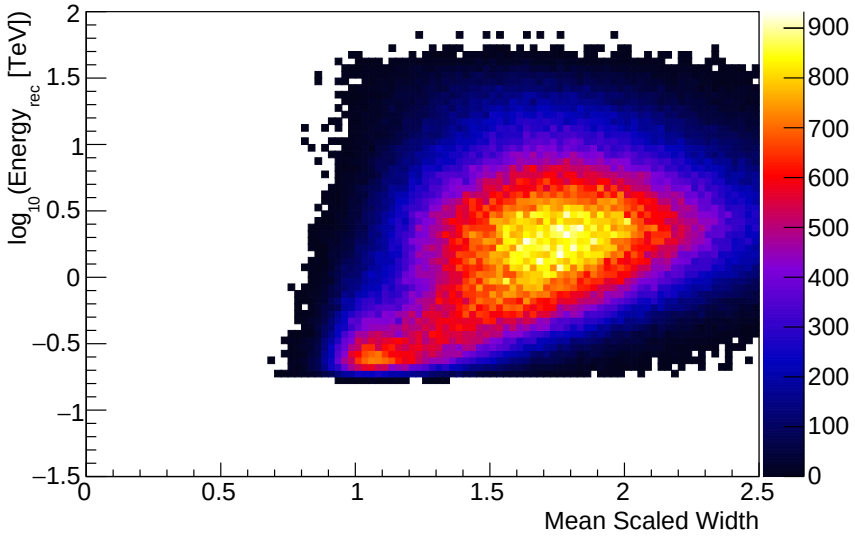

Figure 5.9: Background MSW Distribution

Figure 5.10: MSW distributions derived for the background model from observations. Distributions are shown as a function of logarithmic energy. The color scale represents the number of events used to generate the distribution. Models are extracted for an observation position of 20° zenith angle, 180° azimuth, and 0.5° offset with four telescopes participating in the shower reconstruction.

One of the biggest challenges with modeling the expected background MSW distribution is the dependence on having data runs taken under similar observing conditions in order to model it correctly. Inevitably there will occur regions of the MSW distribution that are poorly defined due to low flux levels (for instance at high energies and low values of MSW). Using the raw distributions in this case would lead to regions where the model predicts zero events, yielding a probability value of zero at this position. Should this be used to evaluate a dataset which happens to have an event in this bin the resulting log-likelihood will be $log(0)$=-∞ causing the fit to fail.

Various approaches were tested to address this low statistics bin issue in the background MSW models. In all cases the agreement between the adjusted models and the data was assessed by fitting various different extended disk templates to samples of assumed blank field data (see §6.5.2 for sources and disk radii used). In this study the models were derived directly from the same sample of data used in the fit to ensure a good match. Smoothing the distributions resulted in a change to the underlying shape of the distribution and was not a good fit. Next, a functional fit was attempted, however, this too distorted the shape such that the distribution would not be a good match to the data. In both of these situations, there were ultimately some bins which would be empty in the model. An event padding of 0.1 events was added to these bins to prevent the fit from failing.

In such a case where the model is being derived from a low statistics data sample, the ultimate solution was adopted from Barlow and Beeston (1993). The adaptation of this technique uses a set of nuisance parameters. The parameters allow the model to float freely in these low statistics bins while being constrained by the data that was used to originally derive the model. When more data is added to the sample used to generate the background MSW models, this constraint becomes stronger and less leeway is given to the fit to adjust the model in these bins. As a result the model value in this bin is able to adjust itself to find the best value possible that is a decent compromise between the data being analyzed and the data used to generate the model from.

Currently, the threshold for defining a bin as having *low statisitics* (and thus needing to be modeled as a nuisance parameter) is when the bin value is derived from fewer than two events.

In order to keep the analysis flexible this threshold value can be set to any value at the time of the analysis, however large threshold values were found to make the fit unstable. This is presumably the result of increasing the number of free parameters in the fit.

5.4 The Full Model

The VERITAS MLM models consist of both a two dimensional spatial model and a mean scaled width model (MSW) for both the γ-ray (source) and background components. In this way the full log-likelihood for a single observation becomes

$$\begin{aligned} log(L(\vec{s})) =& N_{obs} log(N_{exp}) - N_{exp} \\ &+ \sum_{i=1}^{d} log\left[S_{src}(\vec{r}_i|\vec{s}) \cdot W_{src}(w_i|\vec{s}) + S_{bkgd}(\vec{r}_i) \cdot W_{bkgd}(w_i)\right] \\ &+ N'_{obs} log(N'_{exp}) - N'_{exp} + \sum_{j=1}^{p} log\left[W'_{bkgd}(w_j)\right] \end{aligned} \tag{5.14}$$

To correlate the spatial source model (S_{src}) with the MSW source model (W_{src}), the product of the two distributions is taken (similarly for the background component). An additional term is included in the likelihood to model the total expected number of events from both signal and background. The expected number of events in a dataset is taken to be Poisson distributed with expected events N_{exp} and observed events N_{obs}. The first two terms in Eq. 5.14 are based on this assumption. The data is treated as unbinned in the spatial and MSW dimensions and coarsely binned in reconstructed energy. The free parameters are spectral parameters associated with the source being modeled. Note that although Eq. 5.14 only includes one source mode, there is actually no limit to the number of source models that can be included.

The third line in Eq. 5.14 denotes the component of the likelihood which accounts for the nuisance parameters described in §5.2.2.5. Here N'_{obs} is the sum of counts in the MSW distributions which are derived from background data samples. N'_{exp} is the same as N'_{obs} with the exception that bins identified as being replace with nuisance parameters are also replaced in this sum with the current value of the associated nuisance parameter. The summation term applies a shape constraint to the overall distribution. The j index implies the PDF is evaluated for each event from the background data sample used to derive the MSW background

distribution. As a result the nuisance component serves as a constraint on the overall likelihood, reducing the computed value in cases where the data deviates from the model.

It follows that to analyze data from multiple observing positions, each field can be independently modeled and the resulting log-likelihoods summed to get a likelihood for the entire observation set simultaneously. Since all models share the same free parameters (independent of the observing conditions between fields) this can be extended to observations which cover a range of detector configurations or even to connect observations from different detectors.

CHAPTER 6. MAXIMUM LIKELIHOOD PERFORMANCE STUDIES

6.1 Comparison of RBM and 3D MLM Sensitivity: 2FHL J0431.2+5553e

6.1.1 Ring Background Model

Because of the limitations of the RBM technique mentioned in §4.3.3, the analysis of 2FHL J0431.2+5553E data cannot rule out that there is in fact a source present. To evaluate whether it is possible that such a source exists, and whether the source could actually be detected by VERITAS, a sample of Monte Carlo events was generated assuming a spectrum as derived by Ackermann et al. (2016). Specifically, a source was simulated with differential flux of 1.17×10^{-7} TeV^{-1} m^{-2} s^{-1} at 1 TeV, spectral index of -1.66, and a disk morphology of radius 1.27°. The source was assumed to be observed with an exposure of ∼20.8 hours in wobble mode at its highest elevation. In order to match the RBM analysis of real data presented in §4.3.4, which uses a separate sample of data to estimate the background, a separate simulation was run with the same observing parameters, but assuming no source present.

Analysis of several hundred such studies showed peak significances between 4.7 - 6.8. Significance maps are shown for four of these studies in Fig. 6.1. Caution should be exercised in interpreting this as positive evidence that the RBM analysis would be capable of detecting such a large source for the following reasons:

- The observing strategy used provides the greatest number of observed events from the source. More realistically the observations would be taken over a range of zenith angles, including less ideal positions reducing the observed number of photons from the source.

- Spectral indices derived from the *Fermi*-LAT data typically have harder spectral indices as compared to those at VERITAS energies. For this reason, it would be more realistic

to assume the spectrum will become softer (i.e. a lower spectral index) leading to a lower observed flux rate in VERITAS data.

- The above significances are *pre-trials*, meaning that the true significance observed will need to be corrected to taken into account the number of locations searched in the map. This will also lower the significance derived from each study.

Each of the above factors will lower the significance. Because the average significance from these studies falls just above the cutoff at which VERITAS claims detection (i.e. significance > 5), it is not unreasonable to expect these significances to fall below the cutoff after taking into consideration the above factors. Perhaps the most important of the these factors is the second, highlighting differences between the derived spectra from *Fermi*-LAT and VERITAS. A spectral index of -1.66 in VERITAS data is highly optimistic, as most high energy SNR have spectral indices $\lesssim$-2.0 as observed with IACTs.

6.1.2 3D MLM

The simulated observations of 2FHL J0431.2+5553e presented in §6.1.1 were also processed through the 3D MLM. This allows a comparison of the sensitivity between the RBM and 3D MLM techniques. One caveat should be mentioned before discussing the results of this study, which is that the 3D MLM analysis uses models that are a perfect match to the data being analyzed. This will result in a slightly over optimistic TS in the analysis.

The results of these 3D MLM analyses are shown in Fig. 6.2. The fitted values for the flux normalization and spectral index appear to be normally distributed about the simulated values of 1.17×10^{-7} (TeV^{-1} m^{-2} s^{-1}) and -1.66, respectively. Additionally, the TS values appear to be Gaussian distributed, with a mean around TS$\approx$750 and σ=61.6, corresponding to an approximate significance ($\sqrt{TS}$) of $\sim$26.2-28.4σ. This represents a marked increase over the results for the same sample as analyzed with the RBM demonstrating the improved sensitivity of the new technique to extended sources.

An update to the 2FHL catalog is currently in preparation (The *Fermi*-LAT Collaboration, 2017), but updated spectral parameters and source extension estimates have been made avail-

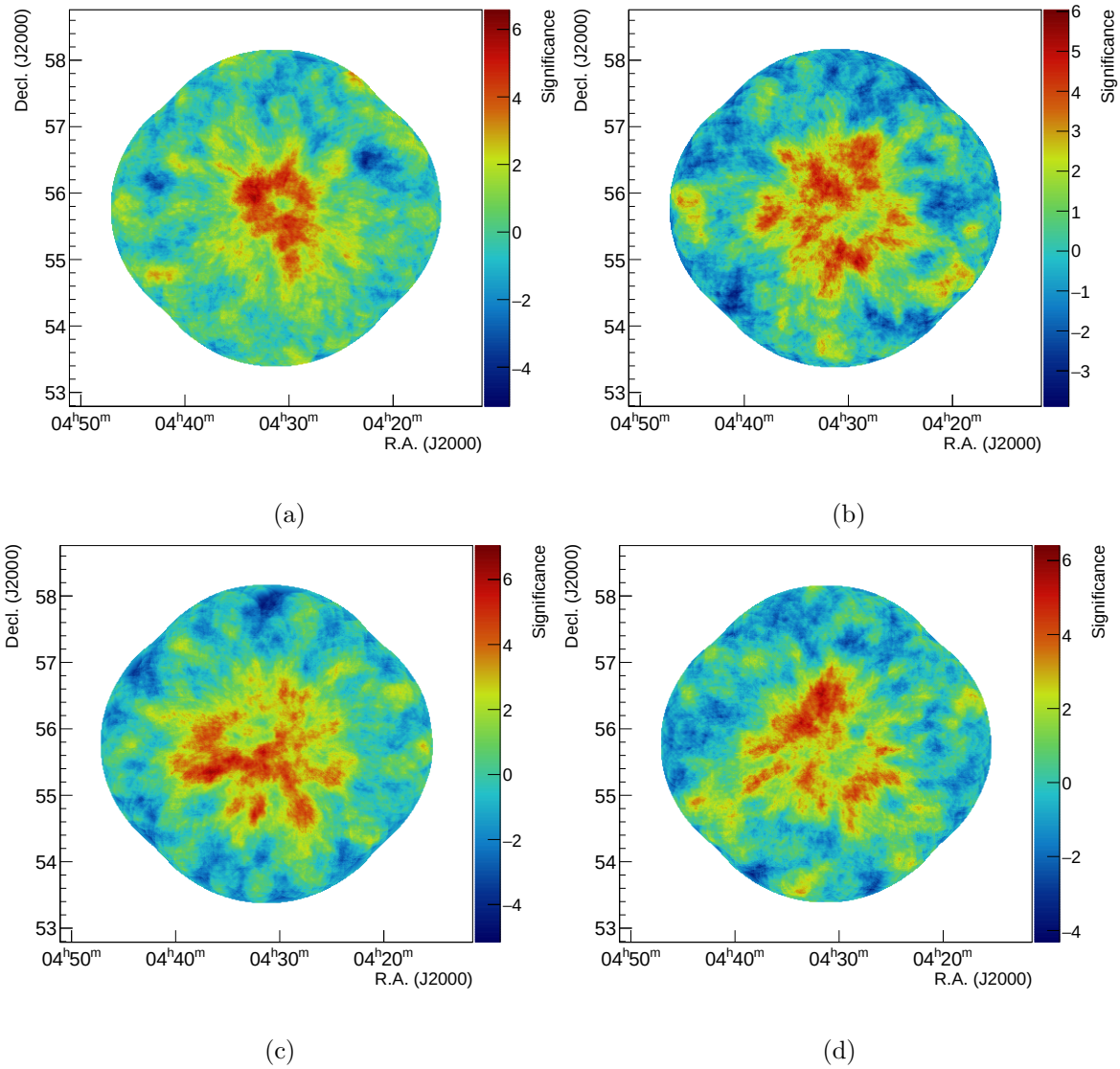

Figure 6.1: Significance sky maps for a small sample of the simulated 2FHL J0431.2+5553e studies analyzed using the standard VEGAS RBM analysis. An integration radius of ∼0.224° was used.

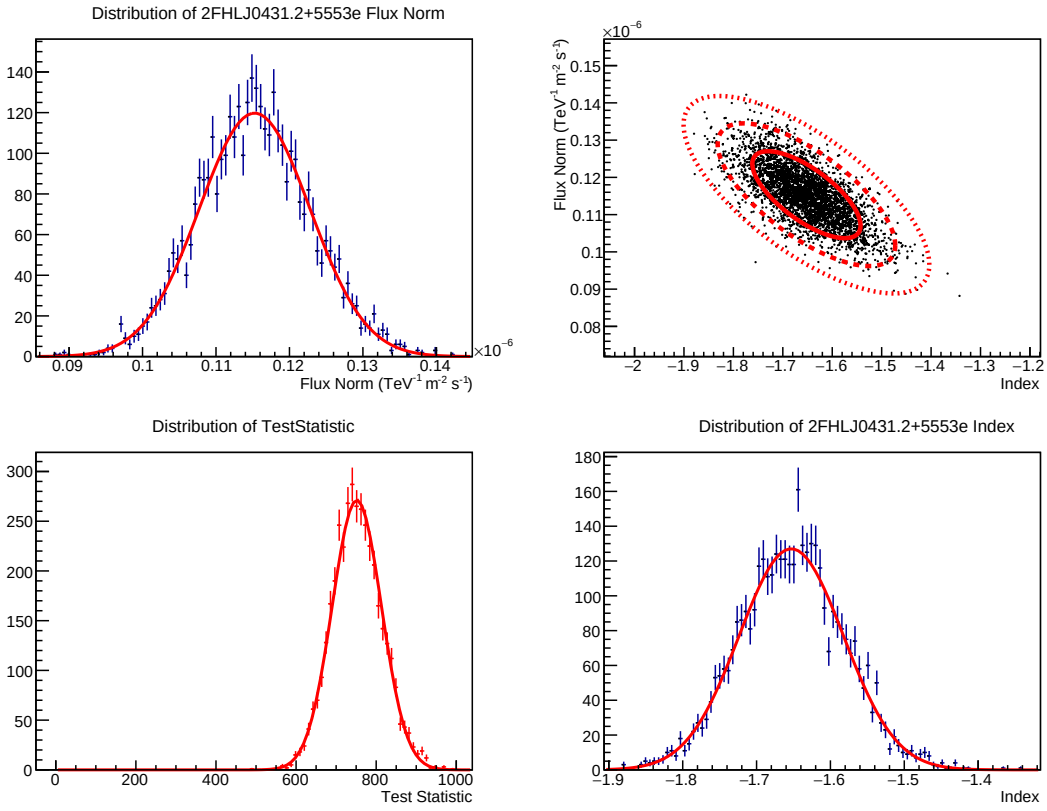

Figure 6.2: Distribution of fit parameters for the simulated 2FHL J0431.2+5553e source as analyzed with the 3D MLM. Specific parameters shown are the flux normalization at 1 TeV (*top left*), spectral index (*bottom right*), and fit TS values (*bottom left*). Each distribution appears to be Gaussian distributed (red curves). Also shown is the distribution of flux normalization versus spectral index (*top right*) with corresponding one, two, and three standard deviation error ellipses (solid, dashed, and dotted lines respectively). The correlation plot suggests that the decorrelation energy (i.e. where the correlation between the flux normalization and index is a minimum) is at a higher energy than the 1 TeV value used in this study.

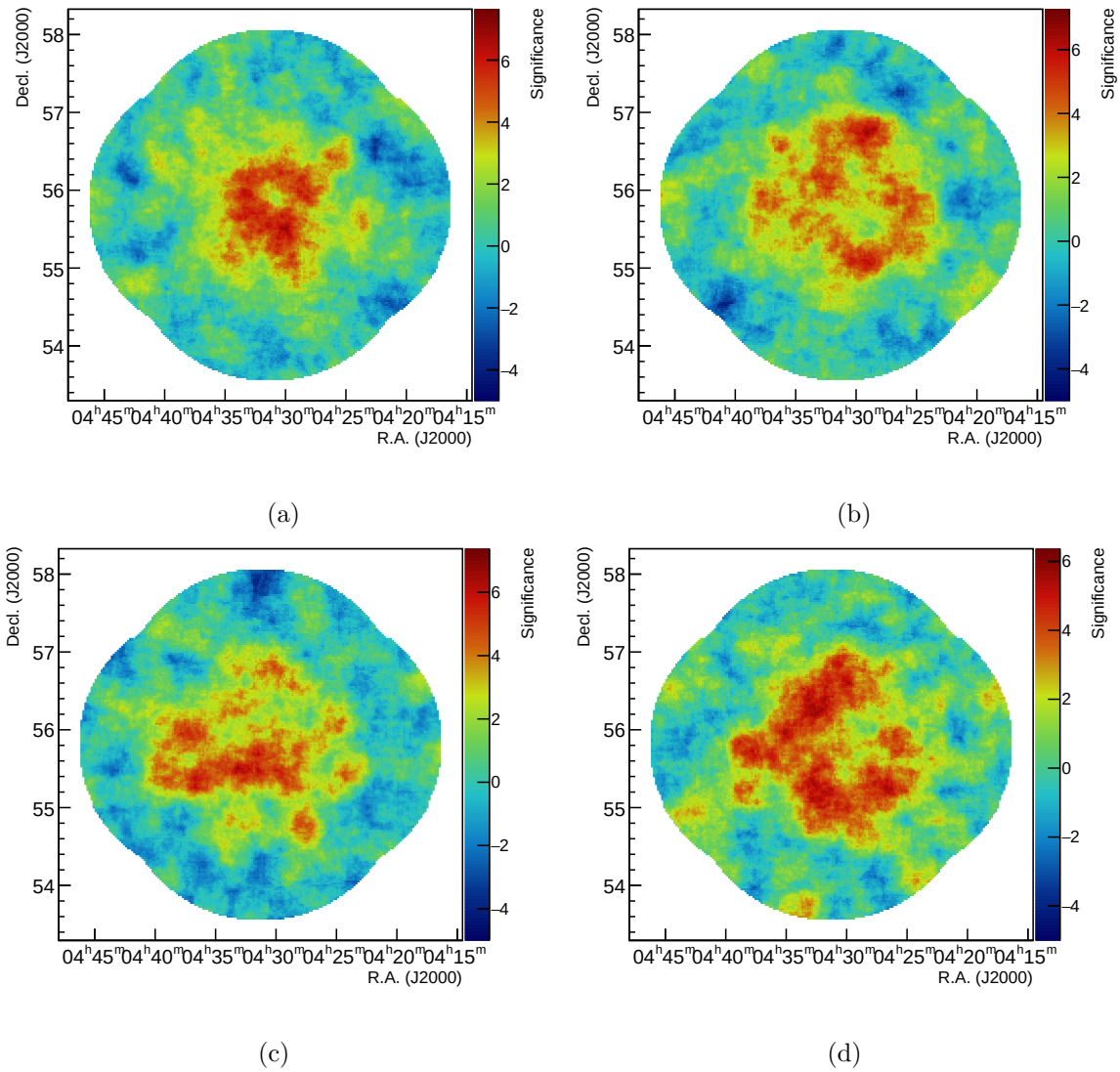

Figure 6.3: Significance sky maps for a small sample of the simulated 2FHL J0431.2+5553e studies analyzed using the 3D MLM analysis presented here. An integration radius of ∼0.224° was used. These maps are derived from the same data sample as the RBM significance sky map presented in Fig. 6.1.

able to the public[1]. 2FHL J0431.2+5553e has been updated to 3FHL J0427.2+5533e which is now modeled as a disk with radius 1.515°. The updated integral flux normalization is 6.83 (± 0.60) × 10^{-10} (photons cm^{-2} s^{-1}) from 10 GeV to 1 TeV with a spectral index of -1.92 (± 0.08). This results in a softer spectrum and a more diffuse source, both of which represent additional challenges for the standard RBM technique. Simulating this source provides an updated set of distributions (see Fig. 6.5) and the predicted TS from the 3D MLM is in the range 190-250. This suggests that even with the reduced flux and larger extension, the source should be well within the capabilities of the 3D MLM.

Another cross-check that can be done involves looking at the generated background-only events. These simulations were used to derive an estimate of the background in the RBM study. The important result of this analysis is the distribution of TS values. Recall from §5.1.2 that Wilks' theorem predicts an exponential distribution for the derived TS values from many studies when the test model includes two additional free parameters (see also Eq. 5.3). Fig. 6.7 shows the distribution of TS for these blank field analyses which appear to follow an exponential distribution (represented by a red line).

Using these studies, an estimate of the significance can be derived from the relationship

$$prob = \frac{1}{2} \cdot \frac{\int_{T_0}^{\infty} e^{-s \cdot T} dT}{\int_{0}^{\infty} e^{-s \cdot T} dT} \tag{6.1}$$

where T represents the test statistic (TS) and *prob* is the probability of obtaining a TS value $\geq T_0$. The factor of 1/2 comes from the fact that half of our simulations are piled up at $TS = 0$, as negative source fluxes are not allowed. A comparison of *prob* to the same integration of the normal distribution allows a characterization of TS in terms of significance. Fits from the above analyses provide values for s of 0.624 (2FHL source analysis) and 0.672 (3FHL source analysis). This suggests that a TS of 25 corresponds to a significance of 5.23-5.45σ. In each analysis these exponential fits are based on approximately 1200 simulations. This number is clearly far too few to say with certainty what the TS to significance relation is, however it does suggest that requiring TS > 25 for establishing a source as *detected* is reasonable.

[1] $https://fermi.gsfc.nasa.gov/ssc/data/access/lat/3FHL/gll\_psch\_v11.fit.gz$

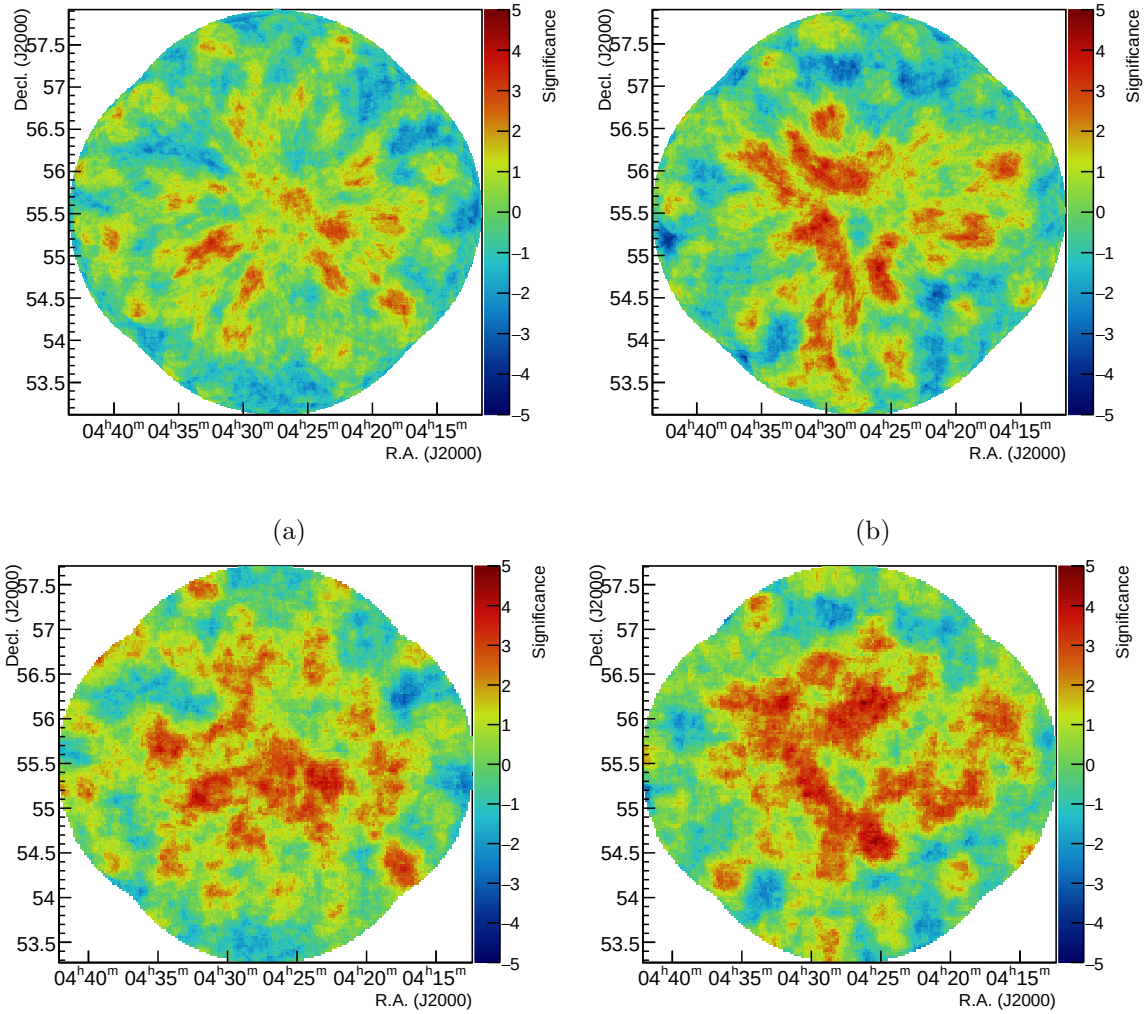

Figure 6.4: Comparison significance maps for two simulated observations of 3FHL J0427.2+5533e produced with the standard RBM (*top*) and 3D MLM (*bottom*) analysis techniques. All maps use a source integration radius of $\sim 0.224°$.

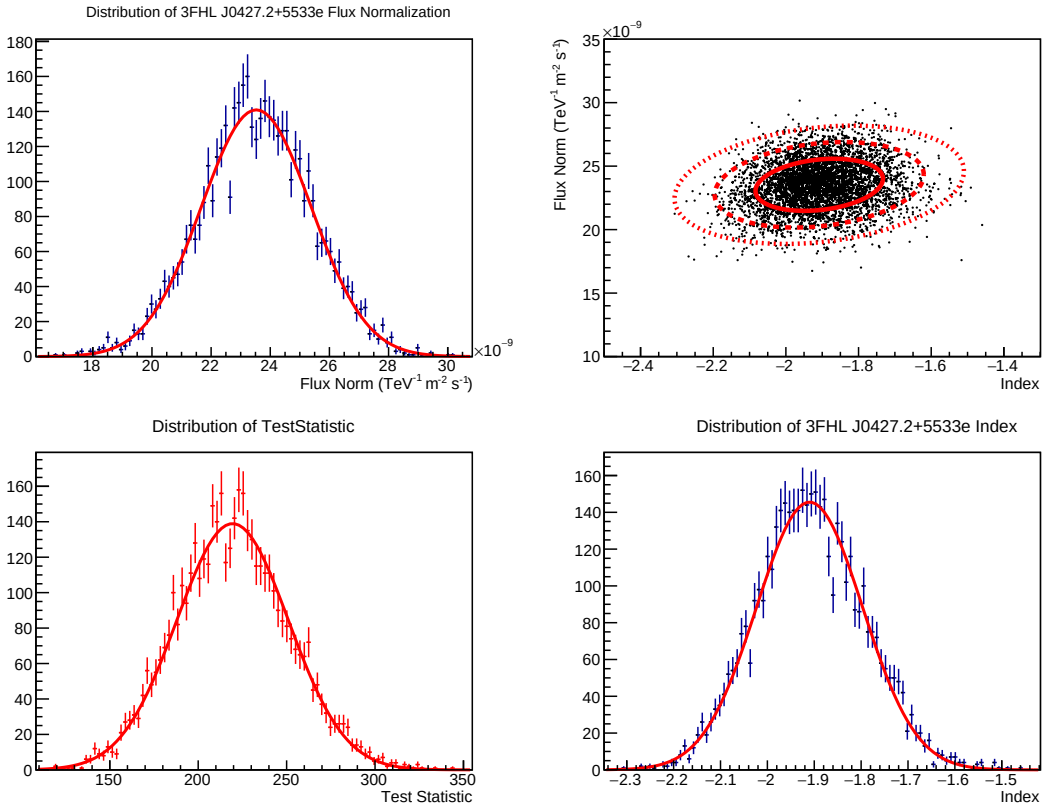

Figure 6.5: Distribution of fit parameters for the simulated 3FHL J0427.2+5533e source as analyzed with the 3D MLM. Specific parameters shown are the flux normalization at 2 TeV (*top left*), spectral index (*bottom right*), and fit TS values (*bottom left*). Each distribution appears to be Gaussian distributed (red curves). Also shown is the distribution of flux normalization versus spectral index (*top right*) with corresponding one, two, and three standard deviation error ellipses (solid, dashed, and dotted lines respectively). It can be seen from the correlation plot that adjusting the scale energy to 2 TeV reduces the correlation between the flux normalization and index.

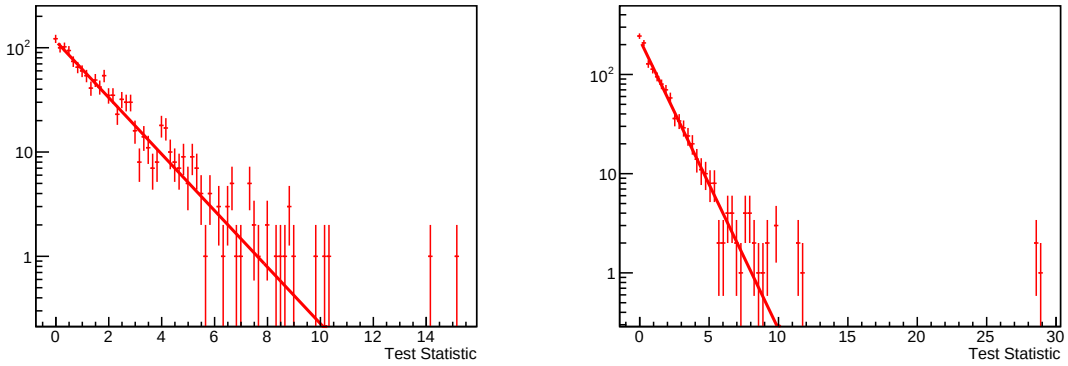

(a) (b)

Figure 6.7: Distribution of TS values for simulations of a blank field containing no source of gamma-ray emission. Plots are shown for the fits of the source as described in the 2FHL (*a*) and 3FHL (*b*) catalogs. The fit line represents the best fit exponential function which can be used to estimate the relationship between TS and detection significance.

6.2 Studies of Actual Data

As mentioned in the previous chapter, the source models of the 3D MLM are constructed from inputs based on simulations of gamma-ray airshowers. The background models are constructed under the assumption that the background is well characterized from data taken in other fields. As a check that these inputs and the models derived from them are an adequate match to actual data taken by VERITAS, several test data sets have been processed through the 3D MLM. These data sets have also been analyzed with the standard RBM method. This chapter will outline these studies.

As the goal is to present a simple verification analysis of the method, few details will be given regarding each source analyzed. The data analyzed below meets the following criteria:

- Taken between September 2009 and July 2012 (V5 epoch)
- Taken during the winter months (November through April)
- All four telescopes were operational during the observations

These criteria were chosen as they overlap with planned first pass analysis of the Geminga extended emission. For each analysis the data is also binned in equally spaced bins of $\log_{10}E_{rec}$ from 316 GeV to 5.01 TeV. This energy range was chosen so as to avoid issues with the energy bias at low energies and with poor energy reconstruction and low background statistics at high energies. All fit spectral parameters in this chapter are provided with purely statistical errors.

6.3 Known Point Sources

In this section the performance of the 3D MLM when analyzing several known point sources of gamma-ray emission is assessed. A point source is defined as any source whose extension is smaller than the gamma-ray PSF of the instrument ($\lesssim$0.05° radius). The same data is also analyzed using the standard VEGAS RBM technique. Comparing the results of the 3D MLM and the RBM analyses provides an evaluation of how well the 3D MLM can reproduce the spectrum of a given source. For bright sources, this study will also allow evaluating the accuracy of the source model construction, in which the PSF, effective area, and energy resolution are folded together.

6.3.1 Crab Nebula

The Crab Nebula is among the brightest, reasonably steady point sources of emission above a few hundred GeV. As a result, it is often used for validating new analysis techniques in VERITAS. The spatial significance map and MSW residuals for ∼30.3 hours of Crab data analyzed with the 3D MLM are shown in Fig. 6.8 and Fig. 6.10 respectively. The Crab was modeled as a log-parabolic function (Eq. 6.2).

$$\frac{dN}{dE} = f_0 \left(\frac{E}{E_0} \right)^{\alpha+\beta \cdot ln(E/E_0)} \tag{6.2}$$

The best fit spectral values were found to be α=-2.47 (± 0.02), β=-0.13 (± 0.02), and f_0=3.85 (± 0.06) x 10^{-7} TeV^{-1} m^{-2} s^{-1} evaluated at E_0=1 TeV. These values are in agreement with the standard RBM analysis (blue line, Fig. 6.11).

Because the Crab nebula is one of the brightest sources observable by VERITAS, it provides an opportunity to assess the source model construction. Comparing Fig. 6.8a and Fig. 6.8b reveals that the model is able to account for a significant portion of the emission from the source, thus reducing to a large degree the peak significance in the map. The residual map in Fig. 6.9b demonstrates that there are still some discrepancies in the modeling of the source. Around the source position, where the integrated excess appears to peak at 324 (counts / 0.0314 deg^2) above the background. There are also two regions about 0.17° above and below the source position which result in an over subtraction and a deficit of counts. In terms of

the total number of counts in the map, there are approximately 9775 events after background subtraction. After subtracting the source model, there are -115 events, implying an overall over subtraction of ∼1.2%. Combined with the relatively good agreement between the spectra derived from both the 3D MLM and the standard RBM (see Table 6.1), results suggest that the emission is well accounted for by the model.

6.3.2 Mrk 501

Mrk 501 is a bright blazar located at $\alpha = 16\text{h } 53\text{m } 52.2\text{s}$, $\delta = +39°45'37''$ [2]. This declination places the source on the northern portion of the sky as viewed from the VERITAS observatory, opposite from from the Crab nebula which is in the southern sky. Approximately 7.4 hours of Mrk 501 data was analyzed with the 3D MLM and the resulting spatial significance map (Fig. 6.12) and MSW residuals (Fig. 6.14) have been included. The spectrum was modeled as a power law according to Eq. 6.3.

$$\frac{dN}{dE} = f_0 \left(\frac{E}{E_0} \right)^{\Gamma} \tag{6.3}$$

The best fit spectral values (Fig. 6.15) were found to be Γ=-2.35 ($\pm$ 0.05) and f_0=2.79 ($\pm$ 0.09) x 10^{-7} TeV^{-1} m^{-2} s^{-1} evaluated at E_0=0.75 TeV.

Although not as bright as the Crab nebula, Mrk 501 is still sufficiently bright to provide insight to the quality of the models. Fig. 6.12b shows that the same features present in the Crab residual map are also present in the Mrk 501 residual map. Specifically, a peak excess at the source position and deficits above and below the source position. The total excess counts predicted after subtracting only the background models is about 812 counts. Subtracting the source model as well results in a deficit of 91 counts, yielding an over subtraction of ∼11.2%. Including a larger data sample could reduce the errors on the fitted values of the spectrum and improve the overall fit and source modeling. Despite the the apparent over subtraction of the source, the fitted spectral values are still in good agreement with the standard RBM analysis (see Table 6.1).

[2] Posisition from NASA/IPAC Extragalactic Database (http://ned.ipac.caltech.edu/).

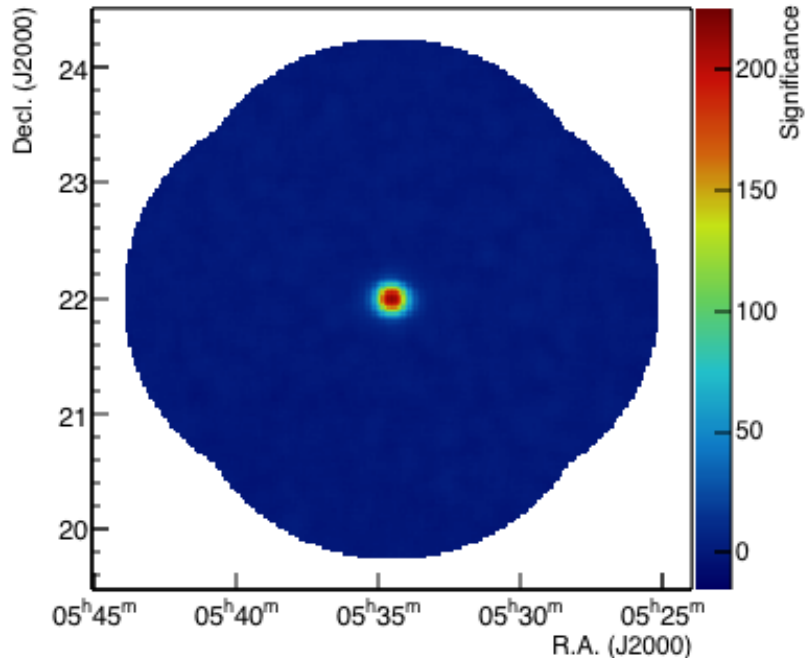

(a) Crab Significance Map

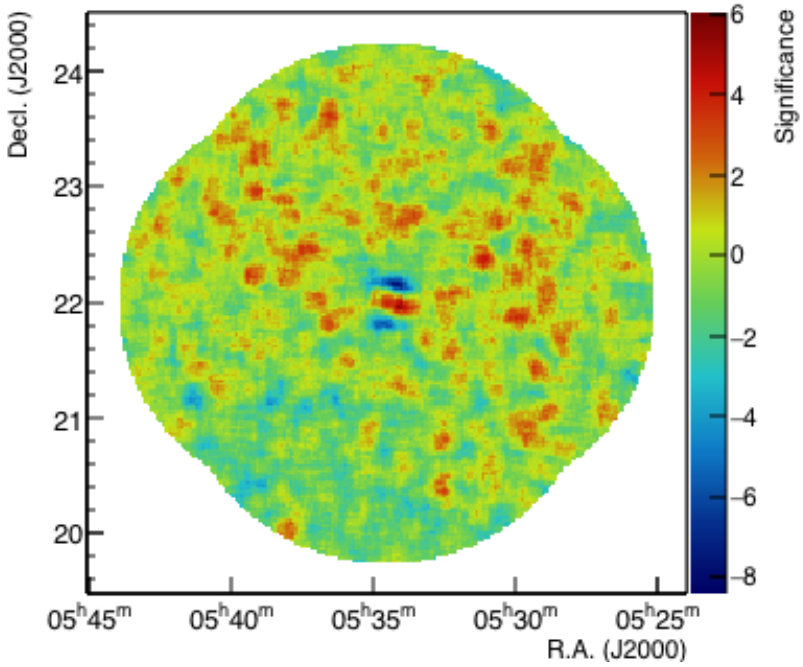

(b) Crab Source Subtracted Significance Map

Figure 6.8: (*a*) Spatial significance map of the Crab nebula computed without the Source model and (*b*) with the source model.

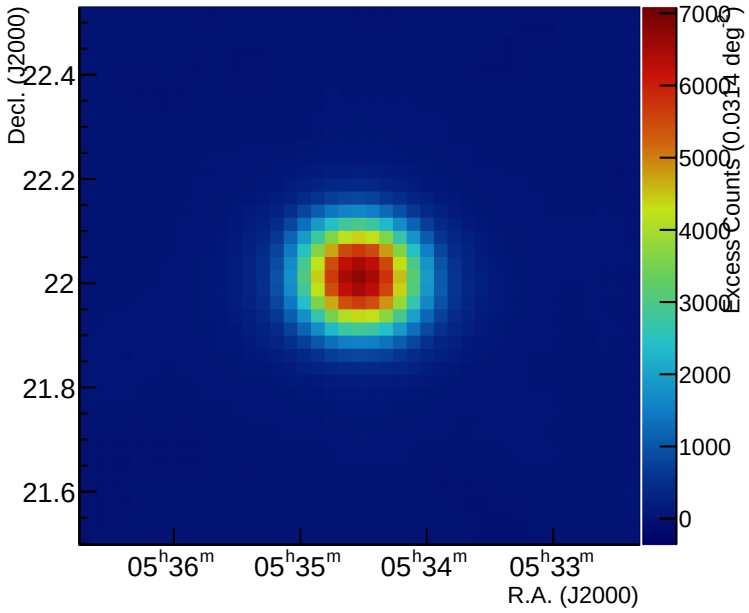

(a) Source Included

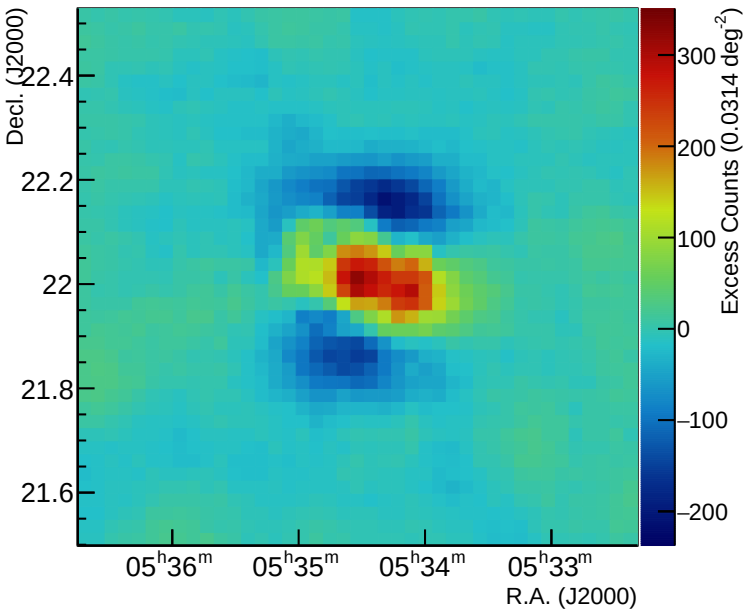

(b) Source Excluded

Figure 6.9: Zoomed excess sky map of the region around the source position for the Crab nebula with (*a*) source included and (*b*) source subtracted. Features in the lower map highlight differences between the model and the data.

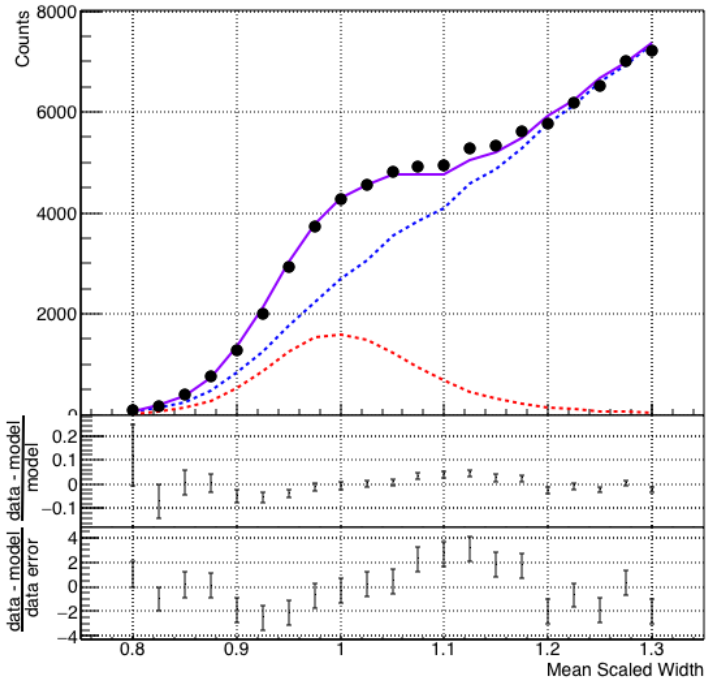

(a) Full Field MSW distribution

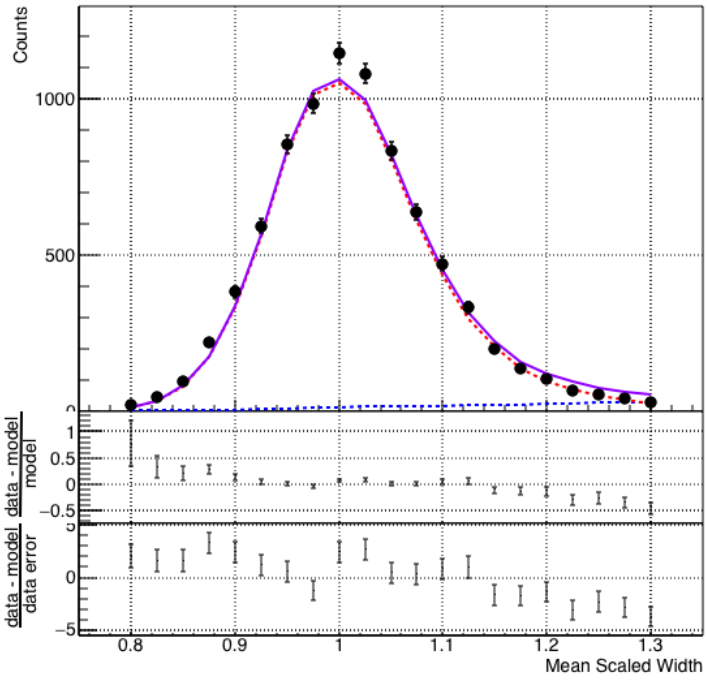

(b) Within 0.1° of source position

Figure 6.10: (*a*) MSW distribution for both the entire Crab nebula field of view and (*b*) only events within 0.1° of the source position. Plotted are the data (black points), background model (blue dashed), source (red dashed), and full models (purple solid).

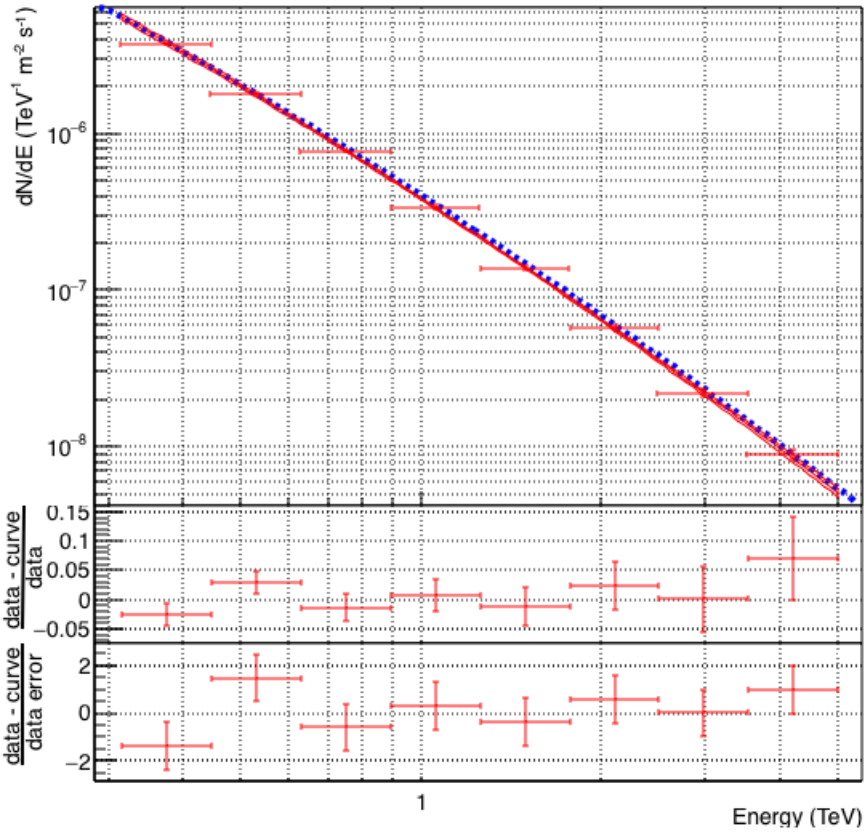

Figure 6.11: Best fit spectrum for the Crab nebula. The best fit from the standard VEGAS analysis (blue dashed line) is also plotted.

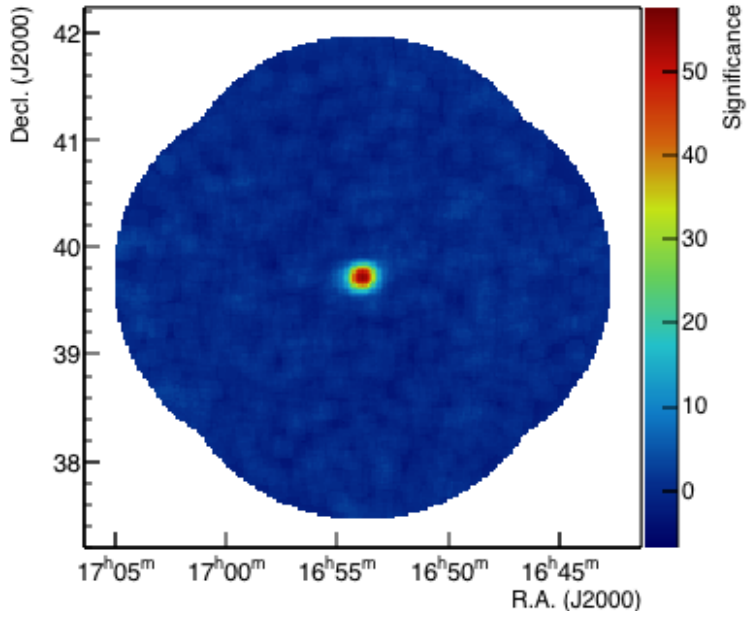

(a) Significance Map

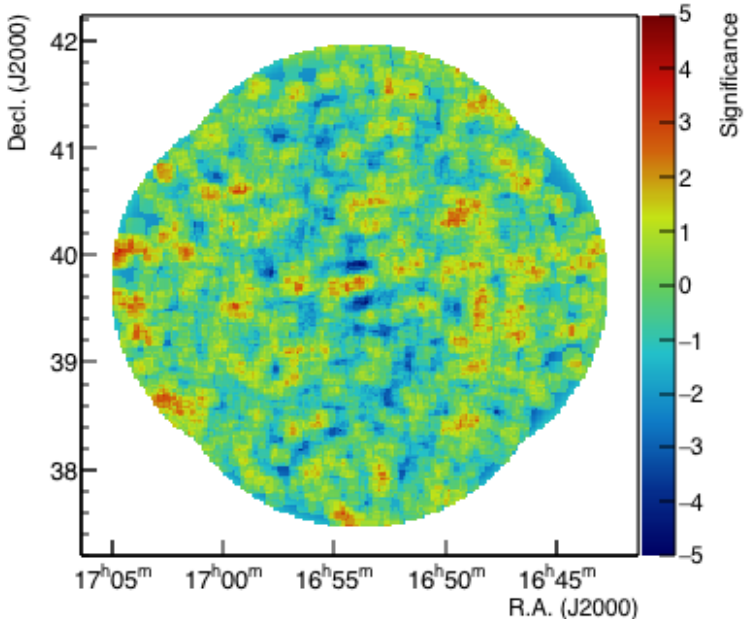

(b) Source Subtracted Significance Map

Figure 6.12: (*a*) Spatial significance map of the Mrk 501 computed without the Source model and (*b*) with the source model.

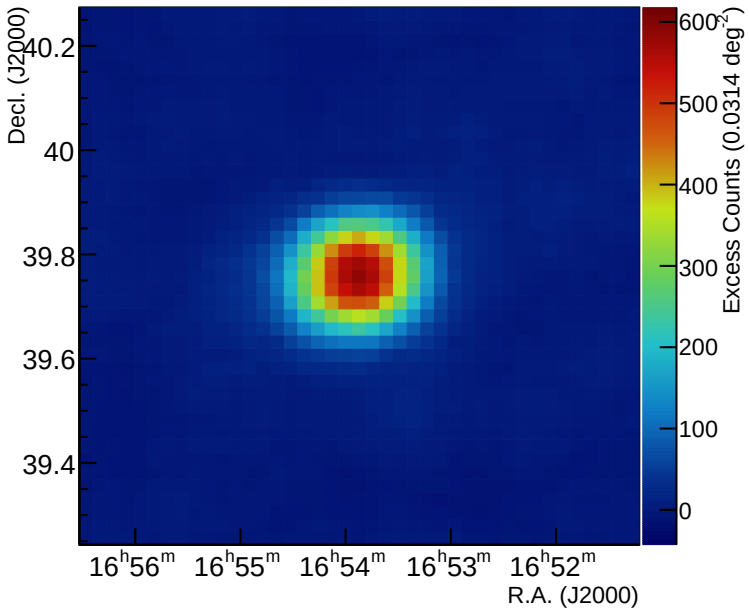

(a) Source Included

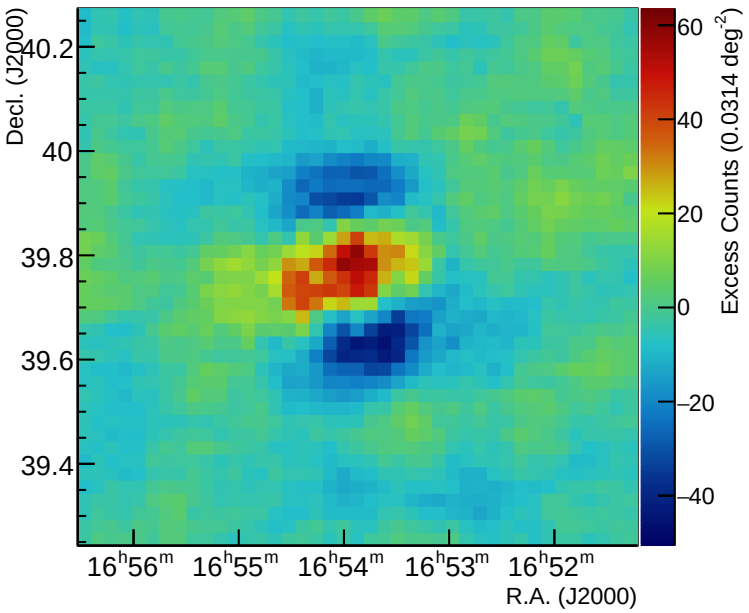

(b) Source Subtracted

Figure 6.13: Zoomed excess sky maps of the region around the source position for Mrk 501 with (*a*) source included and (*b*) source subtracted. Features in the lower map highlight differences between the model and the data.

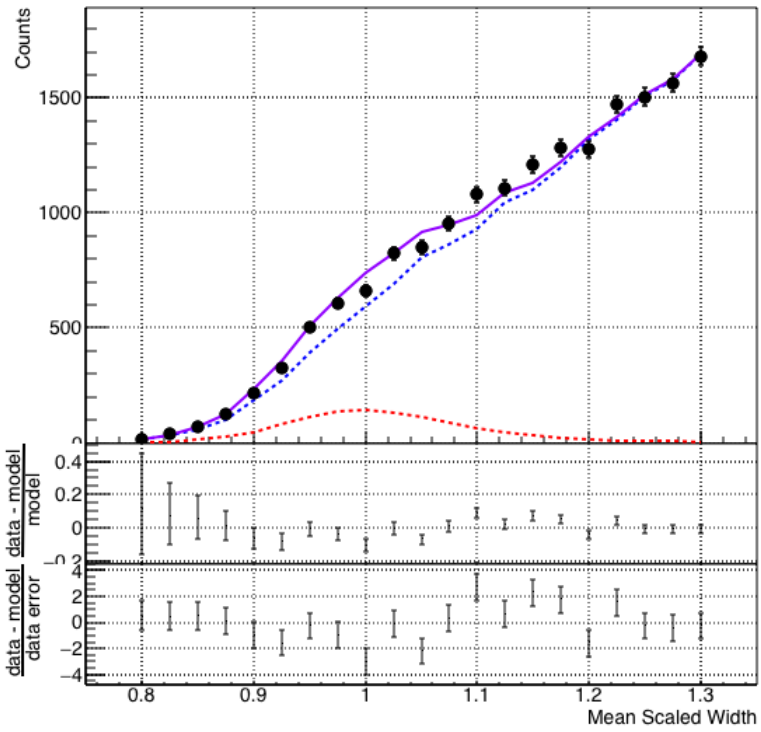

(a) Full Field MSW distribution

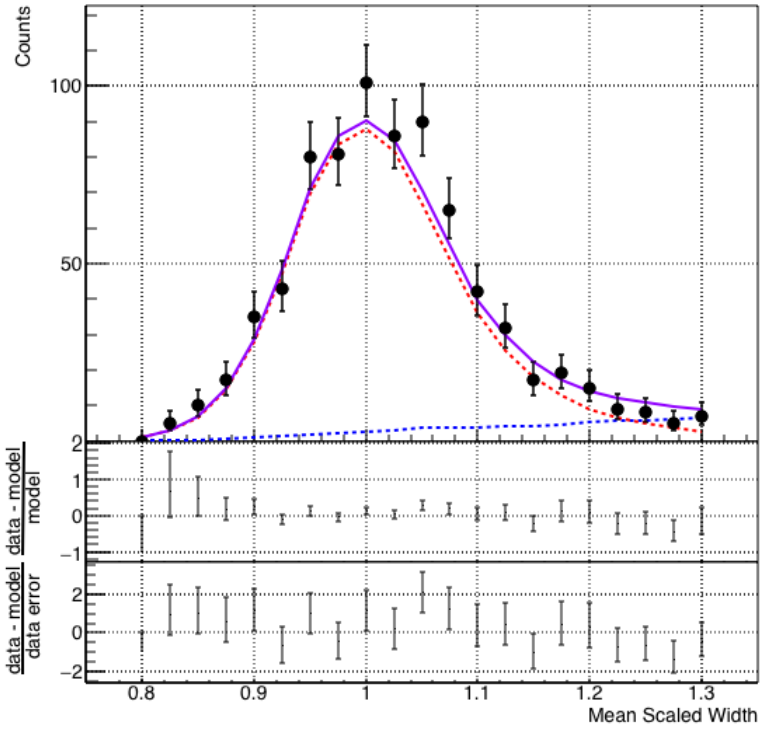

(b) Within 0.1° of source position

Figure 6.14: (*a*) MSW distribution for both the entire Mrk 501 field of view and (*b*) only events within 0.1° of the source position. Plotted are the data (black points), background model (blue dashed), source (red dashed), and full models (purple solid).

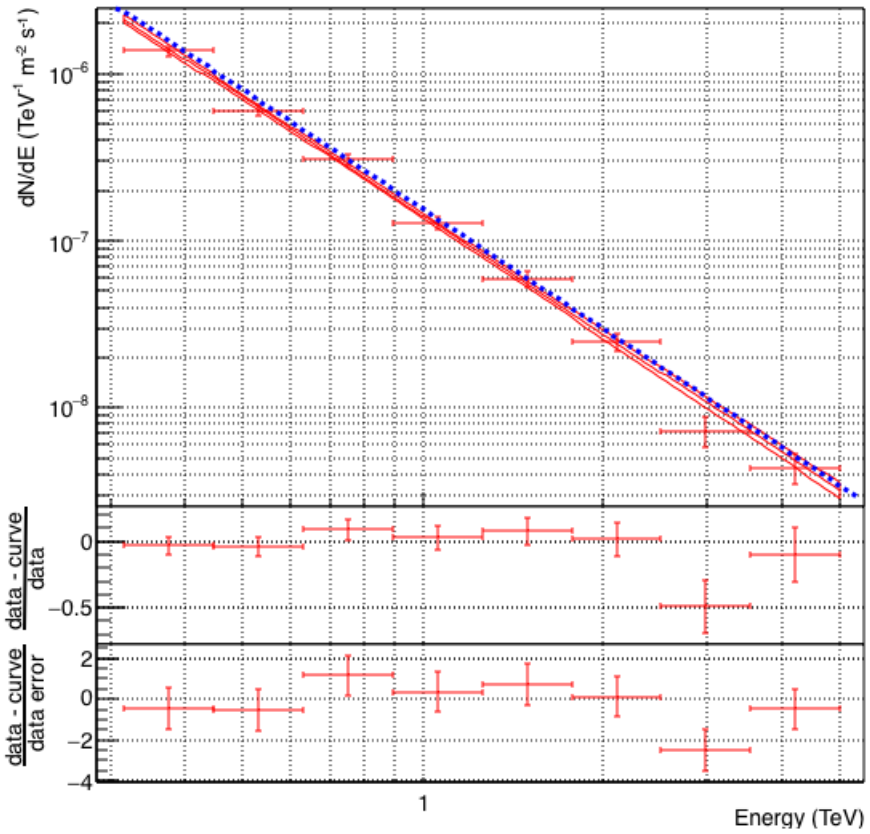

Figure 6.15: Best fit spectrum for Mrk 501. The best fit from the standard VEGAS analysis (blue dashed line) is also plotted.

6.3.3 1ES 1218+304

1ES 1218+304 (α=12h 21m 21.9s, δ=+30° 10' 37.2") and nearby 1ES 1215+303 (α=12h 17m 50.1s, δ=+30° 07' 0.6") are weak blazars with very soft spectra (Γ < -3.0). Data analyzed by the 3D MLM amounts to ∼48.6 hours. The initial analysis was done only fitting for 1ES 1218+304, however as can be seen in Fig. 6.16b 1ES 1215+303 is also visible as a small region of enhanced emission right of center. A subsequent analysis was also done simultaneously fitting for both point sources modeled as power laws according to Eq. 6.3. The results of this second analysis are reported here. The resulting spatial significance map and MSW residuals for this analysis are shown in Fig. 6.16 and Fig. 6.18 respectively.

For 1ES 1218+304 the best fit spectral values were found to be Γ=-3.54 (± 0.11) and f_0=1.01 (± 0.05) x 10^{-7} TeV^{-1} m^{-2} s^{-1} evaluated at E_0=0.5 TeV. For 1ES 1215+303 the fit values are Γ=-3.14 (± 0.43) and f_0=5.2 (± 1.2) x 10^{-9} TeV^{-1} m^{-2} s^{-1} evaluated at E_0=0.7 TeV. A plot of these spectra is provided in Fig. 6.15, along with the best fit spectrum for 1ES 1218+304 obtained from the standard VEGAS RBM analysis (blue dashed line). A direct comparison between the two analyses (see Table 6.1) shows that although the spectral parameters agree within errors, the values are still quite a bit different from each other. The agreement between these two analyses may be improved with better handling of the background model, as mentioned in §6.5.3.

Due to the weak nature of these sources, investigation of the spatial significance and excess maps reveals little information with which to evaluate the source models. Instead, the fit can be used as an evaluation of the background model. Looking at the MSW residuals between the model and data in the region surrounding 1ES 1218+304 (Fig. 6.18b), it is seen that in the immediate vicinity of the source the level of emission is well characterized by the combination of the source and background model. This is evidenced by the fact that the residuals mostly stay within ±2 standard deviations (bottom residual plot). The MSW residual plots for 1ES 1215+303 (Fig. 6.18c) show a similar level of agreement. The overall quality of the background can be evaluated in Fig. 6.18a. Here, the overall contribution from background appears to be slightly overestimated in the region where gamma-ray photons contribute significantly (∼0.9-1.1). This can lead to an underestimate of the overall source flux normalization (f_0). If the

level of this disagreement is energy dependent, the background can also have an influence on the spectral index (Γ). For bright sources, such as the Crab nebula and Mrk 501 above, the impact of the background will be reduced due to the larger number of source photons in the fit.

6.3.4 Comparison to RBM Analysis

As was mentioned above, the sources analyzed in this section have been studied using standard analysis techniques. To ensure a self consistent cross check with the standard analysis, a re-analysis of these sources was carried out using the standard VEGAS RBM analysis on the same data covering the same energy range of 316 GeV to 5.01 TeV. The spectra were derived using the standard reflected region analysis (RRM). In terms of the data used, the primary difference is in the cut range on MSW. The MSW range chosen for the standard analysis of [0.05, 1.1] is optimized for the highest gamma-ray sensitivity. The range chosen for the 3D MLM analysis of [0.8, 1.3] allows a better characterization of the background. The difference in the lower bound of the cut on MSW is negligible as very few events are reconstructed with a MSW below 0.8.

A comparison between the spectral fit values was also carried out using the reflected region model (RRM) analysis. The RBM significances and best fit RRM spectral parameters are presented in Table 6.1. The results demonstrate a good level of agreement between the two analyses for most parameters. Mrk 501 was analyzed with different scale energy (E_0) values as the 3D MLM is evaluated close to the analysis scale energy. Evaluating the 3D MLM derived Mrk 501 spectrum at 1 TeV results in a flux norm value of 1.42×10^{-7}, which agrees with the RRM result, within errors. The largest difference occurs for 1ES 1218+304, in which the 3D MLM index appears to deviate from the RRM index by about two standard deviations. This could be the result of a slight deficiency in the background model which would affect the weakest source more dramatically than the brighter Crab nebula and Mrk 501. Additionally, inaccuracies in the effective area and energy migration IRFs could also impact the modeling of the source spectrum. If discrepancies between these IRFs and the true distribution is not uniform across energy, this would also impact the measured index of the source.

[3] An extrapolation of the MLM f_0 to the same E_0 as the standard analysis is provided in the text.

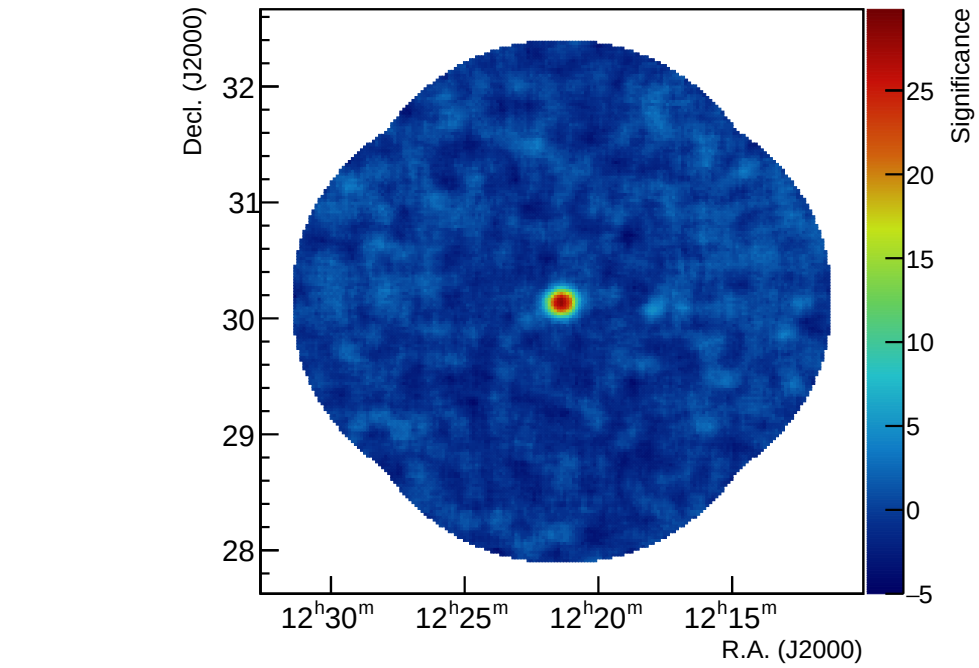

(a) Significance Map

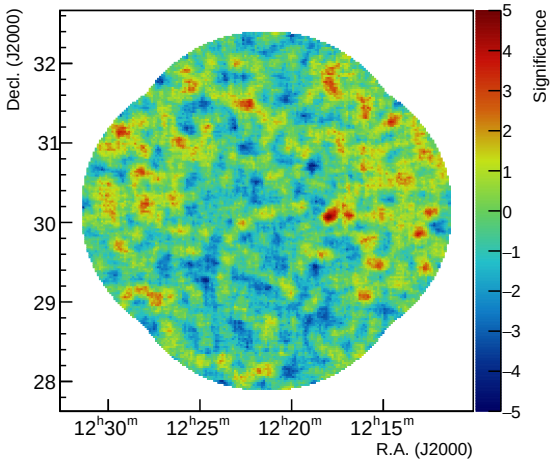

(b) 1ES 1218+304 Subtracted Significance Map

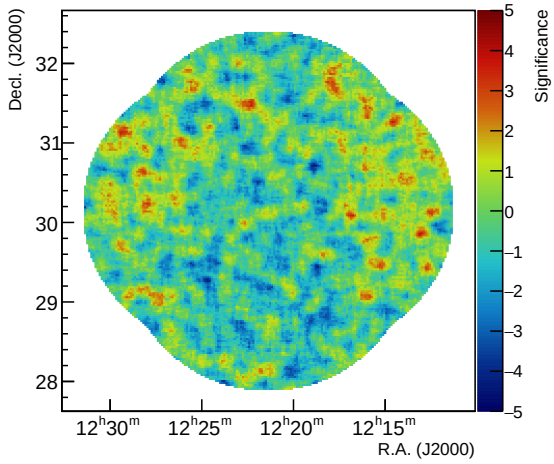

(c) All Sources Subtracted Significance Map

Figure 6.16: (*a*) Spatial significance map of 1ES 1218+304 computed without the Source model and (*b*) with the source model.

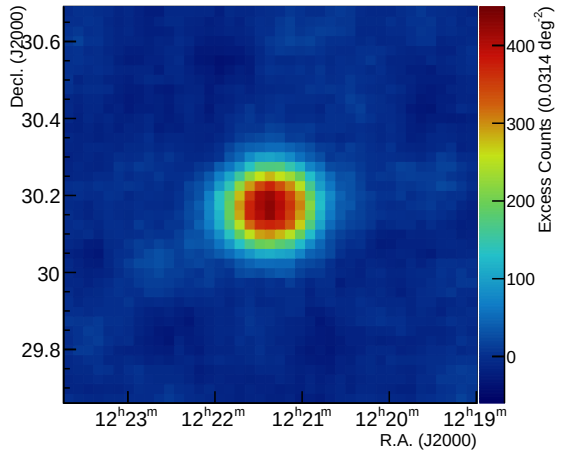

(a) 1ES 1218+304 Source Included

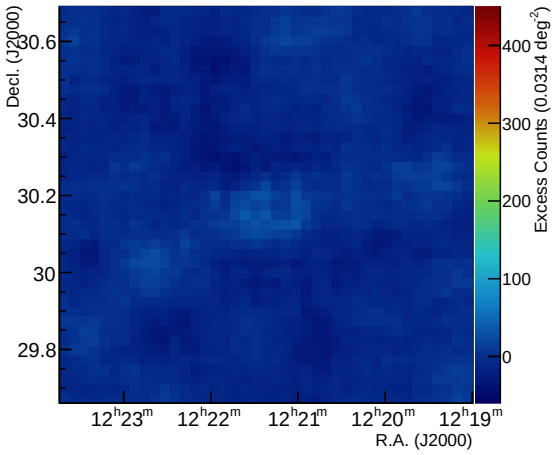

(b) 1ES 1218+304 Source Subtracted

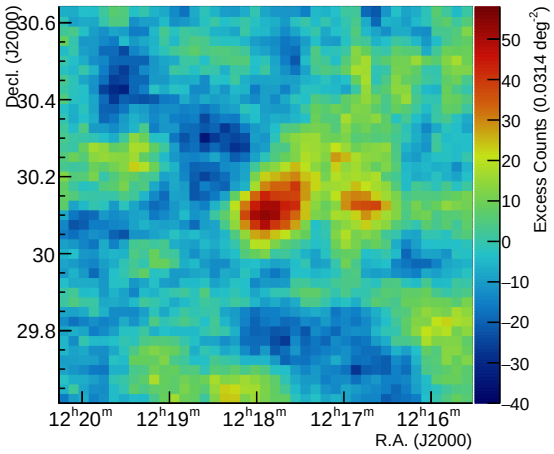

(c) 1ES 1215+303 Source Included

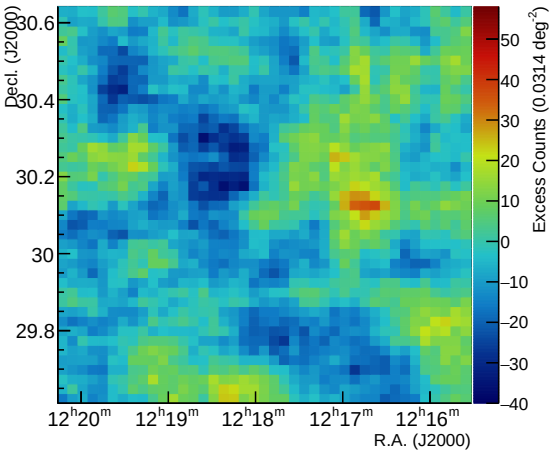

(d) 1ES 1215+303 Source Subtracted

Figure 6.17: Zoomed excess sky map of the region around the source position for (*top*) 1ES 1218+304 and (*bottom*) 1ES 1215+303 with (*right*) source included and (*left*) source subtracted. Features in the lower map highlight differences between the model and the data. The source subtracted maps have been placed on the same z-axis scale.

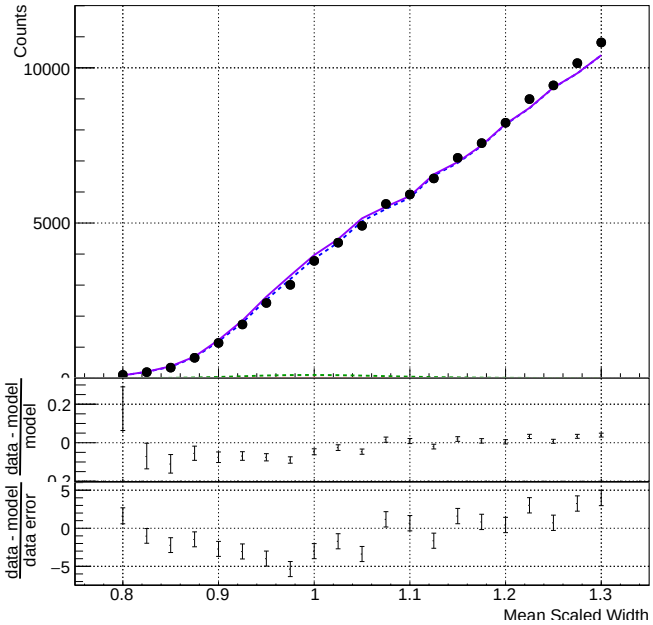

(a) Full Field MSW distribution

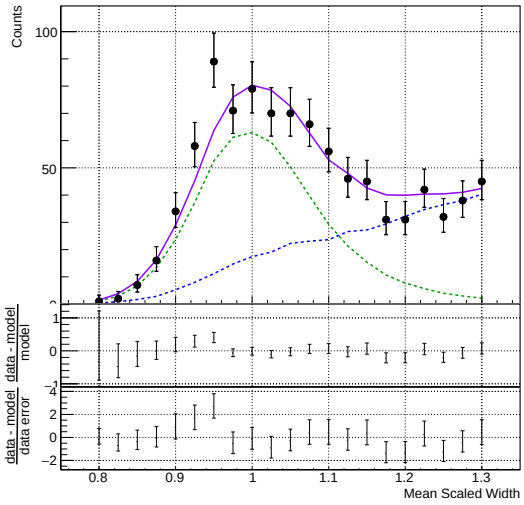

(b) Within 0.1° of 1ES 1218+304

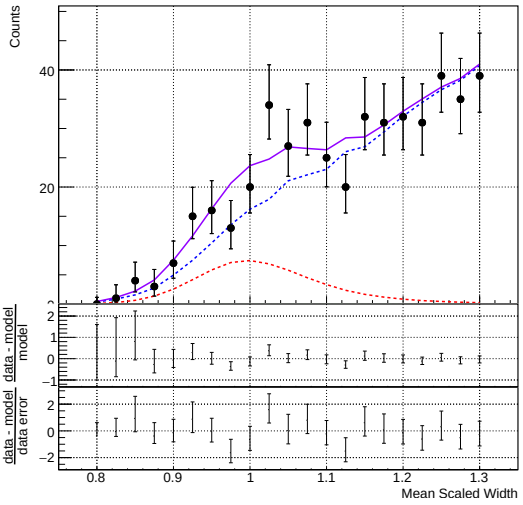

(c) Within 0.1° of 1ES 1215+303

Figure 6.18: MSW distributions for (a) the entire 1ES 1218+304 field of view, (b) only events within 0.1° of 1ES 1218+304, and (c) events within 0.1° of 1ES 1215+303. Plotted are the data (black points), background model (blue dashed), source (1ES 1215+303 in red, 1ES 1218+304 in green), and full models (purple solid).

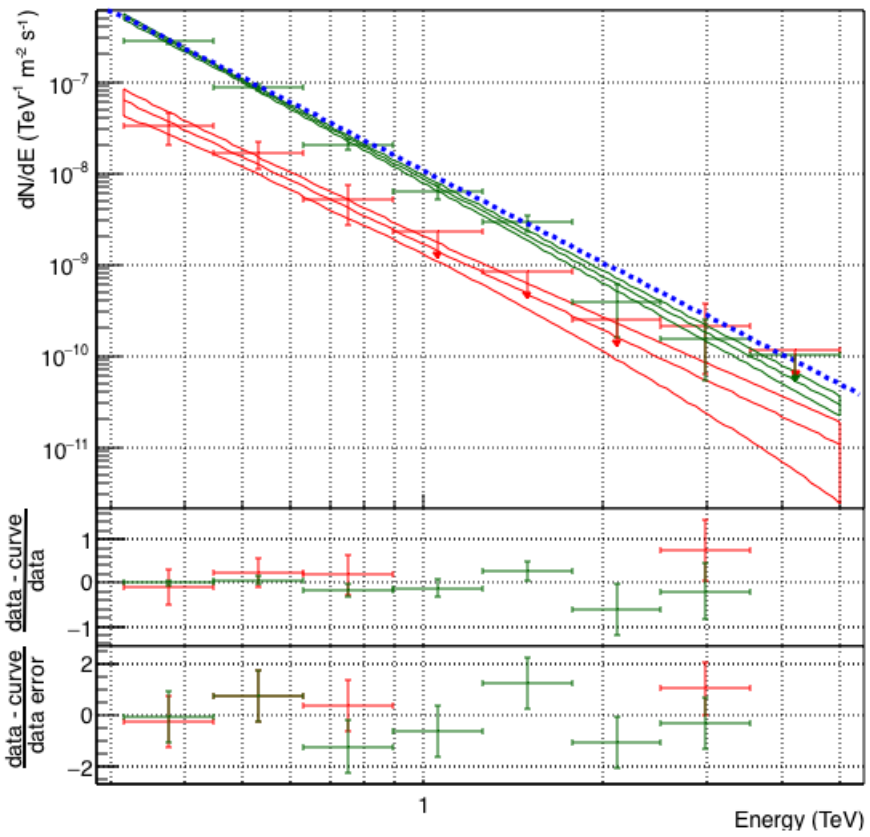

Figure 6.19: Best fit spectrum for 1ES 1218+304 (green) and 1ES 1215+303 (red). The best fit to 1ES 1218+304 from the standard VEGAS analysis is also plotted (blue dashed line). Upper limits are provided for bins where the source specific TS for that bin is < 4.

Table 6.1: Comparison of derived spectra for known point sources. σ represents either the significance of the RBM analysis or the $\sqrt{TS}$ for the MLM analysis. Spectral fits for the standard analysis use the reflected region model for background estimation. f_0 is given in units of (TeV^{-1} m^{-2} s^{-1}) and is evaluated at the scale energy E_0. p_1 represents either Γ for a powerlaw spectrum or α for a log-parabola. In the case of a log-parabola spectrum p_2 is the β parameter. Errors shown are statistical only.

Source	Method	σ	$f_0 \cdot 10^{-7}$	E_0	p_1	p_2
Crab	standard	187.3	4.05 ± 0.07	1 TeV	-2.44 ± 0.02	-0.15 ± 0.03
	MLM	253.9	3.85 ± 0.06	1 TeV	-2.47 ± 0.02	-0.13 ± 0.02
Mrk 501	standard	49.5	1.55 ± 0.07	1 TeV	-2.37 ± 0.06	-
	MLM[3]	65.6	2.79 ± 0.09	0.75 TeV	-2.35 ± 0.05	-
1ES 1218+304	standard	40.4	1.10 ± 0.06	0.5 TeV	-3.35 ± 0.12	-
	MLM	34.5	1.01 ± 0.05	0.5 TeV	-3.54 ± 0.11	-

6.4 Known Extended Source

6.4.1 IC443

Since the primary goal of the 3D MLM is to assist in detecting energy dependent morphology in extended sources, it is beneficial to test the analysis on a known extended source. For reasons which were discussed in §4.3.3, VERITAS has not detected any sources with extensions above a few tenths of a degree in size. IC443, which has been extensively studied with standard VERITAS analyses (results in preparation), is the most extended source available for test studies. It has a notably non-uniform shape which has been observed in both the VERITAS and *Fermi*-LAT data (see color map in Fig. 6.20).

IC443 was analyzed with the 3D MLM. This analysis seeks to answer the question of whether the 3D MLM can discern between different models of source emission from a source. This will be absolutely necessary when evaluating spatially extended sources such as Geminga in which the morphology of the emission is important. Of particular interest is the ability to distinguish the energy dependence of the emission regions. To test this ability, several source template fits were attempted to a sample of the VERITAS data. This included a 0.15° disk to the brightest region of emission (Fig. 6.20, black circle) and a 0.35° disk to the entire remnant (Fig. 6.20, white circle). A comparison of these two independent model fits provides an insight to whether the 3D MLM can distinguish between the two emission models.

For the 3D MLM cross-check on IC443, a power law spectrum, according to Eq. 6.3, was used for both fits. The data sample used amounted to ∼38.7 hours. The results for the spectral fits are given in Table 6.2. The spectrum derived for the 0.15° disk centered at the brightest position in the map is shown in Fig. 6.23a. The additional dashed lines represent the standard analysis fit to the whole remnant (blue) and the brightest region (green). The reason that the flux normalization from the standard analysis is lower is most likely due to the differences in how the flux of the source is measured. In the standard analysis there is no accounting for emission which originates from inside the region but is reconstructed outside the region due to the instrument's spatial resolution. However, the 3D MLM includes the smearing of the intrinsic disk model by the PSF and thus is able to better account for this effect. The estimated flux is not as high as the whole remnant due to the limited size of the 0.15° disk. However,

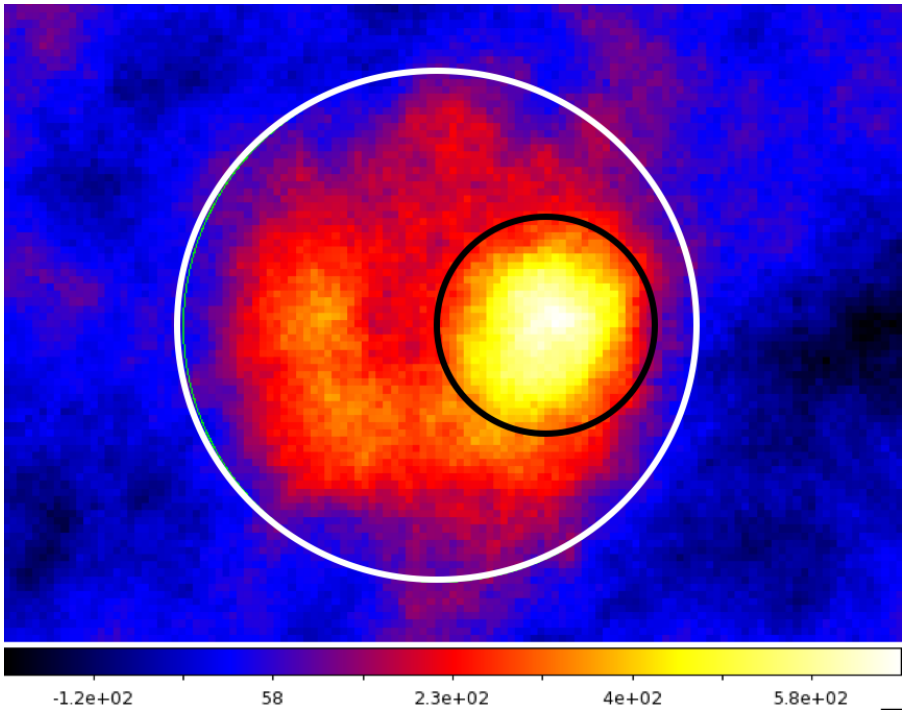

Figure 6.20: Excess counts map of IC443 produced from the standard VEGAS RBM analysis. Circles represent the extensions of attempted disk model fits of 0.15° (black) 0.35° (white) to the highest emission region and whole remnant respectively.

Table 6.2: 3D MLM results for the two models fit to IC443. f_0 is evaluated at 0.65 TeV.

Extension (°)	TS	$f_0 \times 10^{-8}$	Γ
0.15	147.3	2.42 ± 0.25	-3.01 ± 0.17
0.35	173.5	4.79 ± 0.41	-2.89 ± 0.14

because the 0.35° disk model covers the entire remnant it has a much better agreement with the standard analysis (see Fig. 6.23b).

The 3D MLM residual maps shown in Fig. 6.21 provide another assessment of how the two disk models compare. Fig. 6.21c shows the spatial significance map including the fitted 0.15° disk model. While the emission from the bright region appears well accounted for, the residual remaining emission from the remnant is clearly visible as an excess arc about 0.1° to the East of the image center. Fig. 6.21d shows the resulting spatial significance map including the fitted 0.35° disk model. Here, the bulk of the emission from the remnant appears to be accounted for with a slight underestimate of the source flux near the brightest region of the remnant. There also appears to be a slight excess present in the Northeast portion of the maps. Wether this is due to an inconsistency in the background model or whether it is actually due to an undetected source (or sources) of emission is unclear at this time and warrants future study.

6.5 Blank Field Data Sets

There exists in any analysis the danger of falsely detecting emission from a source where none exists. Because of this, the proposed 3D MLM was tested against two fields assumed to contain no detectable signature of gamma-ray emission. Since the emission in these fields is assumed to come strictly from the background, any positive source detection would also suggest a deficiency in the modeling of the background.

6.5.1 Blank Field Analysis Overview

Ursa Minor and Segue 1 have been studied as potential regions containing emission from dark matter annihilation (Acciari et al., 2010; Aliu et al., 2012). However, no significant emission has been detected from these sources in the VERITAS data. This makes the Ursa

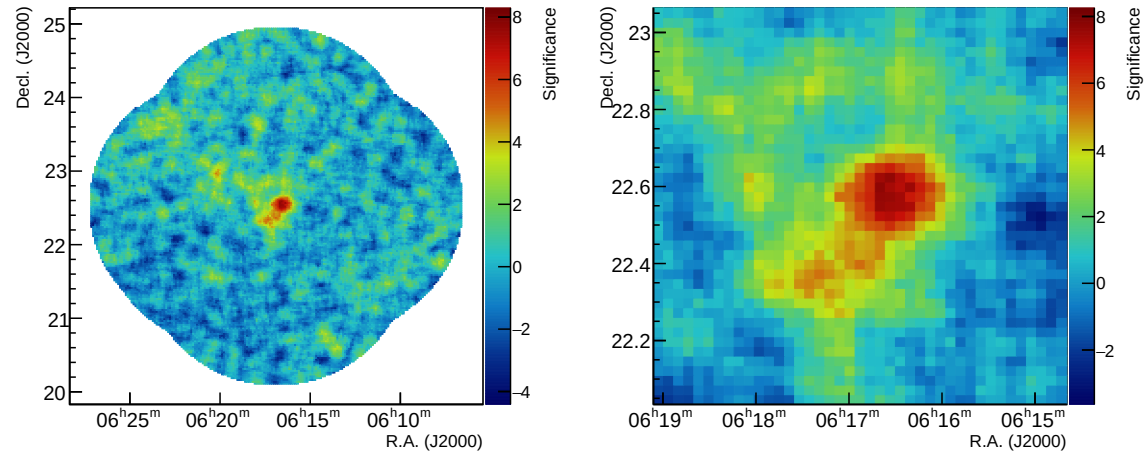

(a) Significance Map

(b) Zoomed Significance Map

(c) 0.15° Disk Subtracted Significance Map

(d) 0.35° Disk Subtracted Significance Map

Figure 6.21: (*a*) Spatial significance map of IC443 computed without the Source model. (*b*) Significance map showing 1°×1° around IC443. The second row shows the spatial significance map including (*c*) the 0.15° disk model and (*d*) 0.35° disk model.

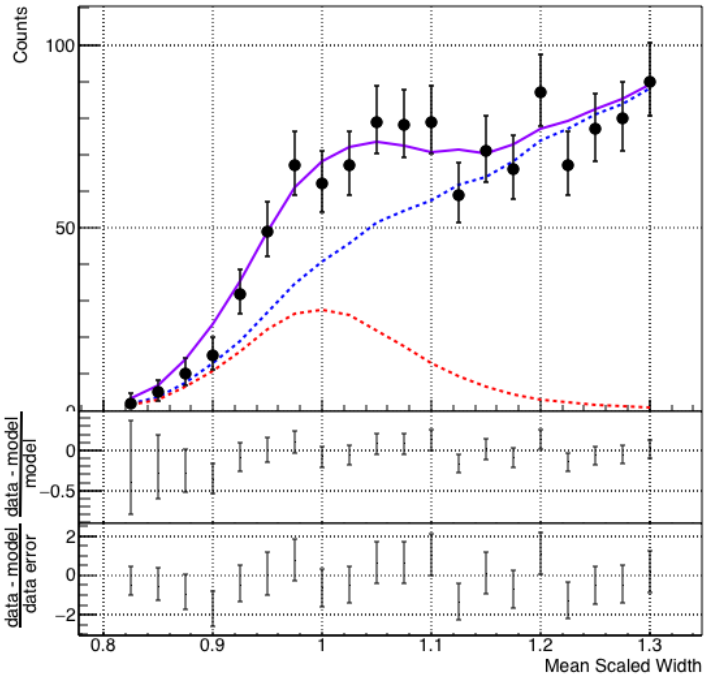

(a) Within the bounds of the 0.15° disk

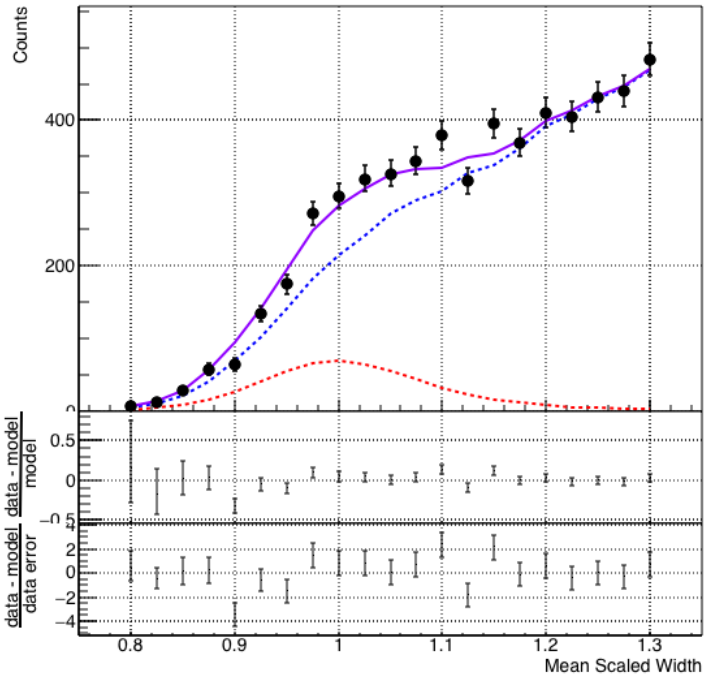

(b) Within the bounds of the 0.35° disk

Figure 6.22: Projections of the IC443 MSW models and data within the bounds of the (a) 0.15° disk and (b) 0.35° disk.

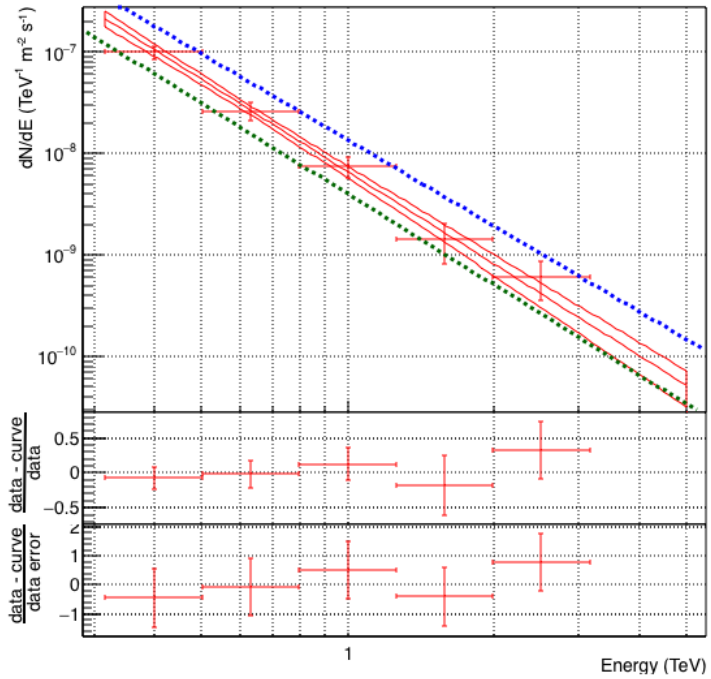

(a) 0.15° disk spectrum

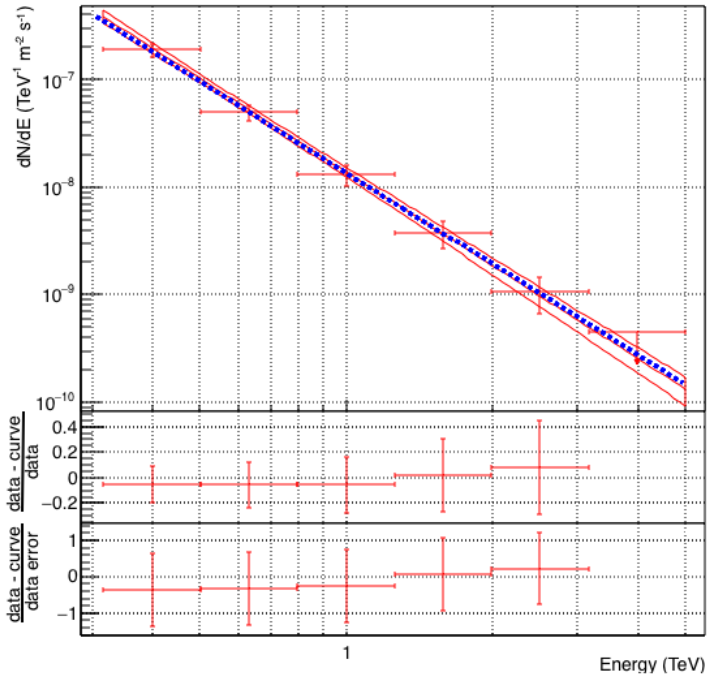

(b) 0.35° disk spectrum

Figure 6.23: Best fit spectra for the MLM analysis of IC443 using a 0.15° radius disk (*left*) and 0.35° radius disk. The best fit to the whole remnant from the standard VEGAS analysis is plotted as a blue dashed line. The green dashed line represents the best fit spectrum to the region around the brightest emission.

Table 6.3: Results of extended source analyses on Segue 1. Source was modeled as a disk with radius equal to the value in the *Extension* column. f_0 and f_0' have units of TeV^{-1} m^{-2} s^{-1} and are evaluated at 0.5 TeV. The unprimed values were fit using MSW models derived using the same Segue 1 data. Primed values were fit using MSW models excluding the same Segue 1 data. Results for the point source analysis are also included for comparison.

Extension (°)	TS	$f_0 \times 10^{-7}$	Γ	TS'	f_0'$\times 10^{-7}$	Γ'
0.0	2.49	0.003 ± 0.003	-1.0 ± 2.0	10.1	0.004 ± 0.003	-1.00 ± 0.64
0.1	7.68	0.008 ± 0.008	-1.1 ± 2.2	17.2	0.010 ± 0.008	-1.07 ± 0.56
0.3	2.04	0.02 ± 0.61	-1.56 ± 1.8	13.6	0.07 ± 0.62	-2.0 ± 2.0
0.5	1.18	0.0 ± 1.8	-2.1 ± 1.8	16.1	0.2 ± 1.2	-2.4 ± 1.6
1.0	2.04	0.3 ± 4.9	-2.9 ± 2.2	34.2	0.90 ± 0.23	-2.75 ± 0.30
1.5	1.47	0.43 ± 0.45	-3.19 ± 0.91	54.5	2.25 ± 0.41	-2.80 ± 0.21
2.0	1.77	0.72 ± 0.78	-3.00 ± 0.89	78.6	4.09 ± 0.64	-2.70 ± 0.17

Minor and Segue 1 datasets good candidates for blank field studies with the VERITAS array. In addition to testing accidental detection of a point source, several extended source models were also tried. Templates were generated for sources modeled as a disk with radii of 0.1°, 0.3°, 0.5°, 1.0°, 1.5°, and 2.0°.

In this section, ∼39.8 hours of Segue 1 data and ∼16.5 hours of Ursa Minor data were studied. The data were analyzed using two different sets of response functions. The first includes data being analyzed in the parameterization of the background acceptance and MSW models. This *ideal* analysis represents the case in which the model is a near perfect match to the data under investigation. The second set of IRFs are generated excluding data samples taken on Ursa Minor and Segue 1. Instead, the IRFs are derived from a sample of data from other sources taken at similar zenith and azimuth angles as the data under investigation. This *realistic* analysis represents a more realistic situation in which no data taken on the source being analyzed would be used in the characterization of the expected background models.

6.5.2 Blank Field Results

The results of these fits to Segue 1 and Ursa Minor are presented in Table 6.3 and Table 6.4 respectively. The ideal analyses (unprimed results in these tables) result in[4] TS values < 10, which is consistent with no source being present in the data. The associated flux normalizations

[4]Recall that a TS > 25 is required to consider a detection.

Table 6.4: Results of extended source analyses on Ursa Minor. Source was modeled as a disk with radius equal to the value in the *Extension* column. f_0 and f_0' have units of TeV^{-1} m^{-2} s^{-1} and are evaluated at 0.5 TeV. The unprimed values were fit using MSW models derived using the same Ursa Minor data. Primed values were fit using MSW models excluding the same Ursa Minor data. Results for the point source analysis are also included for comparison.

Extension (°)	TS	$f_0 \times 10^{-7}$	Γ	TS'	f_0'$\times 10^{-7}$	Γ'
0.0	0.43	0.02 ± 3.5	-2.4 ± 1.9	8.58	0.10 ± 0.057	-2.42 ± 0.54
0.1	0.67	0.03 ± 2.5	-2.1 ± 2.5	9.91	0.10 ± 0.058	-2.18 ± 0.46
0.3	0.0016	0.0 ± 0.03	-3.7 ± 1.6	7.54	0.1 ± 1.6	-2.1 ± 1.6
0.5	0.0016	0.0 ± 0.18	-2.5 ± 2.1	12.0	0.4 ± 2.2	-2.3 ± 1.8
1.0	0.0018	0.0 ± 1.0	-3.2 ± 1.0	39.1	1.9 ± 0.47	-2.51 ± 0.25
1.5	1.60	1.0 ± 0.8	-4.0 ± 2.2	131.4	7.1 ± 1.0	-2.54 ± 0.16
2.0	2.69	2.0 ± 1.4	-4.0 ± 2.2	173.0	12.2 ± 1.6	-2.46 ± 0.13

are also each consistent with 0. Ursa Minor shows the same result, with exception of the two largest disk model extensions. However, even for these analyses the derived TS value is still $<$ 3.

In the case of the pure analysis (primed values in Table 6.3 and Table 6.4), the resulting TS values appear to increase with increasing source size. There are two situations which could cause this increasing TS value. The first is that there is actually a source present in the data. Since the TS values are increasing with increasing source size, this would suggest that if a source were present it would be at least as large as the largest source model. This fact would seem to be supported by the fact that the flux normalization (f_0') also increases with increasing source size. If such an extended source existed, then the smaller sources would only be able to pickup a small portion of the emission, resulting in a lower estimate of f_0'.

The second situation which could lead to the observed increase in TS values and f_0' is an incorrect modeling of the background. This is supported by the fact that both Segue 1 and Ursa Minor show the same apparent rise in both TS and f_0', suggestive of a more pathological cause. This hypothesis is further confirmed by looking at the MSW residuals for the largest model fits with the largest TS values for Segue 1 (Fig. 6.25d) and Ursa Minor (Fig. 6.27d). The residuals in these plots reveal an over subtraction in the dominant gamma-ray MSW region (0.9 - 1.1). Comparing the 2° analysis for the ideal and realistic cases, the largest deviation in the ideal case is ∼2 standard deviations, however in the realistic case the largest deviation

is ∼5 standard deviations. This notable discrepancy between the model and the data suggests that an incorrect background model is the most probable cause for the large TS values.

6.5.3 Addressing Background Discrepancies

Having established that a discrepancy in the modeling of the MSW background can affect the analyses of weak and highly extended sources, this section highlights a few possibilities for improving these models.

One improvement involves a better handling of the zenith angle dependence of the MSW distribution. Currently the background models are derived from data within narrow bins of zenith angle. As a result, the MSW distribution for a given model actually represents the distribution derived from a range of zenith angles. Currently, no correction is applied to account for difference in the distribution of zenith angles in the data used to derive the MSW distribution within a given zenith bin compared to the data being analyzed.

The most obvious way to improve the handling of the zenith angle dependence is to interpolate the appropriate distribution from the data derived distributions. This would be a challenge as any individual 20 minute data sample contributes sparsely to a single zenith angle. A distribution interpolated between any two such sparsely populated distributions would be poorly defined and have large errors associated with each bin. Because of this, any interpolation method that is implemented would have to incorporate multiple distributions from several different zenith angles.

Another improvement involves better handling of the nuisance parameters in the background MSW models. As mentioned in §5.3.3, there is a limit placed on the threshold for which a bin in the background MSW distribution is replaced with a nuisance parameter. That threshold is set to a value of two in each of the above analyses. Ideally this threshold would be set such that every bin in the model is replaced by a nuisance parameter, however this was found to destabilize the fit and increase the convergence time dramatically. This is mainly due to the thousands of added free parameters in the fit. Improvements to this aspect of the model would have to reduce the number of nuisance parameters in the fit, or handle the large number of parameters in a more efficient way[5].

[5]See, for example, the proposed changes to how the nuisance parameters are handled presented in §8.2.2.

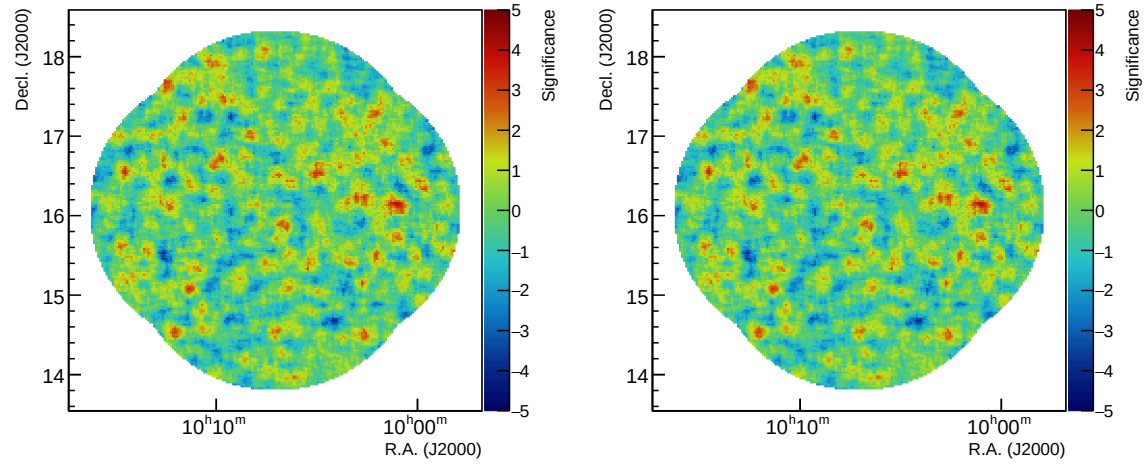

(a) Ideal Analysis Point Source

(b) Ideal Analysis 2° Disk

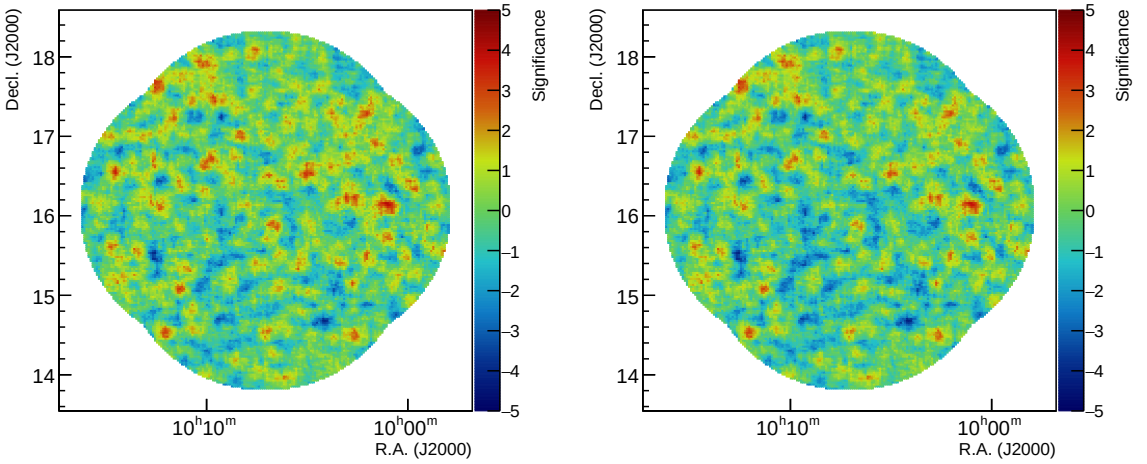

(c) Realistic Analysis Point Source

(d) Realistic Analysis 2° Disk

Figure 6.24: Segue 1 spatial significance maps. The rows identify (*top*) ideal analysis (*bottom*) realistic analysis. The columns identify (*left*) point source and (*right*) 2° disk models.

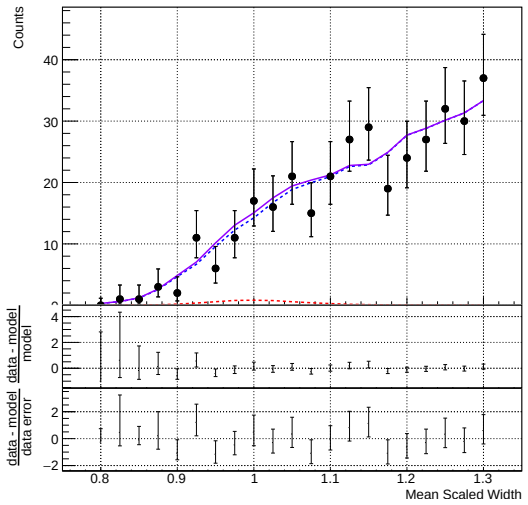

(a) Ideal Analysis, Within 0.1° of Source

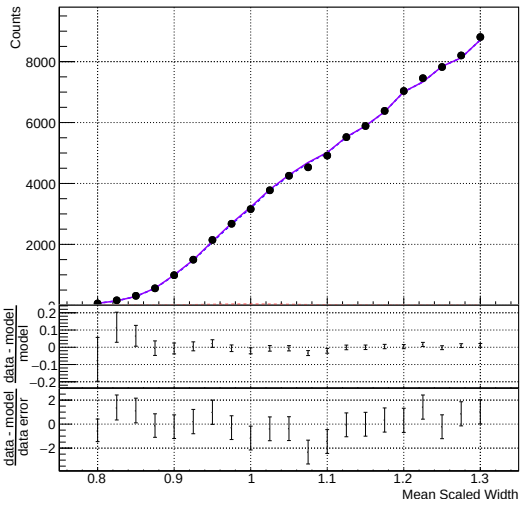

(b) Ideal Analysis, Full Field of View

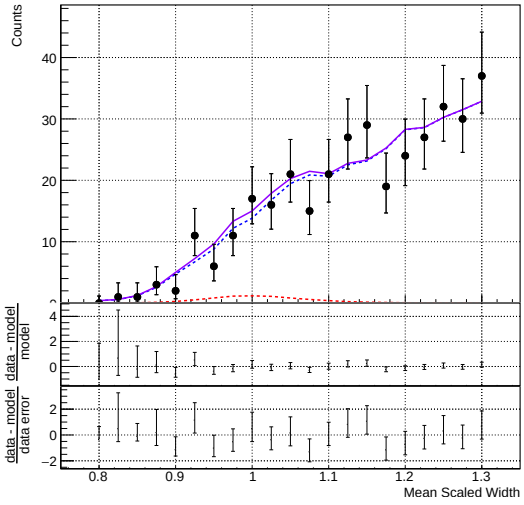

(c) Realistic Analysis, Within 0.1° of Source

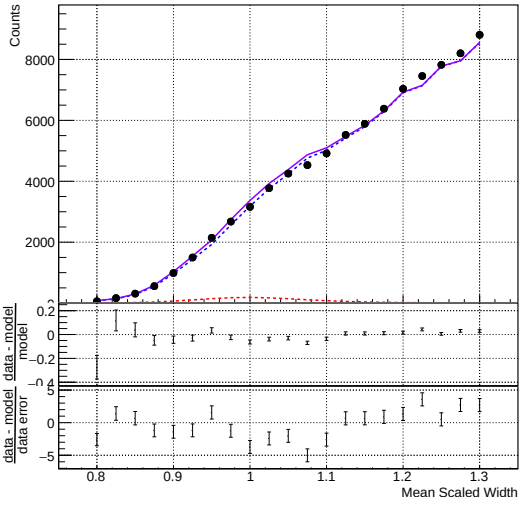

(d) Realistic Analysis, Full Field of View

Figure 6.25: Segue 1 MSW residual plots. The rows identify (*top*) ideal analysis (*bottom*) realistic analysis. The columns identify events within (*left*) 0.1° of the source position for the point source model and (*right*) the complete field of view for the 2° source model.

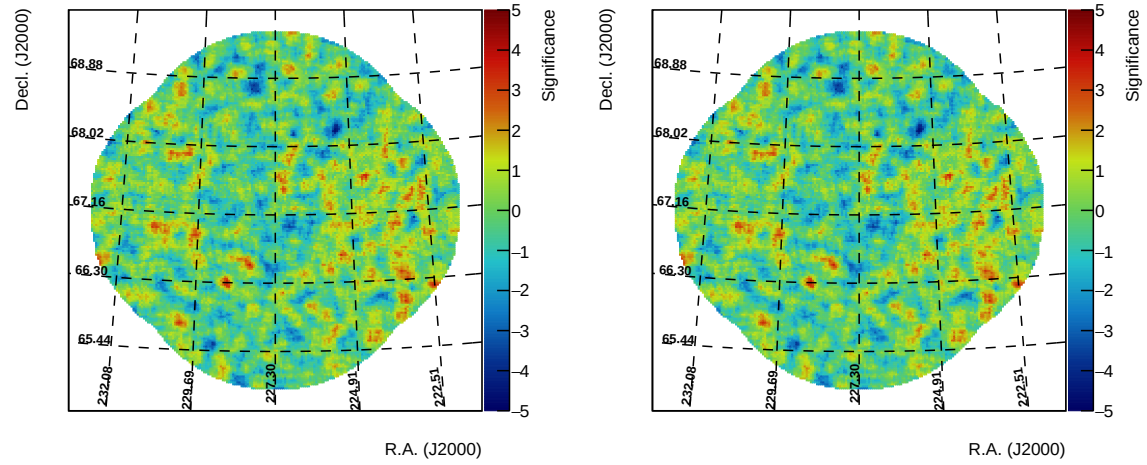

(a) Ideal Analysis Point Source

(b) Ideal Analysis 2° Disk

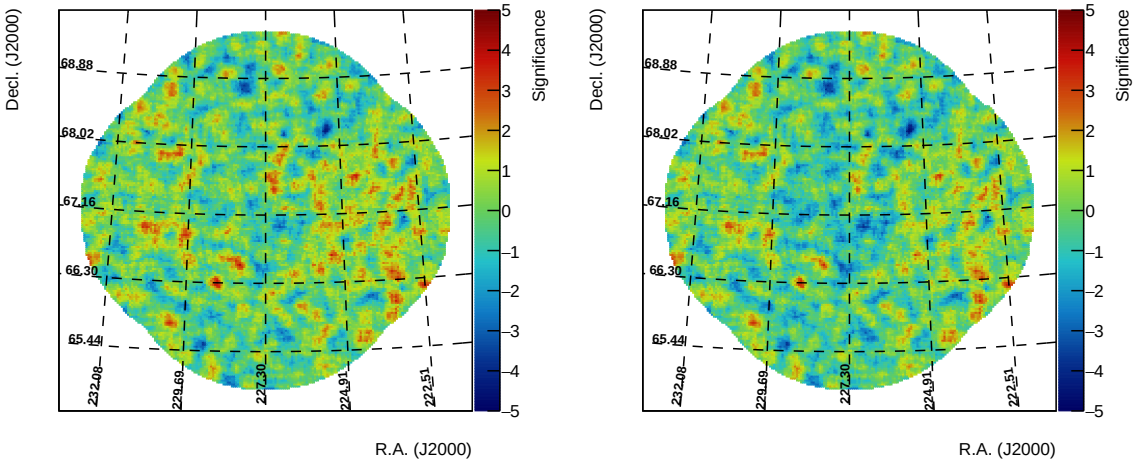

(c) Realistic Analysis Point Source

(d) Realistic Analysis 2° Disk

Figure 6.26: Ursa Minor spatial significance maps. The rows identify (*top*) ideal analysis (*bottom*) realistic analysis. The columns identify ($left$) point source and ($right$) 2° disk models.

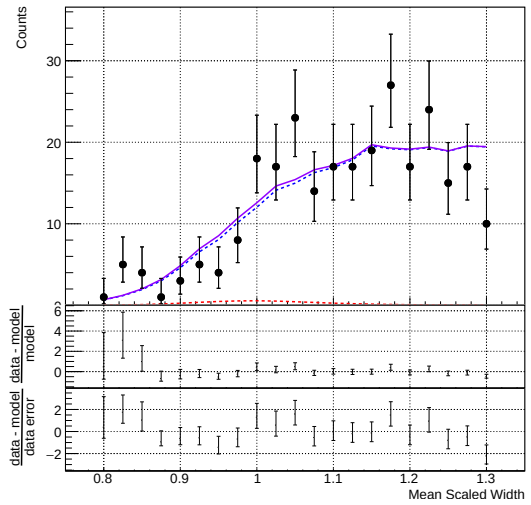

(a) Ideal Analysis, Within 0.1° of Source

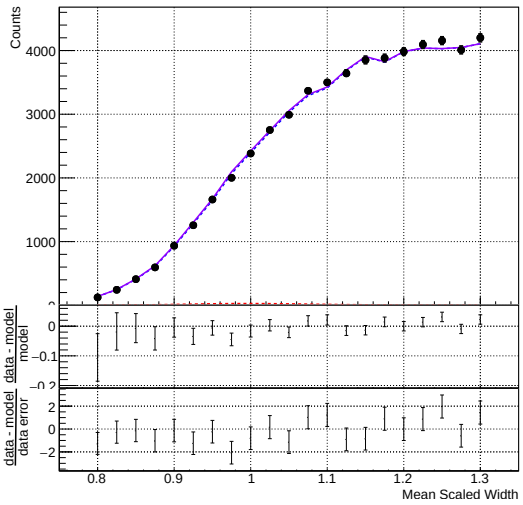

(b) Ideal Analysis, Full Field of View

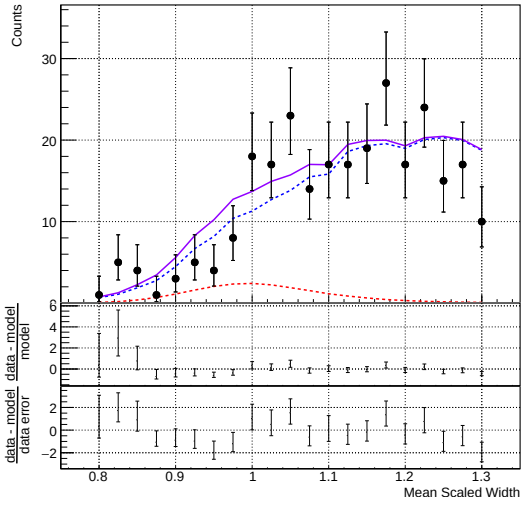

(c) Realistic Analysis, Within 0.1° of Source

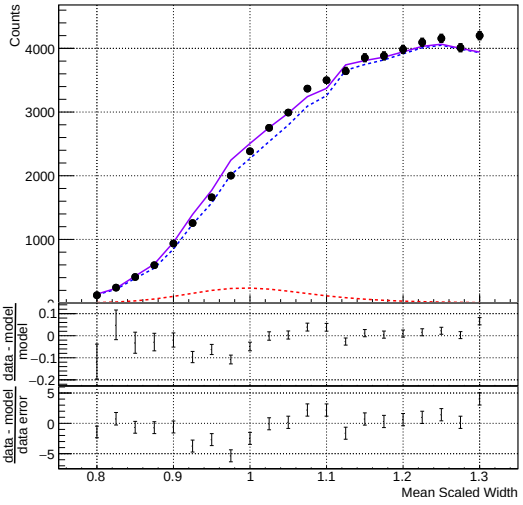

(d) Realistic Analysis, Full Field of View

Figure 6.27: Ursa Minor MSW residual plots. The rows identify (*top*) ideal analysis (*bottom*) realistic analysis. The columns identify events within (*left*) 0.1° of the source position for the point source model and (*right*) the complete field of view for the 2° source model.

CHAPTER 7. SYSTEMATIC UNCERTAINTIES

So far the focus of the discussion on the 3D MLM has been on the results obtained from models which are presumed to be perfect representations of the source and background as observed by VERITAS in the fits[1]. These models, however, are not without error themselves. More specifically the parts of the VERITAS response (effective area, energy resolution, PSF, MSW distributions, etc...) have some uncertainty associated with the values derived from the simulations or background data. The errors in these instrument response functions contribute to the overall *systematic* uncertainty of the fit spectral parameters and even the source extension.

7.1 Universal sources of Systematic Uncertainty

7.1.1 Energy Scale Uncertainty

The dominant uncertainty in the VERITAS spectral analysis comes from the uncertainty in the amount of Cherenkov light emitted in an air-shower. This directly affects the accuracy in the energy estimate of a given photon-like event, known as the *energy scale*. Hardware components contributing to the energy uncertainty include the reflectivity and alignment of the telescope mirrors, the efficiency of the camera PMTs and light cones, the gain of the individual PMTs, and the accuracy of the PMT pulse shapes used in the simulations of the PMT response. Estimates of atmospheric properties are another significant source of uncertainty. Uncertainty in the amount of Cherenkov light produced by a shower and the level of extinction in the atmosphere can play a significant role in the estimation of the energy of an observed event. Each of these hardware and atmospheric effects contributes up to 10% (many below 5%) to the uncertainty in the energy estimate[2]. By adding the uncertainties in quadrature, the overall

[1] This is not strictly true as the nuisance parameters accommodate some level of uncertainty in the MSW distributions.

[2] The contributions to the overall uncertainty from the hardware and atmosphere are comparable in size.

estimate of the uncertainty on the energy scale can be as high as ∼20%. The uncertainty can double when considering data taken at large zenith angles. This is related to the airmass a particle shower must traverse which scales as 1/cos(zenith). The uncertainty in the energy estimate will approximately scale in the same manner (Archer et al., 2014).

The effect of the energy scale uncertainty has a direct impact on the observed flux of a source. Consider some spectrum which is derived using a scale energy shifted by some fraction, represented by ϵ. The reconstructed (measured) energy of an event is now $E_{rec} = E_{true} \times (1+\epsilon)$, where E_{true} is the true energy of the event. Applying this correction to the spectral function of a power law

$$\begin{aligned} \frac{dN}{dE_{rec}} &= \frac{dN}{dE} \cdot \frac{dE}{dE_{rec}} \\ &= f_0 \left(\frac{E_{rec}}{1+\epsilon} \right)^{\Gamma} \frac{1}{1+\epsilon} \end{aligned}$$

gives rise to the following representation of the spectrum as a function of the scale energy

$$\frac{dN}{dE_{rec}} = (1+\epsilon)^{-\Gamma-1} f_0 \left(E_{rec}\right)^{\Gamma} \tag{7.1}$$

yielding an ∼30% error in the differential flux for an energy scale uncertainty of 20% and an index of Γ=-2.5.

The influence on the observed integral flux (N) can be computed in a similar way.

$$\begin{aligned} N(E) &= \int f_0 E^{\Gamma} dE \\ N(E) &= \frac{f_0}{\Gamma+1} E^{\Gamma+1} \end{aligned}$$

Which gives

$$\frac{\sigma_N}{N} = |(\Gamma+1)\epsilon| \tag{7.2}$$

for the error on the observed integral flux. It can be seen from Eq. 7.2 that a 20% overestimate of the energy scale for a spectrum with $\Gamma = -2.5$ yields an overestimate of the integral flux by ∼30%. This ranges from ∼20% for a hard spectrum with $\Gamma = -2.0$ up to ∼50% for a soft spectrum of $\Gamma = -3.5$. This demonstrates the importance of an accurate estimator of the energy, as the uncertainty in the energy scale typically dominates the systematic error in estimate of the source flux.

The uncertainty of 20% represents a worst case scenario. In reality uncertainties from the different hardware components and the atmosphere are often assumed to be uncorrelated, leading to a smaller systematic uncertainty on the observed flux. This assumption is typically employed except in cases where the correlations between uncertainties is well understood.

7.1.2 Effective Area

Another source of uncertainty relevant to both the RBM and the 3D MLM is the effective area. The value for this uncertainty comes from two components. The first component is a statistical uncertainty based on the number of events observed in simulations of gamma-ray air-showers. Recall from Eq. 5.6 that the effective area is given by

$$A = A_{thrown}\frac{N_{observed}}{N_{simulated}}$$

The statistical uncertainty comes from $N_{observed}$. Assuming Poisson statistics in the number of observed events provides an estimate of the error on the effective area.

$$\sigma_A \approx \frac{A_{thrown}}{N_{simulated}}\sqrt{N_{observed}} \tag{7.3}$$

The second component comes from cuts applied to the simulations on various parameters (MSW, MSL, squared offset over which the events are integrated, etc...), which are typically optimized for a given source strength. The overall effect from adjusting these parameters is typically $\lesssim$10%, implying that the energy scale uncertainty will still be the dominant source of uncertainty.

It has also been mentioned previously that the background acceptance changes as a function of the zenith angle across the field of view. Since the effective area also exhibits a zenith angle dependence, it is possible that the signal acceptance will also change across the field of view, introducing another potential source of systematic uncertainty. This work did not investigate this source of uncertainty, however future studies will need to be carried out which investigate this effect. If it is discovered that the effective area changes significantly over a single field of view, this could have implications on the way in which the datasets are combined within the bands of zenith. A large dependence on zenith angle would result in the need for a greater number of zenith angle bins.

Table 7.1: Resulting spectral fits to the Crab nebula data in §6.3.1 with the standard PSF model and after scaling the PSF sigma width by ±10%.

σ Scale Factor	TS	$f_0 \cdot 10^{-7}$	α	β
-10%	64352.4	3.78 ± 0.06	-2.47 ± 0.02	-0.14 ± 0.02
0.0%	64452.6	3.85 ± 0.06	-2.47 ± 0.02	-0.13 ± 0.02
+10%	64261.4	3.91 ± 0.06	-2.47 ± 0.02	-0.13 ± 0.02

7.2 Understanding Systematic Uncertainty in the 3D MLM

7.2.1 Point Spread Function

The effect of an error on the width of the PSF can affect the derived spectral values. Using the Crab nebula data set in §6.3.1 as an example, the analysis can be run with a narrower PSF sigma (see Fig. 7.1). By comparing the spectral parameters derived using the narrower (broader) PSF to the parameters from the standard analysis, it is possible to see how an uncertainty in the PSF parameters contributes to the overall systematic uncertainty of the fitted spectral parameters. Table 7.1 shows a comparison of the resulting spectral parameters in the fit. The main difference between the derived spectra is the flux normalization (f_0). There appears to be a slight correlation between f_0 and the width of the sigma parameter.

As mentioned in §5.2.2.4, the PSF model is based on a King function with a fixed value for λ. The best value of λ was chosen to be the value which maximizes the TS value when fit to the same sample of Mrk 501 as described in §6.3.2. However, these fits can also be used to demonstrate the effect of changing λ on the fitted spectral parameters. The resulting significance maps from three models of the PSF (λ=2.5, 5.0, 7.5) fit to the Crab nebula data sample from §6.3.1 are presented in Fig. 7.2. The derived spectral parameters for each of these models are presented in Table 7.2. The flux normalization appears to have a slight anti-correlation with an increase in the PSF λ parameter, although the results from these analyses are still consistent within errors.

Using the spectral parameter values presented in Table 7.1 and Table 7.2, the affect of the incorrect PSF on the measured flux normalization is a mis-estimate of ∼1%-2%. Therefore, an incorrect measurement of the PSF σ and λ parameters has a far reduced impact on the measured source flux than the uncertainty in the energy scale. The fits for other spectral

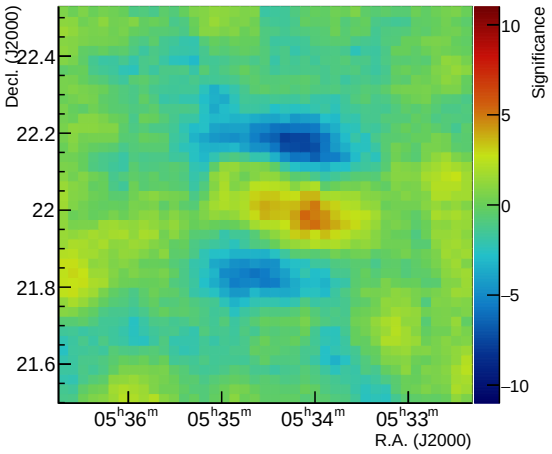

(a) Unscaled PSF model

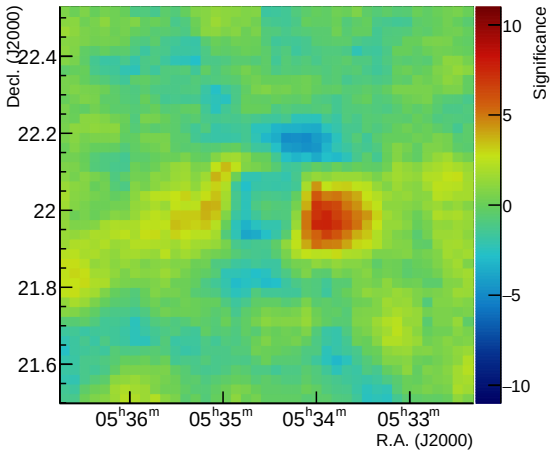

(b) -10% Sigma PSF

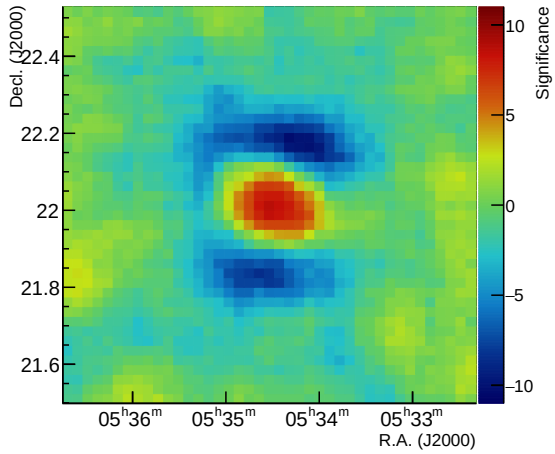

(c) +10% Sigma PSF

Figure 7.1: Significance sky maps of the Crab data (*a*) using the standard, unscaled PSF model, (*b*) reducing the PSF sigma parameter by 10%, and (*c*) increasing the PSF sigma parameter by 10%.

Table 7.2: Resulting spectral fits to the Crab data in §6.3.1 using PSF models derived with a fixed value of λ from 2.5 to 7.5.

λ	TS	$f_0 \cdot 10^{-7}$	α	β
2.5	64452.6	3.85 ± 0.06	-2.47 ± 0.02	-0.13 ± 0.02
5.0	63930.8	3.81 ± 0.06	-2.47 ± 0.02	-0.14 ± 0.02
7.5	63449.7	3.80 ± 0.06	-2.47 ± 0.02	-0.14 ± 0.02

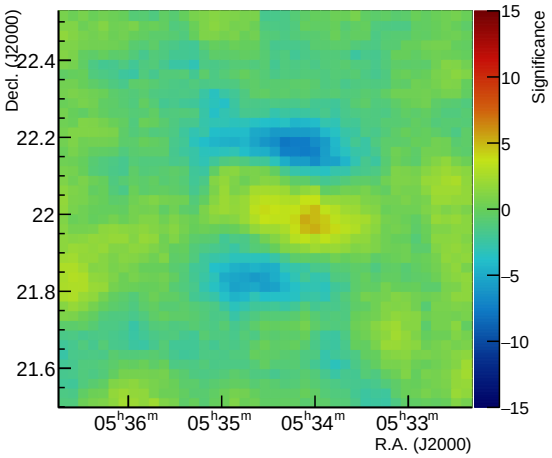

(a) $\lambda_{PSF} = 2.5$

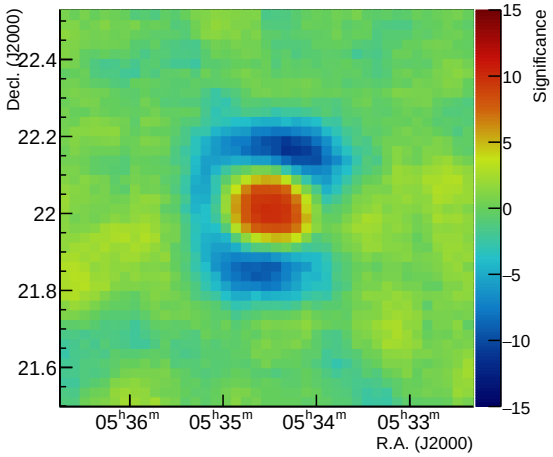

(b) $\lambda_{PSF} = 5.0$

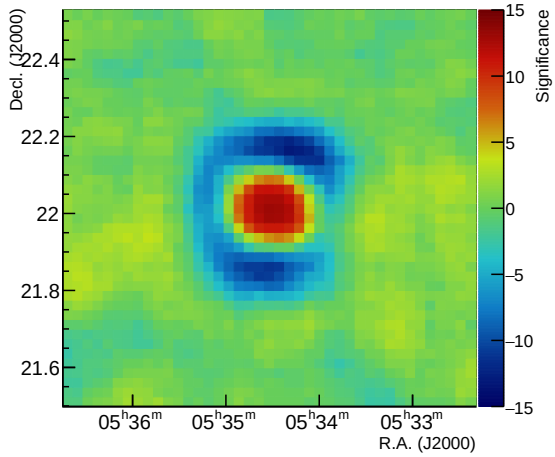

(c) $\lambda_{PSF} = 7.5$

Figure 7.2: Sky maps of the Crab nebula data using PSF models derived with (*a*) λ=2.5 (standard model), (*b*) λ=5.0, and (*c*) λ=7.5. Z-axis represents the number of standard deviations above the prediction from the background model component.

parameters (α, β) appear to be fairly robust to minor changes in the PSF parameterization.

This argument can be reversed in order to assess the effect of an accurate parameterization of the PSF to a source with an extension below the detection threshold. In this case the PSF model would be slightly narrower than the source being studied. It can be reasonably assumed that the spectral parameters derived for such a source should still be reasonably unchanged compared to those derived using the correct source extension.

7.2.1.1 Measured Source Extension

There is another affect that an uncertainty in the PSF will have in analyses of extended sources. This is the uncertainty on the measurement of the intrinsic source extension. For this discussion, a $\pm 10\%$ uncertainty on the relevant PSF parameter will be assumed.

To begin this discussion, assume the most general situation in which the source being studied has a morphology consistent with a Gaussian distribution, and that the PSF can be modeled as a Gaussian as well.

$$\begin{aligned} f_{src}(r) &= \frac{1}{\sigma_{src}\sqrt{2\pi}} e^{-r^2/(2\sigma_{src}^2)} \\ g_{psf}(r) &= \frac{1}{\sigma_{psf}\sqrt{2\pi}} e^{-r^2/(2\sigma_{psf}^2)} \end{aligned} \tag{7.4}$$

In order to generate the actual model of the source it is necessary to convolve the source model and the PSF model. This is relatively simple for the case here, as the convolution of two Gaussian functions is itself a Gaussian function

$$(f * g)(r) = \frac{1}{\sqrt{\sigma_{src}^2 + \sigma_{psf}^2}\sqrt{2\pi}} e^{-r^2/(2(\sigma_{src}^2+\sigma_{psf}^2))} \tag{7.5}$$

Increasing σ_{psf} by some fractional amount ϵ will obviously change the width of the distribution[3]. For this simple case an analytic expression which relates the width of the convolved source model Gaussian in the ideal case with the width of the Gaussian that would be measured with an incorrect PSF width.

$$\begin{aligned} \sigma_{src,meas}^2 + \sigma_{psf}^2 &= \sigma_{src,true}^2 + (1+\epsilon)^2\sigma_{psf}^2 \\ \sigma_{src,meas} &= \sqrt{\sigma_{src,true}^2 + \sigma_{psf}^2(\epsilon^2 + 2\epsilon)} \end{aligned} \tag{7.6}$$

[3]Here, ϵ represents a fractional increase, i.e. ϵ=0.1 means a +10% increase in sigma.

σ_{psf} represents the derived PSF model, and $(\epsilon+1)\sigma_{psf}$ represents the true width of the Gaussian PSF. Now the difference between the measured Gaussian width and the true Gaussian width can be determined.

$$\Delta\sigma_{src} = \sigma_{src,meas} - \sigma_{src,true} = \sqrt{\sigma^2_{src,true} + \sigma^2_{psf}(\epsilon^2 + 2\epsilon)} - \sigma_{src,true} \tag{7.7}$$

In the extreme cases of this formula

$$\Delta\sigma_{src} = \begin{cases} \sigma_{psf}\sqrt{\epsilon^2+\epsilon}, & \text{if } \sigma_{src,true} << \sigma_{psf} \text{ (i.e. point source)} \\ 0, & \text{if } \sigma_{src,true} >> \sigma_{psf} \text{ (i.e. highly extended source)} \end{cases} \tag{7.8}$$

As mentioned previously, the 3D MLM does not use a Gaussian to model the PSF, but rather uses a King function. Still, the above argument provides insight to the behavior of the fitted source extension uncertainty. Eq. 7.7 demonstrates how the measured source extension is less affected by an uncertainty in the PSF width at larger source extensions.

To understand the effect of an uncertainty in the PSF width on the measured source extension, the following simple exercise is used. This involves modifying the PSF width by some amount and deriving a model from the modified PSF convolved with some source of known extension. This model is then fit with the standard PSF convolved with a source of similar extension $\pm\epsilon$, where ϵ represents a slight increase or decrease in extension. In the study presented here, a $\pm$10% modification to the PSF sigma parameters was used to approximate an uncertainty in the PSF model. It is not expected that the PSF deviates from the derived widths by more than 10%.

The results of these studies are presented in Table 7.3. From the results, two conclusions can be made. The first is that underestimating the PSF sigma value leads to an overestimate in the source width, a result that is intuitive. The second is that larger sources are less affected by an error in the width of the PSF. Eq. 7.7 predicts this result, as is also shown in Table 7.3. Overall, the uncertainty on the measured extension of large sources will most likely be dominated by statistical fluctuations in the emission across spatial extent of the source.

7.2.2 Energy Resolution and Effective Area

The energy resolution is the spread in measured energy for a sample of events with the same true energy. For the relevant energy range used in the above analyses the uncertainty on

Table 7.3: Systematic uncertainty on the best fit source extension assuming the true PSF sigma is larger (+10%) or smaller (-10%) than the standard PSF sigma. The values based on Eq. 7.7 assume a Gaussian PSF with σ=0.07°.

	Eq. 7.7		King ∗ Gaus		King ∗ Disk	
Ext. (degrees)	-10%	+10%	-10%	+10%	-10%	+10%
0.1	-0.0048	0.0050	-0.0026	0.0027	-0.0053	0.0055
0.3	-0.0016	0.0017	-0.0015	0.0009	-0.0036	0.0026
0.5	-0.0009	0.0010	-0.0010	0.0004	-0.0030	0.0024
1.0	-0.0005	0.0005	-0.0006	0.0002	-0.0026	0.0019
1.5	-0.0003	0.0003	-0.0003	0.0002	-0.0021	0.0019
2.0	-0.0002	0.0003	-0.00005	0.0003	-0.0015	0.0015

Table 7.4: Systematic uncertainty on the best fit source extension assuming the true PSF sigma is larger (+) or smaller (-) than the standard PSF sigma. The values based on Eq. 7.7 assume a Gaussian PSF with σ=0.07°.

	Eq. 7.7		King ∗ Gaus		King ∗ Disk	
Ext. (degrees)	-10%	+10%	-10%	+10%	-10%	+10%
0.1	-4.8%	5.0%	-2.6%	2.7%	-5.3%	5.5%
0.3	-0.52%	0.57%	-0.49%	0.29%	-1.2%	0.86%
0.5	-0.19%	0.21%	-0.21%	0.081%	-0.61%	0.49%
1.0	-0.047%	0.051%	-0.058%	0.015%	-0.26%	0.19%
1.5	-0.021%	0.023%	-0.022%	0.011%	-0.14%	0.12%
2.0	-0.017%	0.013%	-0.003%	0.016%	-0.076%	0.076%

the estimate of the energy is of the order 15%-20%. This uncertainty is accounted for in the models used in the 3D MLM fit. This means that the effect of the energy resolution is already be factored into the fits.

The effective area is handled slightly differently in the 3D MLM as compared to the RBM analysis. Rather than integrating the counts observed within a certain distance of the assumed source position (as is done in the RBM), the MLM counts all of the events which fall into the observed field of view. This will reduce the uncertainty originating in the choice of the integration radius. However, since this uncertainty is typically small (less than a few percent) the benefit derived from not integrating within a small region is relatively minor. The 3D MLM will still have similar uncertainties in the effective area from the from errors in the computed MSW and MSL parameters.

In order to measure the effect of these uncertainties on the fit spectral parameters, a simple adjustment of the values input to the source model can be made. For example, the affect of the effective area can be computed by noting the shift in the spectral parameters by adjusting the input values from the effective area up and down by one standard deviation. Additionally, the uncertainties from varying the cuts can be determined by deriving the effective area IRF from simulations with adjusted cut ranges on the MSW and MSL parameters. The resulting systematic uncertainty on parameter p_i from the effective area is given by

$$\sigma_{i,A} = p_{i,adjusted} - p_{i,standard}. \tag{7.9}$$

By adjusting the values individually, their independent affect on the fit spectral parameters can be evaluated. An approximation of the overall systematic uncertainty can then be made by adding all of the individual uncertainties in quadrature.

$$\sigma^2_{i,sys} = \sigma^2_{i,A} + \sigma^2_{i,R} + \sigma^2_{i,P} + ... \tag{7.10}$$

A positive one standard deviation shift in the IRF values may have a different affect on the spectral parameters as compared to a negative one standard deviation shift. Because of this, the above prescription can be used to separately assess the positive and negative systematic uncertainties for each spectral parameter.

7.2.3 Mean Scaled Width

Assessing the impact of an error in the MSW model on the overall source uncertainty is difficult. The contribution to the uncertainty comes from two main factors.

1. Assumed Poisson fluctuations based on the total number of events observed from a given bin.

2. Differences in the distribution of observation parameters for data sets used to derive IRFs and data sets being fit.

For the source models the relative uncertainty from (1) above is very small due to the large number of events simulated. The contribution to the uncertainty from (2) is also reduced due to the fact that distributions are *scaled* by the value estimated from simulated gamma-ray events. This means that the gamma-ray distribution of events in MSW will be fairly similar for events taken around the positions simulated. For example, the peak of each distribution should always occur at or around zero. The width of the distribution is presumed to be a secondary effect and to change very little within a given bin of zenith angle, azimuth, and offset. All of this leads to the conclusion that the uncertainty incurred from the MSW distributions is dominated by the background component.

In terms of background models, to a small degree the uncertainty from (1) is accounted for through the inclusion of nuisance parameters in the bins derived from the fewest events. The nuisance parameters allow the actual value for the expected number of events in a bin of MSW to be adjusted within some presumed Poisson statistical fluctuation on the observed number of events. The uncertainty derived from the remaining bins which are not modeled as nuisance parameters is not accounted for. In these bins the derived distribution is assumed to be the correct one. Ideally the threshold for modeling a bin with a nuisance parameter would be set sufficiently high that the uncertainty in any remaining bin would be negligible. Unfortunately as mentioned above this is not possible in the current state of the analysis.

The background models will also suffer from the second type of uncertainty above. Differences in observing positions and observing conditions for the datasets used to derive the distributions compared to the datasets being fit to is most likely the larger source of uncer-

tainty as compared to bin-by-bin statistical fluctuations. This is especially true for observations with very long exposures.

A combination of these uncertainties is the most probable source of the error in the blank field extended source tests shown in §6.5.2. As such, these studies can be used as a way to assess the level of uncertainty incurred from such observational mismatches. This discussion will focus on the most highly extended sources ($> 1^\circ$ radius) as the sources below this extension do not pass the TS > 25 detection threshold.

The Ursa Minor analysis is more strongly impacted by these sources of uncertainty as compared to the Segue 1 analysis. This assumption is based on the higher TS values and larger flux normalization derived for the Ursa Minor extended sources as compared to the corresponding Segue 1 analyses[4]. This will provide a loose upper limit to the MSW uncertainty based on (1) and (2) above.

The use of this information is shown in Fig. 7.3. Taking the best fit spectral parameters and their errors from Table 6.4, an upper limit is computed using the butterfly uncertainty formula for a power-law from Eq. D.4. For simplicity the correlation term between the flux normalization and the spectral index is ignored. Also plotted are log-parabola spectral curves representing 100%, 10%, and 1% the Crab nebula strength. It is clear any source that is presumed to be less than 10% of the Crab nebula and greater than 1° is most likely outside the capabilities of the analysis.

The sources discussed in Chapter 2 are sources of large extent. Both Geminga and 2FHL J0431.2+5553e are predicted to have extensions of $\sim 1.3^\circ$. The implication of the above study is that if these sources are less than $\sim$30% the strength of the Crab nebula around 1 TeV, then the new technique will be unable to claim a detection of these sources, even if a significant TS value is derived for them. Sources of even larger extent are most likely beyond the capabilities of the 3D MLM without some method of accounting for the differences between the observing parameters and statistical uncertainties in the derived MSW models. Resolving this issue is currently the focus of continued efforts on this analysis.

[4]This argument becomes stronger when noting that the Segue 1 data has more than twice the exposure ($\sim$39.8 hours) compared to the Ursa Minor data ($\sim$16.5 hours). Any impact on the spectral parameters due to the difference between the data and model would only become stronger with an increase in the exposure.

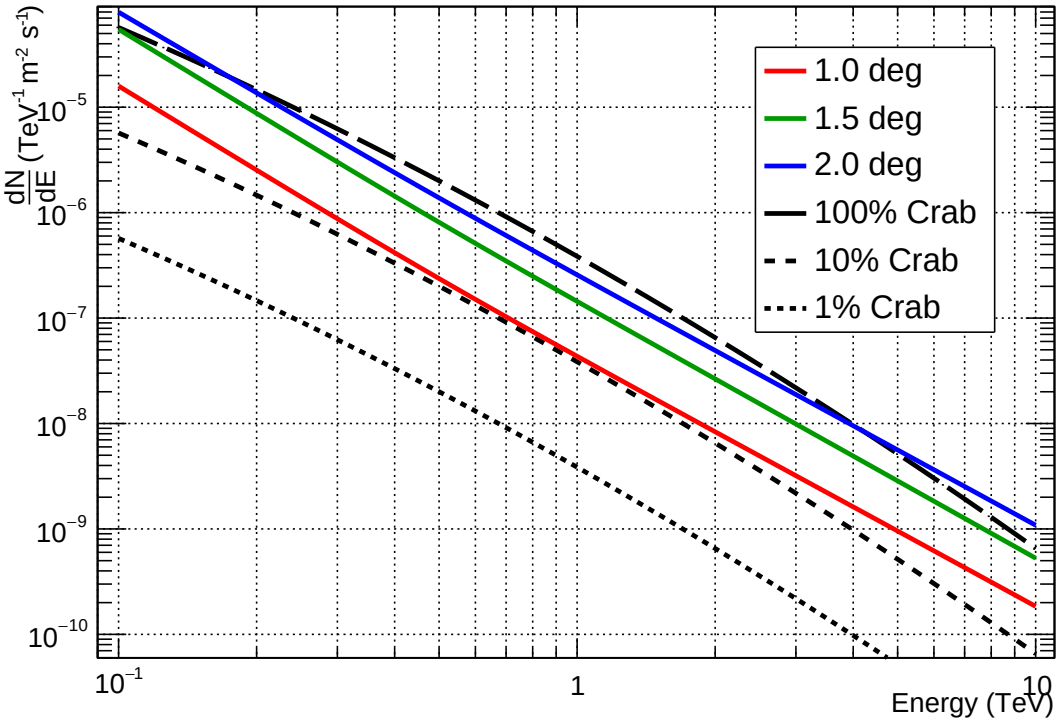

Figure 7.3: Estimates of the upper limit on the differential flux for extended sources based on the results from the blank field extended source cross checks on Ursa Minor. Also plotted are the spectral curves for a 100%, 10%, and 1% Crab nebula strength source in black.

CHAPTER 8. SUMMARY AND DISCUSSION

8.1 Overview

This thesis has presented an analysis which applies the technique of maximum likelihood in order to detect moderately extended ($\gtrsim$0.3° in radius) sources of gamma-ray emission in VERITAS data. It has been shown in §6.1.2 that when the distributions of the cosmic-ray background are well-determined the technique is able to accurately account for the emission from such a source. Even for sources which are highly extended ($\gtrsim$1.0° in radius) the technique is able to account for the emission whereas the standard RBM technique exhibits poor performance. Despite this, analysis of real data has revealed some areas where the technique is deficient. These areas will now be discussed along with potential areas of future improvement to resolve them.

8.2 Model Quality Assessment

8.2.1 Source Models

The point source analyses in §6.3 of the Crab nebula and Mrk 501 are useful for testing the modeling of the source and how well the 3D MLM is capable of accounting for the detected emission in the field of view. The main issue with the source model appears to be the observed asymmetry in the spatial residual maps. This asymmetry is visible in residuals for both the Crab Nebula (Fig. 6.9b) and Mrk 501 (Fig. 6.13b) about 0.17° above and below the source position which exhibit an over estimation of the source emission and thus a deficit of counts.

As mentioned in §5.2.2.4 the gamma-ray PSF is forced to be symmetric. However, it is possible to derive an asymmetric PSF by fitting a different width parameter to the simulations of gamma-ray air-showers. The above data suggest that an asymmetric PSF is preferred,

however the asymmetry does not appear to be radial. Rather, it appears the PSF has different extensions in the East-West direction as compared to the North-South direction.

This presents a problem as the air-shower simulations used in the fitting of the PSF all assume the observation is taken at offsets North of the source position. This makes deriving the dependence of the PSF shape on wobble *direction* very difficult without some initial insight as to how the shape should change in each direction. It is possible that future air-shower simulations could be generated taking into account each wobble direction, but care will need to be taken when modeling extended sources. Because extended sources do not strictly contain emission along the North-South and East-West directions, it will be important to accurately model how the PSF changes in (for example) the North-West direction.

Regardless of the apparent asymmetry of the PSF as a function of offset, the ability of the 3D MLM to accurately account for emission from a these point sources appears to agree well with spectral parameters derived from the standard reflected region analysis. This is demonstrated by the good agreement between the derived spectral parameters for the Crab nebula and Mrk 501 presented in Table 6.1 as well as the moderately extended source IC443.This is further demonstrated by the large reduction in excess counts when accounting for the emission from the fitted source in Fig. 6.9 and Fig. 6.13. The above asymmetry will most likely be of less consequence in models of highly extended sources due to their diffuse nature.

8.2.2 Background Models

The test analysis of the dwarf spheroidal galaxies Segue 1 and Ursa Minor provide a look at the modeling of the background emission. Beginning with the spatial background models, a perfectly matched model would result in a completely flat (all bins are zero) residual map. However, due to random Poisson fluctuations in the data there will always be some positive and negative excesses above and below the assumed background level in parts of the observed sky. The distribution of how significant these fluctuations are in each bin should be roughly Gaussian with standard deviation of 1.0. The quality of the background spatial models, though not perfect, does appear in every case to reproduce a Gaussian with width < 1.1.

Looking now at the MSW distributions for these background models. Specifically, Fig.

6.25d for Segue 1 and Fig. 6.27d for Ursa Minor. These show a large discrepancy around five standard deviations between the model and the data around the peak gamma-ray region of MSW, between 0.9 - 1.1. While it cannot be ruled out that there is some emission from these sources in the data, this large discrepancy does suggest that there is an issue in the modeling of the background. In the corresponding ideal models represented by 6.25b for Segue 1 and 6.27b for Ursa Minor no such discrepancy is observed. This is especially compelling as these models are derived excluding any events within 0.3° of the assumed source position. This means that any emission from a potential point source (or the inner region of an extended source) would not contaminate the models of the background and should be detectable by the analysis.

An additional improvement currently under development involves better handling of the nuisance parameters. Barlow and Beeston (1993), from which the current implementation of the nuisance parameters was derived, also outline how to approach the inclusion of these parameters without requiring simultaneous adjustment of both the spectral parameters and the nuisance parameters. Instead, an iterative approach is used in which the spectral parameters are first fit assuming the nuisance values are fixed. Then, a system of coupled equations are solved yielding updated values for the nuisance parameters. This process of fitting spectral parameters then updating the nuisance variables is iterated on until the change in the fitted spectral parameters is within some acceptable tolerance. Since the nuisance parameters are no longer adjusted simultaneously with the spectral parameters, care will need to be taken to ensure the errors on the MSW distributions are incorporated into the error of the spectral parameters.

8.2.3 Systematic Uncertainties

The uncertainties introduced by the 3D MLM technique can be described in relation to the two model components. The modeling of the source appears to introduce little additional systematic uncertainty in the estimation of the source parameters. The dominant uncertainty in a given source spectrum is the uncertainty in the energy scale which can introduce a systematic upwards of ±50% for very soft spectra. For comparison, the effect of a 10% uncertainty in the width of the PSF model is on the order of a few percent. The scale energy is determined by

the understanding of how air-showers develop and the degree to which the efficiency of various detector components is known. As such, this uncertainty is present in any analysis of VERITAS data and not strictly the 3D MLM.

On the other hand, the modeling of the background component appears to have a dramatic effect on the uncertainty of highly extended sources ($\gtrsim 0.5^\circ$) at the current time. This is primarily due to the uncertainties in the modeling of the background MSW distribution as mentioned in the previous section. Currently, the technique appears to behave acceptably for moderately extended sources ($\lesssim 0.5^\circ$), however the studies of blank field data presented in §6.5.2 suggest limits on the detectable flux level above this extension. As such, the conclusion was reached that any source with radius $\gtrsim 1^\circ$ and flux less than 10% of the Crab nebula is beyond the capabilities of the 3D MLM in its current state. This limitation is not the result of an inability of the 3D MLM to detect such a source, but rather an inability to discern whether the observed source is the result of an actual detection, or a discrepancy in the modeling of the background.

8.3 Proposed Analysis Guidelines

This section outlines a proposed set of guidelines to be used when using the 3D MLM to analyze data. It is not suggested that these guidelines are mandatory or that they are all encompassing. However, they should serve as a starting point for continued discussions on the appropriate way to approach an analysis with this technique.

There are potentially an infinite number of different models that could be fit to the emission in any given sample of data. Because the significance of a given detection decreases as the number of model fits attempted increases, it is important to define exactly what models will be tried before the analysis is conducted. Most likely any analysis of highly extended sources will be restricted to using some predefined source template, such as a disk or Gaussian. An estimate of the disk or Gaussian model width can be derived from data taken with other instruments, such as *Fermi*-LAT or HAWC. The models derived from the emission in these instruments should not be the only ones considered, however, as the morphology of the source may be energy dependent and thus be somewhat different in the VERITAS data.

After fitting a given model to the data, it is crucial to evaluate the residual plots in the analysis. These plots allow determining whether any discrepancy between the data and the models exists. The studies of blank fields presented in the previous chapter are evidence of how important these residual plots are. If such a large discrepancy as seen in the background MSW distribution for Segue 1 and Ursa Minor is present, this must be resolved before assessing the resulting TS value or the fits of the spectral function parameters.

Once an analysis is carried out, a detailed study of the relationship between the obtained TS value and the significance of the detection should be done. This involves generating many Monte Carlo simulations derived from the null model fit and fitting these generated samples with the test and null models. The resulting distribution of TS values can be used to assess the relation between a given TS value and how likely it is that the test model fit is preferred over the null model fit.

8.4 Conclusion

A new technique has been presented for studying highly extended sources in data taken by the VERITAS observatory. The technique employs a three dimensional maximum likelihood method making use of both the spatial distribution of the events on the sky and the distribution of the events in the primary gamma/hadron separation parameter of mean scaled width. Up to now this third dimension has only be used to reduce the number of background cosmic-ray events, however in the 3D MLM it is the crucial component allowing detection of these highly extended sources. The preliminary results obtained on data from two bright sources, the Crab nebula and Mrk 501, as well as a moderately extended source, IC443, show good agreement between the 3D MLM and the standard reflected region model in terms of fitted spectral parameters. The study of 1ES 1218+304 shows a slight deviation from the reflected region analysis, although the results seem to agree within the quoted errors. Studies of the moderately extended source IC443 and blank field data appear to agree well between the two techniques up to extensions of $\sim 0.5^\circ$ in radius. Several proposed improvements have been described which should enable the technique to reach its full potential for sources beyond this extension. Additionally, a proposal for best practices in using the 3D MLM analysis has been

provided. It is the hope of the author that this document will serve as a starting point for the adoption of this technique by the VERITAS collaboration.

BIBLIOGRAPHY

Abdalla, H., Abramowski, A., Aharonian, F., et al. (2016). H.E.S.S. observations of RX J1713.7-3946 with improved angular and spectral resolution; evidence for gamma-ray emission extending beyond the X-ray emitting shell. *ArXiv e-prints*.

Abdo, A. A. et al. (2009a). Fermi/Large Area Telescope Bright Gamma-Ray Source List. *ApJS*, 183:46–66.

Abdo, A. A. et al. (2009b). Milagro Observations of Multi-TeV Emission from Galactic Sources in the Fermi Bright Source List. *The Astrophysical Journal Letters*, 700:L127–L131.

Abdo, A. A. et al. (2010). Fermi-LAT Observations of the Geminga Pulsar. *The Astrophysical Journal*, 720:272–283.

Abeysekara, A. U. et al. (2013). Sensitivity of the high altitude water Cherenkov detector to sources of multi-TeV gamma rays. *Astroparticle Physics*, 50:26–32.

Abramowski, A. et al. (2011). A new snr with tev shell-type morphology: Hess j1731-347. *Astronomy & Astrophysics*, 531:A81.

Acciari, V. A. et al. (2010). Veritas search for vhe gamma-ray emission from dwarf spheroidal galaxies. *The Astrophysical Journal*, 720(2):1174.

Acciari, V. A. et al. (2011). Discovery of TeV Gamma-ray Emission from Tycho's Supernova Remnant. *Astrophysical Journal Letters*, 730:L20.

Acero, F. et al. (2010). First detection of VHE γ-rays from SN 1006 by HESS. *Astronomy & Astrophysics*, 516:A62.

Acero, F. et al. (2015). Fermi Large Area Telescope Third Source Catalog. *ApJS*, 218:23.

Ackermann, M. et al. (2012). Measurement of Separate Cosmic-Ray Electron and Positron Spectra with the Fermi Large Area Telescope. *Physical Review Letters*, 108(1):011103.

Ackermann, M. et al. (2013). Detection of the Characteristic Pion-Decay Signature in Supernova Remnants. *Science*, 339:807–811.

Ackermann, M. et al. (2016). 2FHL: The Second Catalog of Hard Fermi-LAT Sources. *ApJS*, 222:5.

Adriani, O. et al. (2009). An anomalous positron abundance in cosmic rays with energies 1.5-100GeV. *Nature*, 458:607–609.

Aguilar, M. et al. (2013). First result from the alpha magnetic spectrometer on the international space station: Precision measurement of the positron fraction in primary cosmic rays of 0.5˘350 gev. *Phys. Rev. Lett.*, 110:141102.

Aharonian, F., Akhperjanian, A. G., Bazer-Bachi, A. R., and othrrs (2006). A detailed spectral and morphological study of the gamma-ray supernova remnant RX J1713.7-3946 with HESS. *Astronomy & Astrophysics*, 449:223–242.

Aharonian, F. et al. (2007). H.E.S.S. Observations of the Supernova Remnant RX J0852.0-4622: Shell-Type Morphology and Spectrum of a Widely Extended Very High Energy Gamma-Ray Source. *Astrophysical Journal*, 661:236–249.

Aharonian, F. et al. (2009). Discovery of Gamma-Ray Emission From the Shell-Type Supernova Remnant RCW 86 With Hess. *Astrophysical Journal*, 692:1500–1505.

Aharonian, F. A. et al. (2004). High-energy particle acceleration in the shell of a supernova remnant. *Nature*, 432:75–77.

Ahnen, M. L. et al. (2016). Search for VHE gamma-ray emission from Geminga pulsar and nebula with the MAGIC telescopes. *Astronomy & Astrophysics*, 591:A138.

Aliu, E. et al. (2011). Detection of pulsed gamma rays above 100 gev from the crab pulsar. *Science*, 334(6052):69–72.

Aliu, E. et al. (2012). VERITAS deep observations of the dwarf spheroidal galaxy Segue 1. *Physical Review D*, 85(6):062001.

Aliu, E. et al. (2015). A Search for Pulsations from Geminga above 100 GeV with VERITAS. *The Astrophysical Journal*, 800:61.

Amenomori, M. et al. (2010). Observation of tev gamma rays from the fermi bright galactic sources with the tibet air shower array. *The Astrophysical Journal Letters*, 709(1):L6.

Ansoldi, S. et al. (2016). Teraelectronvolt pulsed emission from the Crab Pulsar detected by MAGIC. *Astronomy & Astrophysics*, 585:A133.

Archer, A. et al. (2014). Very-high Energy Observations of the Galactic Center Region by VERITAS in 2010-2012. *Astrophysical Journal*, 790:149.

Barlow, R. and Beeston, C. (1993). Fitting using finite monte carlo samples. *Computer Physics Communications*, 77(2):219 – 228.

Baughman, B. M., Wood, J., and for the HAWC Collaboration (2015). TeV Gamma-Ray Emission Observed from Geminga with HAWC. *Proceedings of the 34th International Cosmic Ray Conference*.

Becherini, Y., Punch, M., and Collaboration, H. (2012). Performance of HESS-II in multi-telescope mode with a multi-variate analysis. *AIP Conference Proceedings*, 1505(1):741–744.

Berge, D., Funk, S., and Hinton, J. (2007). Background modelling in very-high-energy γ-ray astronomy. *Astronomy and Astrophysics*, 466:1219–1229.

Bignami, G. F., Caraveo, P. A., and Lamb, R. C. (1983). An identification for 'Geminga' (2CG 195+04) 1E 0630+178 - A unique object in the error box of the high-energy gamma-ray source. *Astrophysical Journal Letters*, 272:L9–L13.

Blackett, P. (1949). . *Phys. Abst.*, 52:4347.

Cholis, I., Finkbeiner, D. P., Goodenough, L., and Weiner, N. (2009). The PAMELA positron excess from annihilations into a light boson. *Journal of Cosmology and Astroparticle Physics*, 12:007.

Cogan, P. (2008). VEGAS, the VERITAS Gamma-ray Analysis Suite. *Proceedings of the 30th International Cosmic Ray Conference*, 3:1385–1388.

Connaughton, V. et al. (2015). Localization of gamma-ray bursts using the fermi gamma-ray burst monitor. *The Astrophysical Journal Supplement Series*, 216(2):32.

Daniel, M. K. (2008). The VERITAS standard data analysis. *Proceedings of the 30th International Cosmic Ray Conference*, 3:1325–1328.

Daugherty, J. K. and Harding, A. K. (1982). Electromagnetic cascades in pulsars. *The Astrophysical Journal*, 252:337–347.

Drury, L., Markiewicz, W., and Völk, H. (1989). Simplified models for the evolution of supernova remnants including particle acceleration. *Astronomy and Astrophysics*, 225:179–191.

Faherty, J., Walter, F. M., and Anderson, J. (2007). The trigonometric parallax of the neutron star geminga. *Astrophysics & Space Science*, 308(1-4):225 – 230.

Feng, L., Yang, R.-Z., He, H.-N., Dong, T.-K., Fan, Y.-Z., and Chang, J. (2014). Ams-02 positron excess: New bounds on dark matter models and hint for primary electron spectrum hardening. *Physics Letters B*, 728:250 – 255.

Fermi, E. (1949). On the origin of the cosmic radiation. *Phys. Rev.*, 75:1169–1174.

Flinders, A. and for the VERITAS collaboration (2015). VERITAS Observations of the Geminga Supernova Remnant. *ArXiv e-prints*.

Gaensler, B. M. and Slane, P. O. (2006). The Evolution and Structure of Pulsar Wind Nebulae. *Annu. Rev. Astron. Astrophys*, 44:17–47.

Galbraith, W. and Jelley, J. V. (1953). Light Pulses from the Night Sky associated with Cosmic Rays (article). *Nature*, 171(4347):349–350.

Gao, X. Y. and Han, J. L. (2014). Discovery of a new supernova remnant G150.3+4.5. *Astronomy & Astrophysics*, 567:A59.

Ghisellini, G., Celotti, A., Fossati, G., Maraschi, L., and Comastri, A. (1998). A theoretical unifying scheme for gamma-ray bright blazars. *Monthly Notices of the Royal Astronomical Society*, 301:451–468.

Ginzburg, V. L. and Syrovatskii, S. I. (1965). Cosmic Magnetobremsstrahlung (synchrotron Radiation). *Annual Review of Astronomy & Astrophysics*, 3:297.

Giordano, F., Naumann-Godo, M., Ballet, J., Bechtol, K., Funk, S., Lande, J., Mazziotta, M. N., Rainò, S., Tanaka, T., Tibolla, O., and Uchiyama, Y. (2012). Fermi Large Area Telescope Detection of the Young Supernova Remnant Tycho. *Astrophysical Journal Letters*, 744:L2.

Grieder, P. (2010a). *Extensive Air Showers*, volume 1. Springer.

Grieder, P. (2010b). *Extensive Air Showers*, volume 2. Springer.

Hall, J., Vassiliev, V. V., Kieda, D. B., Moses, J., Nagai, T., and Smith, J. (2003). Veritas CFDs. *Proceedings of the 28th International Cosmic Ray Conference*, 5:2851.

Halpern, J. P. and Holt, S. S. (1992). Discovery of soft x-ray pulsations from the γ-ray source geminga. *Nature*, 357(6375):222–224.

Hanna, D., McCann, A., McCutcheon, M., and Nikkinen, L. (2010). An LED-based flasher system for VERITAS. *Nuclear Instruments and Methods in Physics Research A*, 612:278–287.

Harding, A. K., Tademaru, E., and Esposito, L. W. (1978). A curvature-radiation-pair-production model for gamma-ray pulsars. *The Astrophysical Journal*, 225:226–236.

Heck, D., Knapp, J., Capdevielle, J. N., Schatz, G., and Thouw, T. (1998). *CORSIKA: a Monte Carlo code to simulate extensive air showers.* Thouw, T.. Forschungszentrum Karlsruhe GmbH, Karlsruhe (Germany)., Feb 1998, V + 90 p., TIB Hannover, D-30167 Hannover (Germany).

Hewish, A., Bell, S. J., Pilkington, J. D. H., Scott, P. F., and Collins, R. A. (1968). Observation of a rapidly pulsating radio source. *Nature*, 217(5130):709–713.

Hillas, A. M. (1982). The sensitivity of cerenkov radiation pulses to the longitudinal development of cosmic-ray showers. *Journal of Physics G: Nuclear Physics*, 8(10):1475.

Hillas, A. M. (1985). Cerenkov light images of EAS produced by primary gamma. *International Cosmic Ray Conference*, 3.

Hooper, D., Blasi, P., and Serpico, P. D. (2009). Pulsars as the sources of high energy cosmic ray positrons. *Journal of Cosmology and Astroparticle Physics*, 2009(01):025.

Kieda, D. B. f. t. V. C. (2013). The Gamma Ray Detection sensitivity of the upgraded VERITAS Observatory. *Proceedings of the 33rd International Cosmic Ray Conference*.

Knödlseder, J. et al. (2016). GammaLib and ctools: A software framework for the analysis of astronomical gamma-ray data. *ArXiv e-prints*.

Kohnle, A. et al. (1996). Stereoscopic imaging of air showers with the first two HEGRA Cherenkov telescopes. *Astroparticle Physics*, 5:119–131.

Li, T.-P. and Ma, Y.-Q. (1983). Analysis methods for results in gamma-ray astronomy. *ApJ*, 272:317–324.

Linden, T. and Profumo, S. (2013). Probing the pulsar origin of the anomalous positron fraction with ams-02 and atmospheric cherenkov telescopes. *The Astrophysical Journal*, 772(1):18.

Longair, M. (1992). *High Energy Astrophysics*. Cambridge University Press, 2 edition.

Lotto, B. D. and the Magic Collaboration (2012). The magic telescopes: performance, results and future perspectives. *Journal of Physics: Conference Series*, 375(5):052021.

Malkov, M. A. and Drury, L. O. (2001). Nonlinear theory of diffusive acceleration of particles by shock waves. *Reports on Progress in Physics*, 64(4):429.

Manchester, R. N., Hobbs, G. B., Teoh, A., and Hobbs, M. (2005). The australia telescope national facility pulsar catalogue. *The Astronomical Journal*, 129(4):1993.

Mattox, J. R. et al. (1996). The Likelihood Analysis of EGRET Data. *ApJ*, 461:396.

McCann, A., Hanna, D., Kildea, J., and McCutcheon, M. (2010). A new mirror alignment system for the {VERITAS} telescopes. *Astroparticle Physics*, 32(6):325 – 329.

Meyer, M., Horns, D., and Zechlin, H.-S. (2010). The Crab Nebula as a standard candle in very high-energy astrophysics. *Astronomy & Astrophysics*, 523:A2.

Muslimov, A. G. and Harding, A. K. (2004). High-altitude particle acceleration and radiation in pulsar slot gaps. *The Astrophysical Journal*, 606(2):1143.

Olive, K. A. et al. (2014). Review of particle physics. *Chinese Physics C*, 38(9):090001.

Park, N. and VERITAS Collaboration (2015). Performance of the VERITAS experiment. *Proceedings of the 34th International Cosmic Ray Conference*.

Perkins, J. S., Maier, G., and The VERITAS Collaboration (2009). VERITAS Telescope 1 Relocation: Details and Improvements. *2009 Fermi Symposium, eConf Proceedings C091122*.

Rebillot, P. F., Buckley, J. H., Dowkontt, P., and Kosack, K. (2003). The VERITAS Flash ADC Electronics System. *Proceedings of the 28th International Cosmic Ray Conference*, 5:2827.

Roache, E., Irvin, R., Perkins, J. S., Harris, K., Falcone, A., Finley, J., and Weeks, T. (2008). Mirror Facets for the VERITAS Telescopes. *Proceedings of the 30th International Cosmic Ray Conference*, 3:1397–1400.

Romani, R. W. and Yadigaroglu, I.-A. (1995). Gamma-ray pulsars: Emission zones and viewing geometries. *The Astrophysical Journal*, 438:314–321.

Rosswog, S. and Brüggen, M. (2007). *Introduction to High-Energy Astrophysics*. Cambridge University Press, New York, 1 edition.

Smith, A. J. f. (2015). HAWC: Design, Operation, Reconstruction and Analysis. *ArXiv e-prints*.

The *Fermi*-LAT Collaboration (2017). 3FHL: The Third Catalog of Hard *Fermi*-LAT Sources. *ArXiv e-prints*.

Thompson, D. J., Fichtel, C. E., Hartman, R. C., Kniffen, D. A., and Lamb, R. C. (1977). Final SAS-2 gamma-ray results on sources in the galactic anticenter region. *ApJ*, 213:252–262.

Urry, C. M. and Padovani, P. (1995). Unified Schemes for Radio-Loud Active Galactic Nuclei. *Publications of the Astronomical Society of the Pacific*, 107:803.

Weekes, T. C. (2005). The Atmospheric Cherenkov Imaging Technique for Very High Energy Gamma-ray Astronomy. *ArXiv Astrophysics e-prints*.

Weekes, T. C., Cawley, M. F., Fegan, D. J., Gibbs, K. G., Hillas, A. M., Kowk, P. W., Lamb, R. C., Lewis, D. A., Macomb, D., Porter, N. A., Reynolds, P. T., and Vacanti, G. (1989). Observation of TeV gamma rays from the Crab nebula using the atmospheric Cerenkov imaging technique. *ApJ*, 342:379–395.

Weinstein, A. (2008). The VERITAS Trigger System. *Proceedings of the 30th International Cosmic Ray Conference*, 3:1539–1542.

Wilks, S. S. (1938). The Large-Sample Distribution of the Likelihood Ratio for Testing Composite Hypotheses. *The Annals of Mathematical Statistics*, 9:60–62.

Younk, P. W., Lauer, R. J., Vianello, G., Harding, J. P., Ayala Solares, H. A., Zhou, H., and Michelle Hui for the HAWC Collaboration (2015). A high-level analysis framework for HAWC. *ArXiv e-prints*.

Yüksel, H., Kistler, M. D., and Stanev, T. (2009). Tev gamma rays from geminga and the origin of the gev positron excess. *Phys. Rev. Lett.*, 103:051101.

Zirnstein, E. J., Heerikhuisen, J., Funsten, H. O., Livadiotis, G., McComas, D. J., and Pogorelov, N. V. (2016). Local interstellar magnetic field determined from the interstellar boundary explorer ribbon. *The Astrophysical Journal Letters*, 818(1):L18.

APPENDIX A. FIRST ORDER FERMI ACCELERATION

This derivation of first order Fermi (Fermi-I) acceleration will follow Fermi (1949). The following notation will be observed

- Unprimed values are computed in the reference frame of the unshocked material.
- A *prime* will denote values computed in the reference frame of the shocked material.
- A *0* subscript denotes values prior to the scattering event.
- A *1* subscript denotes values after the scattering event.

A.1 Energy Gain

Consider the following setup. A shock moves through a stationary medium with speed U. Inside the stationary medium, a relativistic particle with speed v_0 is incident on the shock front with some inclination angle θ. This particle collides with magnetic fields co-moving with the shocked material and is reflected back across the shock front. A depiction of the scenario in question is provided in Fig A.1

To predict the change in energy it is necessary to first transform into the frame of reference of the shocked material.

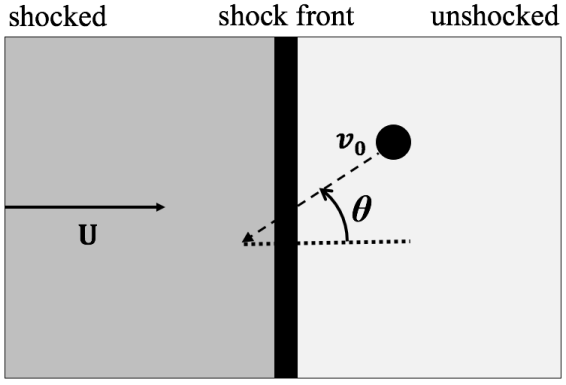

Figure A.1: Depiction of a typical scenario involving Fermi-I acceleration.

$$\begin{bmatrix} E_0'/c & p_{x,0}' & p_{y,0}' & p_{z,0}' \end{bmatrix} = \begin{bmatrix} \gamma & -\gamma\beta & 0 & 0 \\ -\gamma\beta & \gamma & 0 & 0 \\ 0 & 0 & 1 & 0 \\ 0 & 0 & 0 & 1 \end{bmatrix} \cdot \begin{bmatrix} E_0/c \\ p_0 \cdot \cos\theta \\ p_0 \cdot \sin\theta \\ 0 \end{bmatrix}$$

where

$$\begin{aligned} \gamma &= \left[1+\beta^2\right]^{-1/2} \\ \beta &= \frac{U}{c} \end{aligned} \tag{A.1}$$

Because the motion of interest is in the x direction, the other two dimensions will be ignored from here on. The above provides the following for the particle energy and momentum in the shocked frame

$$\begin{aligned} E_0' &= \gamma E_0 + \gamma c\beta p_0 \cdot cos\theta \\ p_{x,0}' &= -\gamma\beta\frac{E_0}{c} - \gamma p_0 \cdot cos\theta \end{aligned} \tag{A.2}$$

The scattering of the particle off of the magnetic field is considered to be elastic. Therefore, after the interaction the energy will be unchanged and the momentum will change sign. The energy and momentum after the scattering will then be

$$\begin{aligned} E_1' &= \gamma E_0 + \gamma c\beta p_0 \cdot cos\theta \\ p_{x,1}' &= \gamma\beta\frac{E_0}{c} + \gamma p_0 \cdot cos\theta \end{aligned} \tag{A.3}$$

Now transforming back into the frame of reference of the unshocked material gives[1]

$$\begin{bmatrix} E_1/c & p_{x,1} & p_{y,1} & p_{z,1} \end{bmatrix} = \begin{bmatrix} \gamma & \gamma\beta & 0 & 0 \\ \gamma\beta & \gamma & 0 & 0 \\ 0 & 0 & 1 & 0 \\ 0 & 0 & 0 & 1 \end{bmatrix} \cdot \begin{bmatrix} E_1'/c \\ p_{x,1}' \\ p_{y,1}' \\ 0 \end{bmatrix}$$

or

$$\begin{aligned} E_1 &= \gamma^2 E_0 + 2\gamma^2\beta c p_0 cos\theta + \gamma^2\beta^2 E_0 \\ p_{x,1} &= \gamma\beta\frac{E_0}{c} + \gamma p \cdot cos\theta \end{aligned} \tag{A.4}$$

[1]Note that here the β has flipped signs from the previous transformation matrix.

Noting the following relativity relations for momentum and energy

$$\begin{aligned} p_0 &= \Gamma m_0 v_0 \\ E_0 &= \Gamma m_0 c^2 \\ \Gamma &= \left[1 + \left(\frac{v_0}{c}\right)^2\right]^{-1/2} \end{aligned} \tag{A.5}$$

the following relation for momentum and energy can be derived.

$$\frac{p_0}{E_0} = \frac{v_0}{c^2} \tag{A.6}$$

This provides a means for relating the energy of the particle after scattering off the shocked material to the energy of the particle before scattering.

$$\begin{aligned} \frac{E_1}{E_0} &= \gamma^2 \left[1 + 2\beta c \frac{p_0}{E_0} cos\theta + \beta^2\right] \\ &= \gamma^2 \left[1 + \frac{2U v_0 cos\theta}{c^2} + \left(\frac{U}{c}\right)^2\right] \end{aligned} \tag{A.7}$$

Further, making the assumption that the shock speed is *not* relativistic (i.e. $\gamma \sim 1$) and expanding to second order in (U/c), Eq. A.7 can be rewritten as

$$\frac{E_1 - E_0}{E_0} = \frac{\Delta E}{E_0} = \frac{2U v_0 cos\theta}{c^2} + 2\left(\frac{U}{c}\right)^2 \tag{A.8}$$

To finish off this discussion, it is important to point out that the above process is unchanged when looking at a particle moving across the shock front from the shocked material to the unshocked material. In this case, the unshocked material appears to be moving with the same speed, but in the opposite direction. As a result, a scatter event in this region will result in the same increase in energy. It follows that a particle will gain energy no matter which direction it travels across the shock front. Because of this, particles at the shock front can be accelerated to very high energies.

APPENDIX B. DESCRIPTION OF OUTPUTS

This appendix outlines the various outputs of the VERITAS 3D MLM analysis.

B.1 Numbers

In addition to storing the obvious parameters (those that parameterize the source spectral function), the resulting negative log-likelihood (NLL) for the test and null models are also stored. These serve as a cross check when attempting to assess the true significance of a given test statistic value, as it is expected the associated NLL for the test and null models in those should have similar values[1].

B.2 Spectral Energy Distribution

The spectral energy distribution represents the best fit values of the parameters for a given spectrum. Once the best fit values of these parameters are stored, a plot is generated which represents this distribution. Included in this plot is also a one sigma confidence band (often referred to as a 'butterfly' plot) representing the error on the fit. The butterfly plot incorporates the errors on each of the spectral parameters as well as the correlations between them in the fit (see Appendix D for more details on how the butterfly plot is generated).

Once the overall fit is finished, secondary fits are conducted in each of the energy bins used in the analysis. First, every parameter in the spectral function is fixed with exception to the normalization parameter f_0. The normalization term is then refit in each bin allowing for a set of spectral points to be generated for each source. The test statistic for each bin is also stored

[1]Since the Monte Carlo generated simulations represent perfect background models, it is useful to note that the fits will be even better giving a slightly lower negative NLL value on average. However, it is expected that the value derived from data will fall somewhere in the distribution of NLL values from cross checks. If this is the case, one can expect a reasonably good agreement between the models and the data.

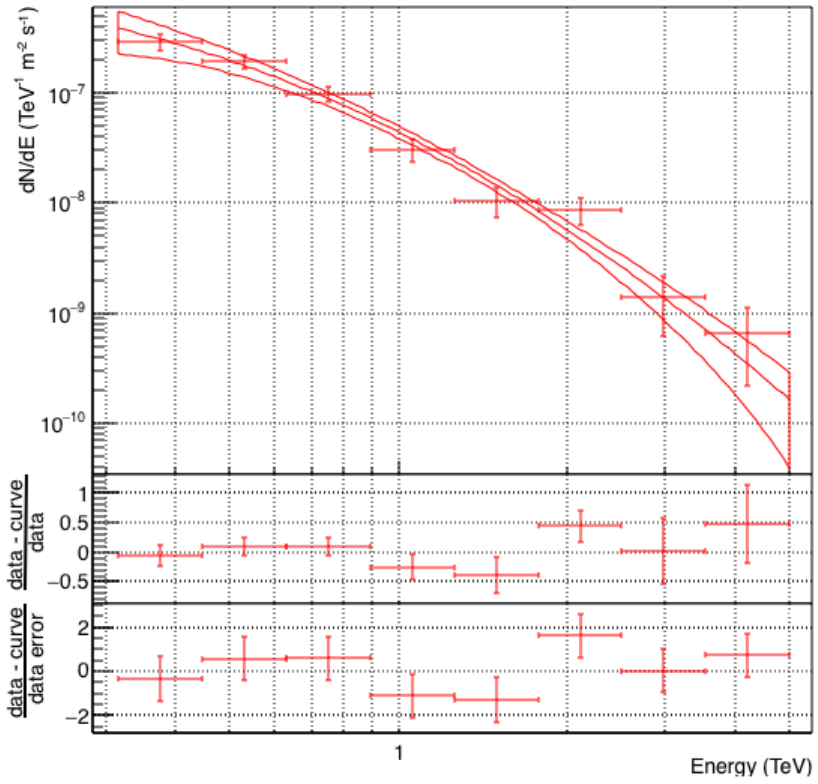

Figure B.1: Sample spectrum. (*top*) Spectral points from the generated Monte Carlo sample (red points) and butterfly plot showing the 68% confidence band on the differential energy flux. (*middle*) Percentage difference between the spectral point and the best fit model curve. (*bottom*) Number of standard deviations the data points fall away from the model.

for each source. When plotting these points, each point that results in a TS value below a given threshold is plotted as a two sigma upper limit instead of a point with one sigma error bars[2].

B.3 Spatial Residuals

In order to better compare the results of the model fit to the data, a spatial residual map can be computed either as a simple excess map or as a significance map (see Fig. B.3). The map is computed using Eq. 4.2. N_{OFF} is estimated by integrating the models within 0.1° of a given bin position, either including or excluding the source model. N_{ON} is estimated by integrating the data within the same region. The models and data are also integrated over the

[2]A threshold of TS < 4 is used to establish upper limits in this analysis.

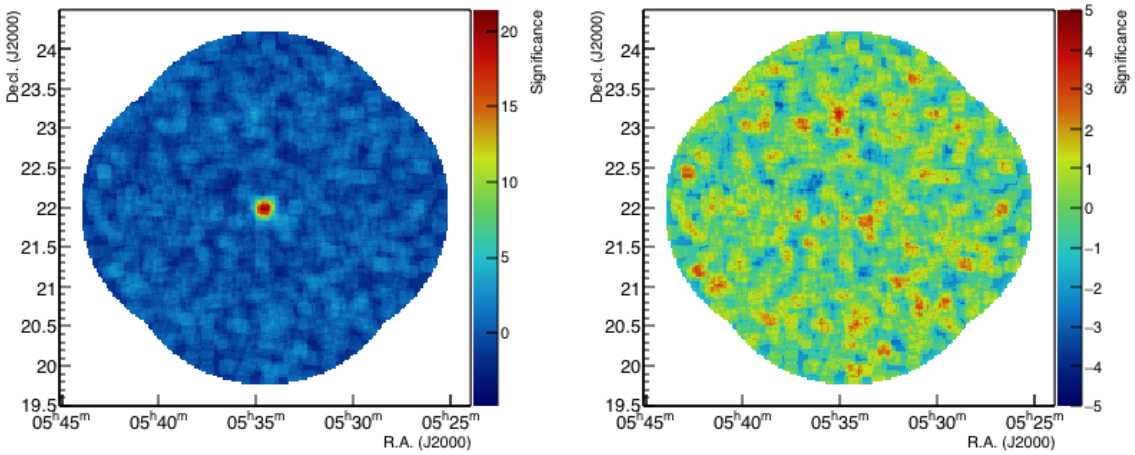

(a) Significance Map (b) Source Subtracted Significance Map

Figure B.3: Spatial significance map using a 0.1° integration radius and a MSW range of [0.7875,1.0875]. (*left*) Significance map computed using only the background component of the test model to estimate N_{OFF}. (*right*) Significance map computed using the full test model to estimate N_{OFF}.

MSW range of [0.7875,1.0875] in order to enhance the gamma-ray component.

B.4 MSW Distributions and Residuals

This plot shows the distribution of the data (black points), the background model (blue dashed curve), the individual source models (non-blue dashed curves), and the full combined model (solid violet curve). This projection of the MSW model component can be done for either the full map, or for a region within a certain distance or outside a certain distance from the source.

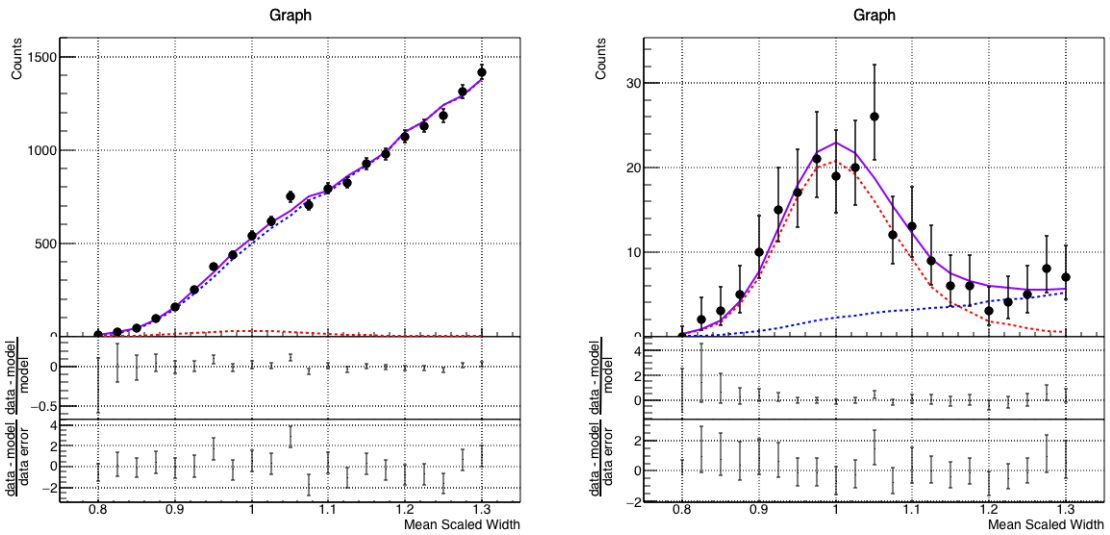

(a) Full Field MSW distribution

(b) Within 0.1° of source position

Figure B.5: (*left*) MSW projection from the full data sample. (*right*) MSW projection from the region within 0.1° of the source position.

APPENDIX C. ZENITH ANGLE CORRECTION

There is a notable change in the instruments response to air-shower events depending on the zenith angle of the observation. air-shower events coming from high zenith angles have a large air mass through which they must travel. Because the transmission of air-showers depends significantly on how much atmosphere the shower must travel through, the lower limit in energy for detection moves towards high energies at larger zenith angles. This presents an added challenge as our background model is energy dependent. Since the threshold can change significantly over a few degrees it is necessary to take this into consideration in our models. Since the air-mass is assumed to follow a cos(zenith) distribution, a linear correction in cos(zenith) is assumed. To do this the subsequent steps are followed.

When reading in the events from a data file, the projected x,y position of each event is stored in a two dimensional map of counts. This allows detailed knowledge of where the events come from in our camera. These events are stored in coarse 0.1°x0.1° spatial bins and equally spaced logarithmic bins of energy. The [zenith,azimuth] bins are chosen to be the same as detailed for other components of the models. In order to properly assign the gradient accross the camera in cos(zenith), the livetime weighted average is computed for all runs which contribute to a give [zenith,azimuth] bin. Each of these distributions is computed at the time the models are derived and stored in the output files.

When deriving the correction function, the above stored two dimensional projection of events is integrated over the energy range of the reconstructed energy bin which is being modeled. This allows the correct acceptance to be derived on the fly without the need to regenerate the stored event counts whenever the energy binning is changed. Next the uncorrected acceptance (i.e. the acceptance assuming azimuthal symmetry) is used to normalize each bin of the projected map. A cos(zenith) gradient map is also produced at this time for comparison to the

counts map. This cos(zenith) map is necessary since the counts map is produced in projected coordinates assuming the x and y-axes are analogous with right ascension and declination, respectively.

C.1 Computing the Cos(zenith) Gradient Map

As mentioned above, the background acceptance models are stored as projected coordinates where [x,y] are analogous to the gnomonic projection of [right ascension, declination]. Because of this, the models are rotated in [azimuth, zenith]. In order to compute the cos(zenith) gradient across these model maps, the following steps are followed.

When computing the gradient maps, the following information is initially available and will be used:

- Azimuth (A) and zenith (z) of the map center
- Observatory latitude (ϕ)[1]

This information is first used to compute the declination (δ) and hour angle (H) of the map center via Eq. C.1 and Eq. C.2, respectively).

$$\delta = cos^{-1}\left[cos(z)sin(\phi) + sin(z)cos(\phi)cos(A)\right] \tag{C.1}$$

$$H = cos^{-1}\left[\frac{cos(z) - sin(\delta)sin(\phi)}{cos(\delta)cos(\phi)}\right] \tag{C.2}$$

It is important to note that the above equations are derived such that azimuth is zero due North and increases along the horizon towards the West. However, the azimuth values used in the MLM code described above use a different definition where azimuth increases towards the East. Since the only use of the azimuth involves cos(azimuth), the results will be identical for the two definitions. The only difference is how the hour angle is defined. For the MLM code, the following definition for hour angle is used:

$$H = \begin{cases} -H, & 0^\circ \leq A < 180^\circ \\ H, & 180^\circ \leq A < 360^\circ \end{cases}$$

[1]The latitude of the VERITAS array is taken to be +31.675°.

Using the hour angle, the right ascension (α) of the map center can be computed knowing the local siderial time (t) from Eq. C.3.

$$t = H + \alpha \tag{C.3}$$

However, since the cos(zenith) gradient map will be unchanged regardless of the local sidereal time or the right ascension of the map center, the assumption of $\alpha_{center} = 0$ can be employed. Now using this value for α a *seudo* local sidereal time (t') can be computed. Note that t' will be equivalent to H_{center}.

At this point, a loop over every bin in the spatial model is done. At each bin, [α_{bin},δ_{bin}] is computed. From α_{bin} the hour angle (H_{bin}) is computed using Eq. C.3 where t' and α_{bin} are used in place of t and α. H_{bin} and δ_{bin} are then plugged into Eq. C.4 to compute the cos(zenith) of the center of the given spatial map bin.

$$cos(z_{bin}) = sin(\delta_{bin})sin(\phi) + cos(\delta_{bin})cos(\phi)cos(H_{bin}) \tag{C.4}$$

Thus a map representing $cos(z_{bin})$-$cos(z_{center})$ can be constructed representing the cos(zenith) gradient across the map at a given observing position in azimuth and zenith.

C.2 Computing the Acceptance Correction

As mentioned above, when generating the radial acceptance curves two additional maps are also computed:

- *Raw counts map* - Map of the total number of events falling into a given bin of the sky
- *Livetime map* - Stores the total livetime contributing to a bin in the Raw counts map

The 'livetime' map is filled for all bins of the map which are not excluded by nearby sources or bright stars[2]. The 'raw counts' map is only filled when a given event passes the requested cuts. These maps, along with the radial acceptance curves, are generated for each bin of zenith, azimuth[3], and energy.

When generating the correction, all 'raw counts' maps which contribute to a given energy range are combined, normalizing each bin by the total livetime of all the data runs which

[2] "Bright stars" include stars with B-magnitude of 6 or less.

[3] Due to the small angular area and limited statistics near zenith, all bins of azimuth in the smallest zenith angle bin are combined into a single bin.

contributed to that bin. Any bin which has a zero livetime is removed. An uncorrected acceptance map is then generated from the stored acceptance curves. Each bin in the livetime-corrected map is then normalized by the uncorrected acceptance at the position of that bin. From here a plot is made of 'counts/(livetime*acceptance)' as a function of Δ cos(zenith). A linear fit is made, and this fit function becomes the correction that is applied.

APPENDIX D. BUTTERFLY PLOTS

A spectral butterfly plot is a way of showing the error on the differential flux at a given energy. It is computed by taking the errors on the various spectral parameters and propogating those errors through the spectral formula. Care is taken to also consider the correlation between various terms.

The following sections outline this procedure for the power-law and log-parabola spectral functions. Use will be made of the propogation formula's presented in Table D.1.

D.1 Spectral Function Error

D.1.1 Power Law

The power law spectral function takes the form of Eq. D.1.

$$\frac{dN}{dE} = f_0 \left(\frac{E}{E_0} \right)^{\Gamma} \tag{D.1}$$

Table D.1: Various error propogation formulae. Lowercase letters denote values not dependent on fit parameters while uppercase letters denote fitted parameters that have a measured error. *cov(A,B)* denotes the covariance between parameters A and B and is equivalent to $cor(A,B)\sigma_A\sigma_B$ where $cor(A,B)$ is the correlation between A and B.

Function	Error
$F = AB$	$\sigma_F^2 = \left(\frac{\sigma_A}{A}\right)^2 + \left(\frac{\sigma_B}{B}\right)^2 + 2\frac{cov(A,B)}{AB}$
$F = a^A$	$\sigma_F^2 = F^2 \left(\ln(a)\sigma_A\right)^2$
$F = aA + bB$	$\sigma_F^2 = a^2\sigma_A^2 + b^2\sigma_B^2 + 2abcov(A,B)$

Rewriting this as

$$\begin{aligned} \frac{dN}{dE} &= F = AB \\ A &= f_0 \\ B &= \left(\frac{E}{E_0}\right)^{\Gamma} \end{aligned} \tag{D.2}$$

the errors on the two parts A and B can be determined independently.

$$\begin{aligned} \sigma_A^2 &= \sigma_{f_0}^2 \\ \sigma_B^2 &= \left[\left(\frac{E}{E_0}\right)^{\Gamma} \sigma_\Gamma \ln\left(\frac{E}{E_0}\right)\right]^2 \end{aligned} \tag{D.3}$$

and when combined this gives the error on F as

$$\begin{aligned} \frac{\sigma_F^2}{F^2} &= \left(\frac{\sigma_A}{A}\right)^2 + \left(\frac{\sigma_B}{B}\right)^2 + 2\frac{cov(A,B)}{AB} \\ &= \left(\frac{\sigma_{f_0}}{f_0}\right)^2 + \left(\ln\left(\frac{E}{E_0}\right)\sigma_\Gamma\right)^2 + 2\frac{cov(f_0,\Gamma)}{f_0}\left|\ln\left(\frac{E}{E_0}\right)\right| \\ &= \left(\frac{\sigma_{f_0}}{f_0}\right)^2 + \left(\ln\left(\frac{E}{E_0}\right)\sigma_\Gamma\right)^2 + 2\frac{cor(f_0,\Gamma)\sigma_{f_0}\sigma_\Gamma}{f_0}\left|\ln\left(\frac{E}{E_0}\right)\right| \end{aligned} \tag{D.4}$$

The substition of *covariance* for *correlation* has been made in the lower version of the formula as the *correlation* is readily available in RooFit. The butterfly plot at any given point is thus plotted as $F \pm \sigma_F$. The formula has been presented as the ratio between σ_F^2 and F^2 for reasons that will become clear when computing the decorrelation energy.

D.1.2 Log-parabola

The log-parabola spectral function takes the form of Eq. D.5.

$$\frac{dN}{dE} = f_0\left(\frac{E}{E_0}\right)^{\alpha+\beta\ln(E/E_0)} = F_{lp} \tag{D.5}$$

The derivation of the error on the differential energy flux for this method is a bit more cumbersome, so instead a short cut can be used. Again, rewritting the formula as

$$\begin{aligned} \frac{dN}{dE} &= F_{lp} = AB \\ A &= f_0 \\ B &= \left(\frac{E}{E_0}\right)^{\Gamma} \\ \Gamma &= \alpha + \beta\ln(E/E_0) \end{aligned} \tag{D.6}$$

the following errors on each of A, B, and Γ can be computed.

$$\begin{aligned}\sigma_A^2 &= \sigma_{f_0}^2 \\ \sigma_B^2 &= \left(B\sigma_\Gamma \ln\left(\frac{E}{E_0}\right)\right)^2 \\ \sigma_\Gamma^2 &= \sigma_\alpha^2 + \left(\sigma_\beta \ln\left(\frac{E}{E_0}\right)\right)^2 + 2cov(\alpha,\beta)\ln\left(\frac{E}{E_0}\right)\end{aligned} \tag{D.7}$$

Now, starting from the equation for the power law spectrum, specifically the middle form in Eq. D.4, subsitute for Γ and σ_Γ.

$$\begin{aligned}\frac{\sigma_{F_{lp}}^2}{F_{lp}^2} = \left(\frac{\sigma_{f_0}}{f_0}\right)^2 + \left(\ln\left(\frac{E}{E_0}\right)\right)^2 \left[\sigma_\alpha^2 + \left(\sigma_\beta \ln\left(\frac{E}{E_0}\right)\right)^2 + 2cov(\alpha,\beta)\ln\left(\frac{E}{E_0}\right)\right] \\ + 2\frac{cov(f_0, \alpha+\beta\ln(E/E_0))}{f_0}\left|\ln\left(\frac{E}{E_0}\right)\right|\end{aligned} \tag{D.8}$$

and finally substituting for the covariance formula the final form used in the analysis is found

$$\begin{aligned}\frac{\sigma_{F_{lp}}^2}{F_{lp}^2} = \left(\frac{\sigma_{f_0}}{f_0}\right)^2 + \left(\ln\left(\frac{E}{E_0}\right)\right)^2 \left[\sigma_\alpha^2 + \left(\sigma_\beta \ln\left(\frac{E}{E_0}\right)\right)^2 + 2cor(\alpha,\beta)\sigma_\alpha\sigma_\beta\ln\left(\frac{E}{E_0}\right)\right] \\ + 2\frac{cor(f_0,\alpha)\sigma_{f_0}\sigma_\alpha + cor(f_0,\beta)\sigma_{f_0}\sigma_\beta \ln\left(\frac{E}{E_0}\right)}{f_0}\left|\ln\left(\frac{E}{E_0}\right)\right|\end{aligned} \tag{D.9}$$

where σ_F is the error on the differential energy flux F_{lp} given in Eq. D.5.

D.2 Decorrelation Energy

The decorrelation energy is the energy where the *relative* error on the differential flux is a minimum. In other words, it is the energy E_{dec} that satisfies the relation

$$\frac{\partial}{\partial E}\left(\frac{\sigma_F^2}{F^2}\right)\Bigg|_{E=E_{dec}} = 0 \tag{D.10}$$

This formula is simple to solve for the power law function. The derivative is given by

$$\frac{\partial}{\partial E}\left(\frac{\sigma_F^2}{F^2}\right)\Bigg|_{E=E_{dec}} = 0 = 2\ln\left(\frac{E_{dec}}{E_0}\right)\frac{\sigma_\Gamma^2}{E_{dec}} + 2\frac{cor(f_0,\Gamma)\sigma_{f_0}\sigma_\Gamma}{f_0 E_{dec}} \tag{D.11}$$

and solving for E_{dec} gives

$$E_{dec} = E_0 exp\left[-\frac{cor(f_0,\Gamma)\sigma_{f_0}}{f_0\sigma_\Gamma}\right] \tag{D.12}$$

Solving this equation for the log-parabola function is non-trivial however. Rather, a numerical approach is used in order to find the approximate minimum of the function.

D.3 Generic Approach

It is worth noting that while the above formulation results in a simple, clean description of the butterfly plot taking into consideration the errors and correlations between the parameters, it also relies on the ability to actually solve the complex error propagation formula for a given spectral function. Solving this formula becomes extremely complicated and tedious as the number of free parameters in the spectral function increases. Instead, there is an alternative method in which the minimum and maximum of the function are found at a given energy within the bounds of the associated error ellipse[1] of the function. This method for computing the butterfly plot is much more generic and can be applied to any given spectral function, at the cost of an increase in computation time. This is the method used by the *ctools* software for computing the butterfly plot from a power law fit (Knödlseder et al., 2016).

The process for doing this is rather straight forward. First, the error ellipse representing the requested confidence interval is computed from the covariance matrix resulting from a given spectral fit. Then, the spectral function is minimized and maximized within the bounds of that error ellipse at evenly spaced points along the energy range of the fit.

Due to time constraints, this method of computing the butterfly plot has not been implemented in the VERITAS MLM code at the time of writing, but would be a very beneficial addition in the future.

[1] In the case of a function with 2 parameters (such as a power law) the bounding object will be an ellipse. In the case of a function with 3 free parameters (such as a log-parabola) it will be an ellipsoid.